Fuselage-wing-slat junction noise

Aeroacoustic analysis of a fuselage-wing-slat junction in approach configuration

Piera, H.I.G.

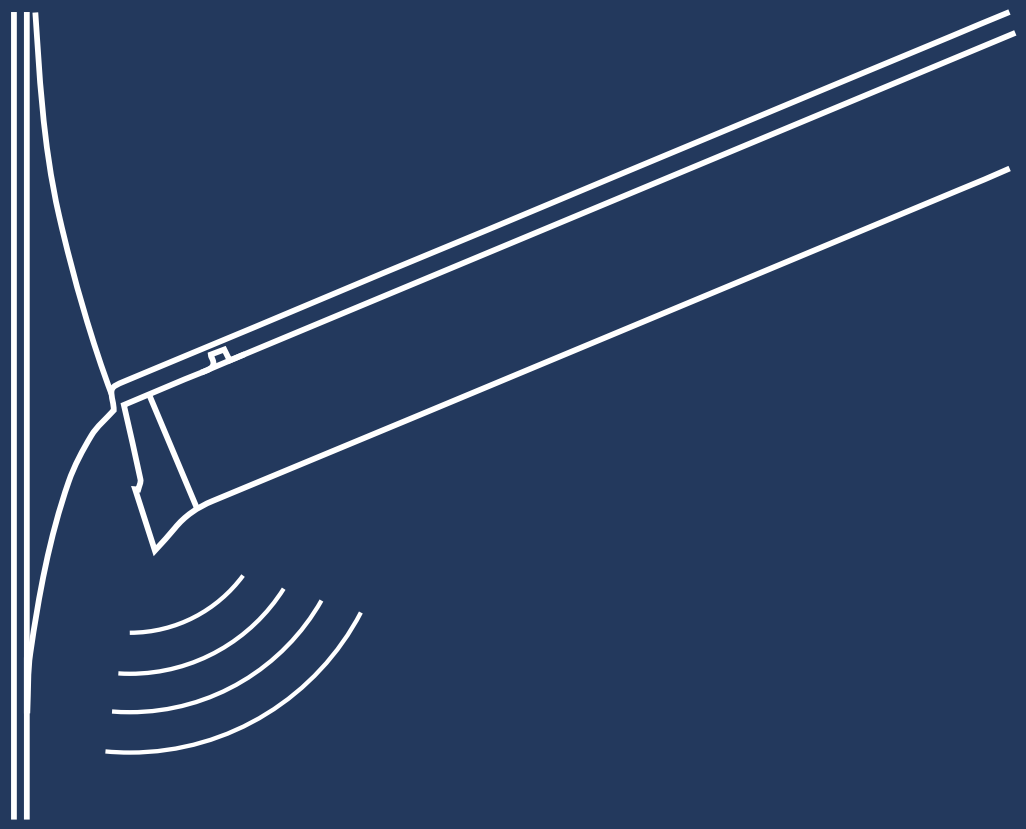

TU Delft

MUTESKIN® BY MUTECH

Fuselage-wing-slat junction noise

Aeroacoustic analysis of a fuselage-wing-slat junction in approach configuration

MSc. Thesis

by

Piera, H.I.G.

To obtain the degree of

Master of Science
in Aerospace Engineering

To be defended Wednesday June 12, 2024 at 13:00
at the Delft University of Technology

Student number:	4667158	
Thesis committee:	Dr. D. Ragni	Delft University of Technology
	Dr. R. Zamponi	Delft University of Technology & Von Karman Institute
	Dr. ir. R. Vos	Delft University of Technology
	Ir. F. Hartog	MuTech B.V.

Faculty of Aerospace Engineering · Delft University of Technology

Preface

This thesis wraps up my journey as a student at Delft University of Technology. I'm grateful for the years spent studying here. At the TU I've learned a lot about engineering, mathematics, and plenty of other academic subjects. But truth be told, I've learned the most from the people around me, the ones I already knew, and the new people I've met along the way.

I'd like to start by thanking Friso, my direct supervisor, and the rest of the team at MuTech, Bieke, Laurens, Michiel, and Olaf, for guiding me through my thesis project this last year. Friso's unwavering enthusiasm and positivity have been a much-appreciated support in the making of this thesis project. I am grateful for his guidance, feedback, and encouragement which have elevated my work to its full potential. I also want to thank the rest of the team for the great time, and truly fun and engaging discussions we've shared. Last but not least, I'd like to thank my fellow graduation students at MuTech, Marlon and Tjeu. Together, we shared seemingly hopeless moments when nothing worked, and the software tools once again decided to play games. More importantly, we had great laughs while doing so.

The TU Delft's aeroacoustics department has provided me with much of the knowledge necessary to thoroughly perform this research, both in content and academically. I would like to thank Dani and Riccardo for their supervisory work on my thesis project. I especially appreciated their direct comments on my often convoluted proposals or writing style. Their availability for questions and feedback was invaluable. Regardless of how well I thought I knew a subject, I often came to the conclusion that "... indeed, I was wrong ...". Special thanks also to Frits for his assistance with my numerical set-up, and to Tercio for the numerous discussions we've had on airfoil noise generation.

Most importantly, I would like to thank my family and friends who were always ready to help this past year. My parents continuously supported me with tasks outside my thesis work and have always offered help with my projects, no matter the technicality of the subjects. They were also there to listen to my frustrations, and, astoundingly, they always picked my side. Next, I want to thank my brothers. As the youngest, I can always rely on their support. Their confidence in my abilities, even when I once again begin a task stupidly late, has been a constant source of motivation.

My friends provide the fun and laughter in my everyday life, arguably the most important part. I would like to thank my housemates for putting up with me this last year when too much of what I talked about was my thesis project. I would like to thank all my friends for the awesome past few years — whether playing sports, rehearsing for a concert, going on numerous random activities, or simply having a drink or two together. Because regardless of how fun it sounds, there is more to life than aeroacoustics.

May 2024, Delft
- Hielke Piera

Executive Summary

A decades-long steady rise in air movements has disproportionally impacted airport-neighbouring communities. These communities bear the brunt of the aviation industry's air, and noise pollution, detrimental to their livelihood. Airports near densely populated areas face increasing societal and governmental scrutiny to reduce their noise pollution and improve the quality of life for airport-neighbouring communities. Airframe noise has become a prominent noise source during approach due to the increased usage of quieter high-bypass ratio turbofan engines. Flyover measurements suggest that the leading edge junction between the fuselage, wing, and slat is a high-intensity localised noise source. This airframe region has been sparsely researched. Therefore, this study aims to describe the relation between the aero-structural design of the fuselage-wing-slat junction and its aeroacoustic footprint for an aircraft in approach configuration.

The research set-up was designed for open-jet numerical simulations using the commercial Lattice Boltzmann Method (LBM) based CFD solver PowerFLOW, with future compatibility for experimental open-jet wind tunnel validation studies at the TU Delft's Anechoic wind tunnel. Three variations of a two-sideplate research set-up were created based on a slat-and-main-wing modified 30P30N airfoil cross-section. A 'No Gap' (NG) geometry that connects the slat to both sideplates; a 'No Horn & Step Stump' (NH) geometry that has a simplified slat side-edge and slat stump, a feature that blends the main wing with the fuselage; and a 'Horn & Smooth Stump' (H) geometry, which incorporates a slat horn on the slat side-edge and a slat stump modelled after the Airbus A320. For all three variations, the relative positions of the slat track, slat side-edge and other junction surfaces were modelled after the Airbus A320 as well. All model variants were analysed based on their far-field noise radiation and the near-field behaviour of aerodynamic turbulent structures.

The results of the simulated scaled models were compared to literature. The noise radiation of the 'H' model was scaled in power and frequency (Strouhal-based), and compared to beamforming integration flyover data of a junction of an Airbus A320. The model shows good spectral resemblance for higher frequencies, with larger discrepancies at lower frequencies. The low-frequency discrepancies were attributed to beamforming limitations stemming from Rayleigh's criterion, as well as a likely over-prediction of lower frequency noise by the scaled 'H' set-up. Comparison to full-scale Reynolds number tests on a model Airbus A320 revealed the slope of the scaled noise spectrum resembled the slope of the slat noise of the Airbus A320 at full Reynolds number both at low and high frequencies.

Contrary to earlier research, the set-up without a sideplate-slat gap, 'NG', produced excess noise compared to the 'Gap'-models, 'NH' and 'H'. The excess noise is attributed to a larger spanwise extent of the slat narrow-band peak noise mechanism. The narrow-band peaks stem from a slat-cusp-to-slat-trailing-edge flow-acoustic resonance. The introduction of a side-edge (for the 'NH' and 'H' models) increases the spanwise velocity in the slat cove and creates a slat cove wake that gets accelerated over the slat track. This study showed that the altered slat cove wake shape prevents the canonical slat-cusp-to-slat-trailing-edge flow impingement from occurring on part of the slat, thus limiting the extent of the resonance mechanism. This phenomenon was portrayed by visualising the slat cove wake through total pressure isosurfaces and visualising the narrow-band peak noise source regions through a Ffowcs-Williams and Hawkings (FWH)-based source visualisation technique. A lack of loading on the slat (which is a property of the non-modified 30P30N cross-section as well) is hypothesised as the reason why the introduction of a slat side-edge does not increase the noise radiation for the models with a slat side-edge ('NH', and 'H').

Future research should validate the noise radiation spectra and the effect of the slat side-edge on the slat cove wake shape through experimental open-jet wind tunnel testing at the TU Delft's A-tunnel. Thereafter, the effect of slat loading on the junction's noise spectrum should be explored. Finally, optimised slat track and slat side-edge positioning and design studies will help characterise their influence on the narrow-band spanwise resonance destruction.

Contents

Nomenclature

List of Abbreviations

AoA	Angle of Attack
CAA	Computational AeroAcoustics
CFD	Computational Fluid Dynamics
DES	Detached Eddy Simulation
DFT	Discrete Fourier Transform
EPNdB	Effective Perceived Noise in Decibels
FFT	Fast Fourier Transform
FVM	Finite Volume Method
FWH	Ffowcs Williams-Hawkings
GCI	Grid Convergence Index
H	Horn & Smooth Stump
HLD	High-Lift Device
HSV	Horseshoe Vortex
ICAO	International Civil Aviation Organization
LBM	Lattice Boltzmann Method
LE	Leading Edge
LES	Large Eddy Simulation
MRT	Multiple Relaxation Time
MTOM	Maximum take-off Mass
NG	No Gap
NH	No Horn & Step Stump
NS	Navier-Stokes
OSPL	Overall Sound Pressure Level
PIV	Particle Image Velocimetry
POD	Proper Orthogonal Decomposition
PS	Pressure Side
PSD	Power Spectral Density
RANS	Reynolds-Averaged Navier-Stokes
RMS	Root Mean Square
SPL	Sound Pressure Level
SPOD	Spectral Proper Orthogonal Decomposition
SS	Suction Side
TE	Trailing Edge
VLES	Very Large Eddy Simulation
VR	Variable Resolution

List of Symbols

$(\cdot)'$	Fluctuating part of a parameter (-)
$(\cdot)_\infty$	Parameter in infinite/free-stream condition (-)
α	Angle of Attack ($^\circ$)
δ	Turbulent shear layer thickness (m)
δ_f	Flap deflection angle ($^\circ$)
δ_s	Slat deflection angle ($^\circ$)
δ_{ij}	Kronecker delta (-)
Λ	Aspect ratio (-)
λ	Wavelength (m)
λ_i	i'th Eigenvalue
ν	Kinematic viscosity (m^2/s)
ϕ	Sweep angle ($^\circ$)
ρ	Density (kg/m^3)
σ_{ij}	Viscous stress tensor
θ	Noise emission angle ($^\circ$)
A	Area (m^2)
b	Wing span (m)
c	Chord length (m)

c_q	Non-dimensional coefficient of paramter q (-)
c_s	Slat chord length (m)
c_{sos}	Speed of sound (m/s)
f	Frequency (Hz)
f_N	Nyquist frequency (Hz)
p	Pressure (Pa)
Re_x	Reynolds number, x-based (-)
S	Wing reference area (m^2)
St_L	L-based Strouhal number (-)
T	Temperature (K)
t	Time (s)
t_s	Signal duration (s)
T_{ij}	Lighthill's stress tensor
u, v, w	Velocities in the (x, y, z)-directions (m/s)
x, y, z	Streamwise, normal and spanwise directions (m)
y^+	Non-dimensional wall distance (-)

List of Figures

List of Tables

I

Introduction

This part introduces the research into fuselage-wing-slat junction noise. Chapter 1 presents a motivation for the study by describing the demand for quieter aviation, and contextualising fuselage-wing-slat junction noise. Chapter 2 presents the research framework and organisation. Thereafter, chapter 3 discusses the theoretical background for numerical aeroacoustics, and chapter 4 presents a brief literature review of fuselage-wing-slat junction noise.

1 Motivation

The demand for quieter aircraft and the future outlook for fuselage-wing-slat junction noise are discussed in section 1.1 and section 1.2, respectively.

1.1. Demand for quieter aviation

The number of flights for both passengers and freight has more than tripled since 1995 [1] and is expected to keep growing in the coming decades [2]. The steady rise in the number of flights disproportionally impacts airport-neighbouring communities. These communities increasingly suffer from health complications due to air and noise pollution. The International Civil Aviation Organization (ICAO) recognises the complexity of solving the different aspects of aircraft noise disturbance and has devised a balanced approach to address the problem, which includes: *(1)* Source noise reduction (aircraft), *(2)* Land use and urban development improvements, *(3)* Flight procedure improvements, and *(4)* Airport operational restrictions [3]. The research performed in this study focuses on source noise reduction.

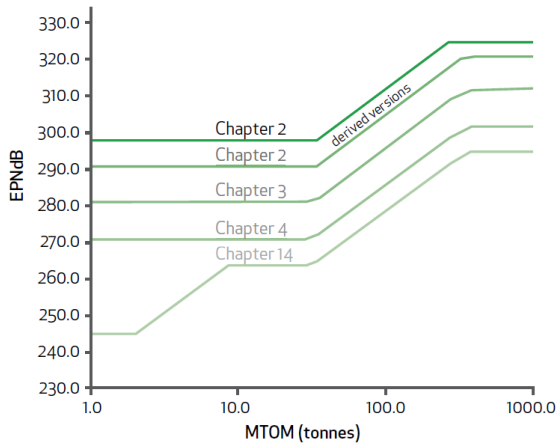

Figure 1.1: Certification points cumulative maximum noise for jet and propeller-driven aircraft, as a function of the maximum take-off mass, based on each Chapter of ICAO's Annex 16 [4]. Higher chapter numbers indicate newer regulations.

Aircraft noise regulations are dictated by the ICAO's standards, where noise is described in 'Annex 16'. The latest amendment to this annex, chapter 14, was adopted in 2017, meaning that aircraft currently in the certification process are required to comply with these latest noise requirements. The Annex 16 noise requirements are shown in figure 1.1 in terms of cumulative effective perceived noise level in decibels (EPNdB) per aircraft maximum take-off mass (MTOM), where higher chapter numbers indicate newer regulations. It shows that noise standards have become stricter over time. The noise limits also depend on the specific aircraft, its configuration, and the certification points. The points include the aircraft fly-over, sideline (lateral), and approach point, described in figure 1.2; and their cumulative (from all certification locations) limit.

Recent narrow- and wide-body aircraft, such as the Airbus A320neo and the A350, have passed the Chapter 14 noise certification with a cumulative margin of about 30 EPNdB, which means they are much quieter than the required level for all certification points (see appendix A for more details). This 30 EPNdB

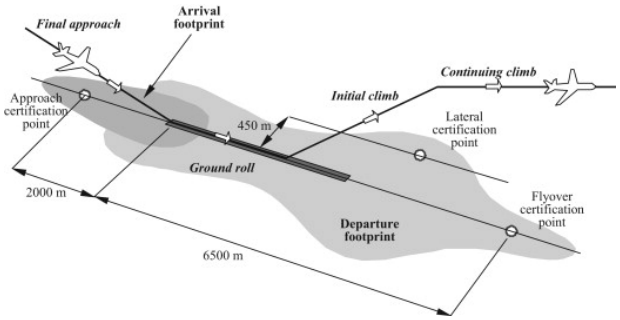

Figure 1.2: Take-off (flyover), sideline (lateral) and approach certification points definitions [3]

margin nearly equals the total required cumulative noise reduction since the first requirements were introduced (Chapters 2 to 14 in figure 1.1).

While the ICAO requirements certify the use of an aircraft, they don't reflect the unique conditions at each airport. Major European airports such as Frankfurt, Heathrow, and Schiphol are implementing noise abatement programmes that include noise quotas, noise charges, and/or quieter fleets due to societal backlash on noise pollution [5, 6, 7]. This societal pressure causes an increase in governmental scrutiny. Hence, the airports and fleets at these airports benefit from additional noise reduction solutions.

Aircraft noise reduction is mainly driven by targets set in the United States and the European Union. The two regions, respectively through NASA and ACARE, have both set out their environmental goals. Drawing direct comparisons between ACARE's and NASA's noise reduction targets is difficult as they use different references and units. Graham et al. [8] performs an example calculation on a specific aircraft to compare the regulations. NASA's noise reduction targets are more stringent than ACARE's. They strive for a reduction of 50% in 2025 and 75% between 2030 and 2035, compared to a comparable year-2000 aircraft. This indicates that between now and 2035 NASA targets an additional 50% noise reduction.

Turbofan engines with high bypass ratios, first implemented in the 1970s to conserve fuel, helped diminish aircraft noise levels by reducing the jet exhaust velocity [10, 11]. Figure 1.3 shows the thrust-corrected perceived noise levels of three engine types by entry into service date. Newer engines, with larger bypass ratios, require a lower jet exhaust velocity to generate the same amount of thrust as a larger volume of air is displaced. This noise reduction trend, caused by lower jet noise, however, shows signs of diminishing returns and may even reverse due to increased fan noise from larger bypass ratio engines. Additionally, as jet noise decreases, airframe noise becomes more dominant, especially during approach [11], due to idle engines, and the deployment of high lift devices (HLDs) and landing gears. Figure 1.4 displays the main noise contributors of a typical 250-passenger aircraft during take-off and approach. In approach configuration, the fan and airframe have become the dominant noise contributors, instead of the jet exhaust.

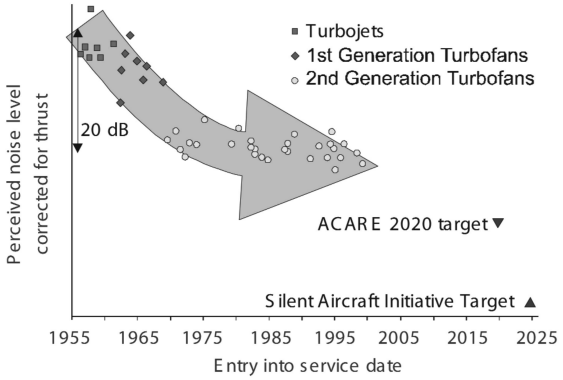

Figure 1.3: Perceived aircraft noise levels by entry into service year for different engine types [9]

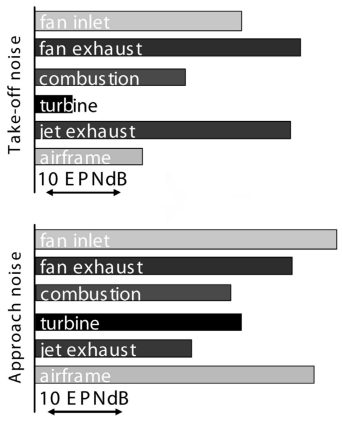

Figure 1.4: Main noise contributors for a typical 250 passenger aircraft, adapted from [9]

1.2. Fuselage-wing-slat junction noise: outlook

Airframe noise reduction has been a subject of studies for at least 50 years. Dobrzynski [10] summarises that many of these studies focused on either the high-lift devices or the landing gears. Recently, researchers have shown increased interest in noise caused by local three-dimensional flow phenomena. One such sparsely researched location is the fuselage-wing-slat junction in approach configuration, illustrated in figure 1.5. Noise source localisation results from fly-over measurements show that the inboard slat [12], and the junction between the slat, wing and fuselage [13, 14] represent a significant localised noise source across the frequency spectrum on commercial aircraft such as the Airbus A340 and A320. Some studies refer to the fuselage-wing-slat junction noise as 'slat horn noise'. However, the slat horn component refers to a hornlike protrusion that smoothly merges the slat and wing when the slats are retracted. The author favours the phrase 'fuselage-wing-slat junction noise', given that the impact of the various aero-structure surface shapes and orientations on noise radiation remains a topic of discussion.

The effectiveness of noise reduction technologies for airport-neighbouring communities relies on their industrial adoption. A principal aircraft design driver is fuel efficiency [16, Chap. 7.2]. Improved fuel efficiency reduces the overall aircraft mass, reduces operational expenses and helps lower greenhouse gas emissions. Since 1960, aviation has become eight times more efficient in terms of fuel usage per paying customer per kilometre, mostly attributed to engine and wing improvements [17]. In recent years, however, most of the fuel efficiency improvements stem from either the seat density and seat utilisation improvements, accounting for 49% of the total fuel reduction achieved between 2005 and 2019 [18]. These factors are nearing their limits and future fuel efficiency improvements will have to be attained differently.

IATA [15] reports that many new aircraft projects with modified wings or engines were launched between 2014 and 2020. Engine manufacturers will optimise the current turbofan technology, but the improvement rate due to higher bypass ratio engines is slowing down because the increased drag from the engines constrains future efficiency gains. Next-generation aircraft designs are introduced once every 15 to 20 years, therefore the author expects only modest aircraft platform or engine innovation until 2030. Figure 1.6 illustrates the expected introduction period for new aircraft and engine concepts. This decade will likely revolve around local airframe modifications to the conventional tube & wing design to improve fuel efficiencies.

The only potential conventional airframe change that could render a fuselage-wing-slat abatement solution obsolete, according to IATA [15], would be the introduction of a laminar wing. Such a design cannot have slats, as slats trigger turbulent flow structures. Researchers conducted and analysed a series of experiments and flight tests on laminar flow wings in the 1990s, using linear stability theory to create design guidelines for these wings [19]. Schrauf [20] and Shi et al. [21] showed that commercial narrow-body and wide-body aircraft, such as the Airbus a320 and A350, would need novel suction systems on the whole wing for laminar flow to work. Such a system has never been conceived on an aircraft's main wing of this size class. Therefore, the author thinks that laminar wings are unlikely to appear in the 2020s, especially for aircraft in the A350 or A320 size categories.

The fuselage-wing-slat junction is a localised airframe noise source, and it is likely to persist on most commercial aircraft for the foreseeable future. This makes it a worthwhile candidate to investigate the relationship between the aero-structural design and the aeroacoustic footprint.

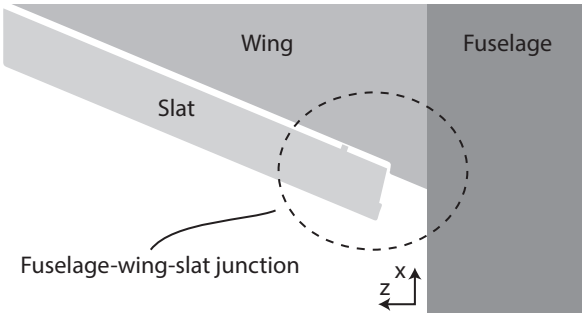

Figure 1.5: Schematic representation of a fuselage-slat-wing junction

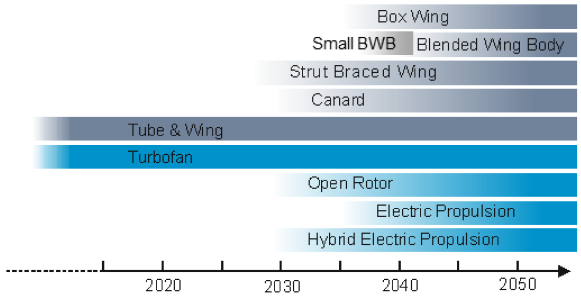

Figure 1.6: Potential timeline for the introduction of new aircraft (grey) and engine (blue) concepts [15].

2

Research framework and organisation

This chapter describes the research framework, detailing the objective in section 2.1 and questions in section 2.2. An outline of the report is presented in section 2.3.

2.1. Research objective

This study tries to establish a link between design choices in the fuselage-wing-slat junction, and the effect on its aeroacoustic footprint. More specifically, the objective of this study is

> ***To describe the relation between the design of a fuselage-wing-slat junction's aero-structure, and its aeroacoustic footprint*** *by investigating noise radiating flow-surface interactions for various junction geometries in approach configuration.*

2.2. Research questions

The study is guided by two sets of research questions. Each research question is subdivided into multiple sub-questions. The first question involves creating a research set-up for studies on a fuselage-wing-slat junction. The second question focuses on characterising the noise from the developed research models.

RQ 1

*What is a suitable **scaled research model** that represents the aeroacoustic characteristics of a full-scale fuselage-wing-slat junction while being compatible with open-jet wind tunnel experiments?*

- *1.1 What are suitable **airfoil cross-sections** for the scaled model?*
- *1.2 Which **geometrical features** from commercial aircraft ensure that the scaled model represents the aeroacoustic characteristics of a fuselage-wing-slat junction?*
- *1.3 What design considerations and adaptations need to be implemented to ensure the scaled model is **suitable for open-jet wind tunnel** experiments?*

RQ 2

*What are the **aeroacoustic characteristics** of the scaled fuselage-wing-slat junction model, and how do these characteristics compare to previous research findings?*

- *2.1 What is the effect of large- and small-scale **turbulent structures** originating near the fuselage-wing-slat junction on surface pressure fluctuation intensities and flow patterns in the set-up?*
- *2.2 To what extent does **impingement from turbulent structures** on the surfaces near the junction contribute to the far-field noise of the model?*
- *2.3 To what extent do the junction's turbulent structures influence the **aeroacoustic characteristics in the slat cove** of the model?*
- *2.4 To what extent are the noise radiation and turbulent flow structures of the model **comparable to results from other scaled research models**?*
- *2.5 To what extent is the noise radiation of the model **comparable to results from flyover full-scale measurements**?*

2.3. Report outline

The report is structured in three parts. To quickly navigate between the parts and chapters, clicking on any page number will automatically redirect the viewer to the contents page (digital only).

Part I introduces the the topic and research framework in chapter 1 and chapter 2, respectively. Additionally, a theoretical background for numerical aeroacoustics is provided in chapter 3, after which a short literature review on fuselage-wing-slat junction noise is presented in chapter 4.

Part II describes the fuselage-wing-slat junction research set-up, including the geometry in chapter 5, and the numerical domain in chapter 6. The set-up is verified for grid independence, and validated against literature in chapter 7. At the end of this part, in chapter 8, the results of the research on the aeroacoustics of a fuselage-wing-slat junction are presented. The main message of this part is provided in article format in appendix B. At the time of writing the manuscript is being prepared for journal submission.

Part III presents the concluding remarks of the report including the conclusions, addressing the research questions, in chapter 9, and recommendations for future research in chapter 10.

3

Theoretical background for numerical aeroacoustics

This chapter briefly introduces the concept of aeroacoustics in section 3.1, after which numerical research through computational fluid dynamics will be described in section 3.2. The concepts are then combined by discussing hybrid numerical aeroacoustic analysis through the introduction of the acoustic analogy in section 3.3. Lastly, useful measurements and methods used for aeroacoustic analyses are introduced in section 3.4.

3.1. Introduction to aeroacoustics

The airframe is a typical example of a noise source where aeroacoustics – i.e. acoustic radiation due to unsteady movements of air itself, and their interaction with stiff bodies – plays the largest role [22]. In aeroacoustics, the noise radiation depends on two factors: *(1)* the formation of turbulent structures, and *(2)* the way these turbulent structures interact with a surface. To understand the physical phenomenon of noise radiation, it is essential to know how kinetic energy is converted into an acoustic pressure wave (noise/sound). Lighthill reformulated the standard Navier-Stokes equations [23, 24] of mass and momentum into a wave equation for density fluctuations (or pressure in a perfect gas) [25, 26]. This reformulation helps describe which phenomena in a flow are sources of noise. Lighthill's equation in Einstein notation is given in eq. (3.1).

$$\frac{\partial^2 \rho}{\partial t^2} - c_0^2 \nabla^2 \rho = \frac{\partial^2 T_{ij}}{\partial x_i \partial x_j} \tag{3.1}$$

where ρ is the density, c_0 is the speed of sound in the quiescent medium, and T_{ij} is the Lighthill stress tensor, defined as:

$$T_{ij} = \underbrace{\rho v_i v_j}_{\text{Reynolds stress}} + \underbrace{\sigma_{ij}}_{\text{viscous stress}} - \underbrace{(p - c_0^2 \rho)\delta_{ij}}_{\text{excess pressure}}$$

where v_i, v_j are the velocity fluctuations in streamwise and transverse directions, σ_{ij} is the viscous stress tensor, p is the pressure, and δ_{ij} is the Kronecker delta.

The left-hand side describes the development of an acoustic wave, and the right-hand side describes the source terms, which, in flows free of external forces or mass injections, are all encapsulated by Lighthill's stress tensor. The main source of noise (for low Mach numbers) is the Reynolds stress [27], which is the nonlinear exchange of momentum between adjacent layers in the flow due to turbulence. These turbulent stresses can physically be attributed to the interaction of various eddies in the flow, which have different sizes and velocities. These stresses, through compressibility in the flow, must radiate quadrupolar noise (as described in the subsequent section). The viscous stress deals with the molecular transport of momentum. It is a source due to viscous energy losses most active in places of high stretching and shearing of eddies in the flow. The excess pressure term is a term that accounts for non-ideal fluids [28] and acoustic self-modulation, i.e. sound waves can modify the local pressure and density of the fluid which then act as a noise term themselves. This term is mostly important in high-pressure flows, e.g. pressure waves [27]. The size of the interacting eddies relates to the frequency of the sound. One might compare this interpretation with the concept of inertia in rigid bodies: larger structures cause slower oscillations. Therefore, having eddies of all sizes means having acoustic energy of all frequencies: broadband noise. This also means that thicker shear layers, which contain larger eddies, produce lower peak-frequency broadband sound. Note that free turbulence, as described by Lighthill, can at most be a quadrupole noise field [29], which, for low Mach flow, attenuates quicker than dipole noise sources stemming from

forces on the flow [30]. The fuselage-wing-slat junction is likely dominated by dipolar noise sources from flow-structure interactions. An expansion of Lighthill's aeroacoustic sources also takes flow-structure interactions into account and is described in subsequent sections.

Simplified physical description of acoustic (multi-)poles
Monopoles, dipoles and quadrupoles are sources that radiate sound in different directional patterns. A monopole radiates sound equally in all directions. It occurs when a volume expands or contracts (a mass injection), forcing the creation of alternating density (and pressure for a barotropic fluid) crests and troughs in the fluid. Kinetic energy, through this compressibility, is transformed into a form of potential energy which is released and radiated as an acoustic wave to the far-field. A small object that scatters a pressure wave with a wavelength much larger than its dimensions can be approximated as a monopole (compactness). A dipole radiates sound as two monopoles with opposite polarity. It can be described as an object oscillating back and forth in a compressible fluid, creating concurrent high-pressure and low-pressure poles on each side through the pushing and pulling of the volume. Any force gradient will "push" on the flow and hence must radiate dipolar sound. A quadrupole resembles two dipoles close to each other that oscillate in opposite phases. It is caused by stresses in the fluid, which are in essence two internal forces that act in opposite pairs to maintain equilibrium. A shear stress, which is parallel to the plane of action, will thus result in a lateral quadrupole. The directivity patterns for the different sources are shown in figure 3.1.

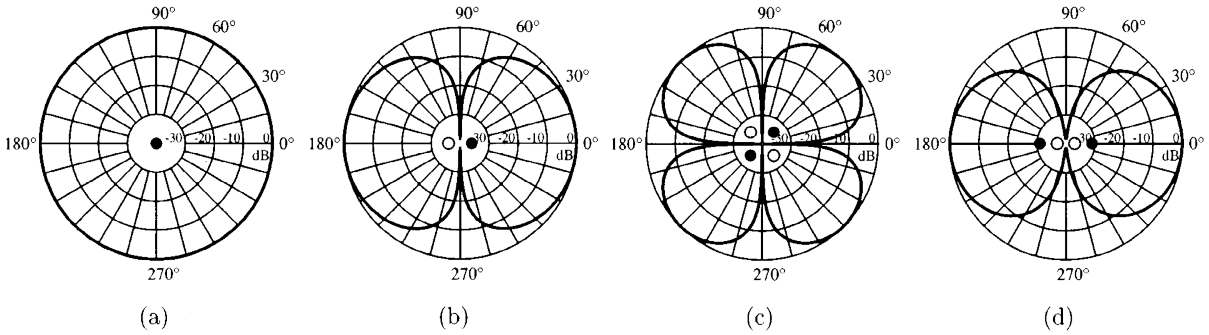

Figure 3.1: Theoretical directivity pattern for acoustic (multi-)poles: (a) monopole, (b) dipole, (c) lateral quadrupole, and (d) longitudinal quadrupole [31].

3.2. Computational fluid dynamics for aeroacoustics

Flow properties result from physical interactions of (groups of) fluid particles at the molecular level [32], which is a multi-scale problem. Multiple numerical methods exist to model the flow properties in a domain. Computational Fluid Dynamics (CFD) methods can be classified into Lagrangian and Eulerian methods, depending on how they describe the fluid motion [32]. A common Eulerian method is the finite volume method (FVM), which applies the NS equations on a grid and models the fluid as a continuum. A FVM is often used by RANS, DES, and LES methods to solve the NS equations for each grid cell. Another method is the lattice-Boltzmann method (LBM), which is a mesoscopic method that models the fluid as a collection of particles that move and collide on a lattice until a thermodynamic equilibrium is reached. The macroscopic properties of the fluid are derived from the microscopic motion and momentum exchanges [32]. LBM is suitable for complex 3D transient phenomena such as aeroacoustic studies, as it is easily parallelised on multiple processors, can handle boundaries directly with bounce-back rules, use multiple relaxation time (MRT) models to adjust properties such as energy, momentum, or stress independently, and avoid some numerical errors (less dissipation and dispersion) that affect NS methods [33]. Therefore, LBM is a logical candidate for studying the fuselage-wing-slat junction, which involves complex 3D flow phenomena such as separation, vortex shedding, and noise generation. Previous studies have shown that LBM with very large eddy simulation (VLES) in PowerFLOW® software can produce accurate results for similar problems [34, 35].

Computational aeroacoustics (CAA) is a branch of CFD that focuses on the numerical simulation of sound generation and propagation in a fluid. The acoustic information at a certain location can be extracted either through direct or hybrid noise calculations [32]. Direct noise calculations require resolving the acoustic information at the locations of interest in high resolution and with high frequency. This is

computationally expensive, especially for high-frequency noise. Hybrid CAA first computes the aerodynamic fluctuations using a CFD method on a smaller domain, surrounding the sources, then propagates the acoustic information to the far-field using an acoustic analogy (section 3.3).

The planned fuselage-wing-slat study can use hybrid aeroacoustic methods for many of the analyses once the results from these methods are validated against several direct measurement probes in the flow.

3.3. The acoustic analogy

The FWH equation enables the calculation of far-field noise using flow properties derived in the near-field. It greatly reduces the numerical domain discretisation otherwise needed to obtain accurate results for far-field noise. The equation is provided in eq. (3.2) [36]. This section aims to give an overview of the different source terms, and how they impact he noise radiation of a system.

$$\underbrace{\frac{\partial^2 \rho' H_s}{\partial t^2}}_{L} - \underbrace{c_\infty^2 \frac{\partial^2 \rho' H_s}{\partial x_i^2}}_{C} = \underbrace{\frac{\partial^2 T_{ij} H_s}{\partial x_i \partial x_j}}_{S_{\text{stress}}} - \underbrace{\frac{\partial}{\partial x_i}(\rho v_i (v_j - V_j) + \sigma_{ij}) n_j \delta(f) |\nabla f|}_{S_{\text{loading}}} + \underbrace{\frac{\partial}{\partial t}(\rho v_j - \rho' V_j) n_j \delta(f) |\nabla f|}_{S_{\text{thickness}}} \quad (3.2)$$

Left-hand side terms: The density wave equation

- L: The **local changes** in unsteady density fluctuations describing the temporal evolution of the wave.
- C: The **convective effects** of the fluid motion describing the spatial evolution of the wave, where c_∞ is the speed of sound and x_i are the spatial coordinates.

Right-hand side terms: The source terms

- S_{stress}: The quadrupole sources, which are volume **free turbulence stress sources** described by the Lighthill stress tensor T_{ij}.
- S_{loading}: The dipole sources, which are surface sources due to the interaction of the fluid with solid boundaries or moving surfaces, described by the fluid density and velocity ρv_i, the viscous stress tensor σ_{ij}, and the normal vector to the surface n_j. This term is also called the **loading source term**, accounting for the unsteady loading exerted by a body. For non-compact sources in low Mach number flow (likely present in the fuselage-wing-slat junction), the dipole noise radiation magnitude far exceeds the other two terms.
- $S_{\text{thickness}}$: The monopole sources, which are surface sources due to the volume changes or mass injection at the surface, are described by the difference between the fluid momentum and the surface momentum $\rho v_j - \rho' V_j$. This term is also called the **thickness source term**, accounting for the fluid displacement.

The noise generation of the fuselage-wing-slat junction likely mostly stems from the loading term. This term is dictated by the upwash velocity fluctuations interacting with the body.

3.4. Measurements and methods used in aeroacoustic analyses

This section outlines the key methods and variables that help describe the noise and noise mechanism in the fuselage-wing-slat junction. Some of the variables and methods will be mentioned in the literature review in chapter 4, or they will be used for the numerical analysis of the fuselage-wing-slat junction.

3.4.1. Pressure fluctuation measurements and analyses

Pressure fluctuations can be measured on surfaces, or in the flow. Microphones on surfaces help identify areas of high surface pressure fluctuation intensity, which often indicate turbulent flow impingement, causing dipole noise. Near-field flow pressure frequency spectra help describe the energy distribution of the eddies of different sizes. Far-field spectra describe the actual radiated noise.

Sampling frequency

Spectral analysis of pressure fluctuation $p'(t)$ measurements decompose the time-varying signal into its frequency components using a discrete Fourier transform (DFT). The lowest observable frequency and

the frequency bandwidth are determined by the frequency resolution of the DFT, $\Delta f = 1/t_s$, where t_s is the total duration of the signal. The highest frequency that can be resolved by the DFT is the Nyquist frequency $f_N = 1/2\Delta t$, where Δt is the sampling interval. The sampling frequency should be at least twice the highest expected frequency in the measured set-up to capture all relevant spectral components from a source. In practice, this factor should be even higher to capture the intensity of the highest frequency noise adequately. This is important for designing an adequate numerical aeroacoustic simulation. The DFT can be efficiently computed using a fast Fourier transform (FFT) algorithm, which reduces the computational complexity from $\mathcal{O}(N^2)$ to $\mathcal{O}(N\log N)$.

Frequency comparisons

Comparing the amplitude of different sound signals requires either the use of the same bandwidth (hence sampling time) or dividing the signals by the bandwidth to compare the noise in dB/Hz. Often, however, the dimensionality of the data is too high for straightforward comparisons. A common method for evaluating the frequency response is to apply octave band or 1/3$^{\text{rd}}$-octave band filters. The centre frequency of each octave band is twice that of the preceding one ($2 \cdot f_c$), and the centre frequency of each 1/3$^{\text{rd}}$-octave band is two to the power one-third that of the preceding one ($2^{1/3} \cdot f_c$). Lastly, the successive frequency bands and their sound pressure levels (SPL(f_i, θ)) can be used to calculate the overall sound pressure level: OSPL$(\theta) = 10\text{log}\ \sum_{i=1}^{n} 10^{\text{SPL}(f_i,\theta)/10}$.

In this report, all frequency data is processed using PowerAcoustics using the static pressure data. It segments the original time signal into several windows, which are later averaged using Welch's method to obtain a smoother representation of the frequency response. The window width used is an exact product of powers of 2, 3, and 5, and each window is less than 25% of the total number of available frames, i.e. $N_{\text{frames, w}} = 2^a \cdot 3^b \cdot 5^c \mid N_{\text{frames, w}} < 0.25 \cdot N_{\text{frames}}$. The product of powers of 2, 3, and 5 is used to improve the efficiency of the fast Fourier transform (FFT). Additionally, an overlap percentage of 50% between the windows is employed, resulting in at least eight averaging windows. The windowing and frame count result in a smooth output sound power (SPL). The resolution/bandwidth is equal to the minimum frequency of a window, i.e. $\Delta f = 1/t_{window}$. The results are exported in dB format using a reference pressure of $p_{ref} = 2.0 \cdot 10^{-5}$ Pa using

$$N_{dB} = 20\text{log}_{10}\left(\frac{p_s}{p_{\text{ref}}}\right) \tag{3.3}$$

where p_s is the static pressure. For all upcoming analyses, a Hanning window was used. When it is applied to a signal, it modifies the signal such that the total power is reduced to $\frac{3}{8}$ of the original power. This is due to the nature of the Hanning window function, defined as $w(x) = 0.5(1 - \text{cos}(2\pi x))$, which damps the edges of the signal. Squaring this function and integrating it over the interval from 0 to 1 yields $\frac{3}{8}$:

$$\int_0^1 (0.5(1 - \text{cos}(2\pi x)))^2 dx = \frac{3}{8}$$

This integral represents the total power of the window function. To restore the total power of the signal to unity (i.e., the original total power), the windowed signal is multiplied by the reciprocal of this value, which is $\frac{8}{3}$.

Frequency scaling

Noise often scales with the size of the turbulent flow structures that cause the noise radiation. For example, in trailing edge noise, the frequency of the noise radiation depends on the size of the turbulent eddies in the boundary layer, as does the magnitude. These sizes scale with the boundary layer thickness, which generally depends on the length of the object and the Reynolds number. The sizes of eddies in the mean shear lines in a slat cove also scale with the slat size, therefore the frequencies of the noise caused by shedding scale with the slat chord. In scaled aeroacoustics, it is often useful to non-dimensionalise the frequencies with respect to a characteristic length scale L that is proportional to the size of the turbulent structure of the noise source, and a characteristic velocity U, often the free-stream velocity, as it affects the flow propagation and the size of the turbulent flow structures. This type of non-dimensionalisation is called Strouhal St scaling.

$$St_L = \frac{fL}{U} \tag{3.4}$$

Pressure fluctuation intensity
To investigate the pressure fluctuation intensity at a certain location, the (band-passed filtered) root mean square of the static pressure fluctuations is calculated, or, equivalently, the standard deviation of the static pressure itself:

$$p'_{rms} = \sqrt{\frac{1}{n}\sum_{i}^{n} p_i'^2} = \sigma(p) = \sqrt{\frac{1}{n}\sum_{i}^{n}(p_i - \mu(p))^2} \tag{3.5}$$

Coherence
The spatial coherence of a noise source influences the noise magnitudes near e.g. straight edges, and in resonance mechanism. It is expressed with regard to a predefined reference signal. The normalised magnitude-squared spatial coherence of a parameter q between a reference location 0 and other locations can be defined as:

$$\gamma^2_{q_0 q}(f) = \frac{|\Phi_{q_0 q}(f)|^2}{\Phi_{q_0 q_0}(f)\Phi_{qq}(f)} \tag{3.6}$$

where $\Phi_{qq}(f)$ denotes an auto-spectral density and $\Phi_{q_0 q}(f)$ a cross-spectral density [37].

Source visualisation
An array of far-field microphones allows for noise source visualisation per frequency through acoustic beamforming [38]. The SPL at each location can be visualised as a heat map by comparing the pressure-time data of the microphones in an array through an algorithm, e.g. 'delay and sum'. By integrating the SPL rom specific regions within the beamforming data, the noise radiation between different sections can be distinguished.

A novel FWH-based noise source visualisation technique is based on the individual contribution of numerical surface cell's pressure fluctuation to the noise at a specified far-field location using the Ffowcs-Williams and Hawkings (FWH) equation [39, 40]. The method can differentiate which part of the surface contributes to the noise constructively (in phase) and which part of the surface contributes destructively (out of phase) per frequency band. The method is hence also capable of describing the coherence of different source locations with respect to the microphone per frequency.

Spectral Proper Orthogonal Decomposition
A set of fluctuating (zero-mean) stochastic measurements can be described with a sum of orthogonal basis functions (eigenmodes), assuming that the measurements of the phenomenon belong to a Hilbert space, i.e. the inner product of the measurement space follows the inner product properties of a Hilbert space [41]. Proper Orthogonal Decomposition (POD) generates spatial eigenmodes that can be ranked by the eigenvalues, i.e. $\lambda_1 \geq \lambda_2 \geq ... \geq 0$, where the eigenvalues indicate the average energy of eigenmodes, and the sum of eigenvalues give the total energy of the process, hence completely describe the process. The primary features of a measurement domain are captured in the first few eigenmodes, as they are ranked. Spectral POD (SPOD) expands the analysis to spatial-temporal eigenmodes, which allows for the decomposition of the eigenmodes per frequency. This decomposition can be used to analyse the primary features of a measurement domain per frequency and to determine to what extent the domain is coherent and periodic for certain frequencies, i.e. a high ratio of the first eigenvalue to the sum of eigenvalues.

In this study, the SPOD analysis is performed by the commercial Opty-dB suite of PowerFLOW, which is based on the work from Towne et al. [41].

3.4.2. Velocity measurements and analyses

In numerical studies, the velocity can be captured for every timestep in each grid cell, in all three spatial directions: $\boldsymbol{U} = [u\ v\ w]'$. This information can be used to calculate other flow properties, as well as visualise the flow direction through streamlines. These flow properties help describe the turbulent flow structures causing the noise radiation.

Vorticity
The spatial velocity field allows for the construction of the velocity gradient tensor $A = [\nabla u\ \nabla v\ \nabla w]'$, which represents the spatial derivatives of the velocity components. The velocity gradient tensor can be decomposed, $A = S + \Omega$, into its symmetric part (the rate-of-strain tensor) $S = \frac{1}{2}(A + A^T)$, and its antisymmetric part $\Omega = \frac{1}{2}(A - A^T)$ (the vorticity tensor). Hence, from the velocity gradient tensor, the

vorticity components can be constructed. Vortical energy is indicative of noise source locations both in the free-field, and near geometries where vortical structures impinge on the structure.

Vortical topology

The rate-of-strain tensor and vorticity tensor can be used to identify vortex structures in turbulent flows. The λ_2-criterion is a method for identifying vortex cores in turbulent flows. It is based on the second eigenvalue of the sum of the squares of the strain rate and vorticity tensor:

$$\lambda_2 = \text{eig}_2(S^2 + \Omega^2) < 0 \tag{3.7}$$

A negative second largest eigenvalue (λ_2) of the $S^2 + \Omega^2$ tensor indicates that the vorticity is strong enough to counteract the strain along one of the principal axes of the strain tensor, indicating the presence of a stable vortex core [42]. Jeong and Hussain [42] shows that the Q-criterion, another common method to identify vortex structures, and λ_2-criterion are linked via the eigenvalues of the $S^2+\Omega^2$ tensor: $Q = -\frac{1}{2}(\lambda_1+\lambda_2+\lambda_3)$. Hence, the Q-criterion identifies a vortex core based on the sum of the eigenvalues being negative, whereas the λ_2-criterion identifies a vortex core based on the second (and third) eigenvalue being negative. Jeong and Hussain [42] state that the definition of the λ_2-criterion is better at excluding non-vortical regions and pressure minima at walls. Additionally, Jeong and Hussain [42] showed that the λ_2-criterion was the best and most consistent in representing the topology and geometry of vortex cores among a multitude of vortex identification criteria.

Velocity visualisations, vorticity strength and vortex identification will help describe the flow phenomena in the junction and slat cove, which is relevant to determine how they influence the noise radiation of the junction.

4

Literature review of the fuselage-wing-slat junction

This chapter aims to provide a short perspective on the influence of the fuselage-wing-slat junction noise compared to the total airframe noise in approach configuration. Section 4.1 analyses the main noise sources for commercial aircraft, focusing on the Airbus A320, in approach configuration. Additionally, the section gives a high-level overview of the knowledge of slat and junction noise. Section 4.2 continues the discussion on fuselage-wing-slat junction noise by describing the geometric features and design requirements for the different components in the junction. Thereafter, section 4.3 reviews the sparse number of existing studies that specifically research the aeroacoustic phenomena in the junction. The chapter is concluded by section 4.4 which describes the significance of fuselage-wing-slat junction noise, and the research gaps in the available literature.

4.1. Junction noise in the context of airframe noise

First, a breakdown presenting the relative airframe noise contribution of different locations throughout the frequency spectrum is discussed. It is impossible to fully differentiate some airframe regions in such studies. Therefore, secondly, a brief introduction to slat noise, slat track noise, and inboard slat noise is presented.

4.1.1. Noise comparison of airframe regions

Full-scale tests have consistently identified the fuselage-wing-slat junction as a region of significant apparent noise sources during approach. This was first demonstrated by Piet et al. [12], who used noise visualisations from fly-overs to highlight the high noise levels produced by the high-lift devices, including the inboard slat at certain frequencies. Later, Sijtsma and Stoker [13] conducted a study on a full-scale A340 aircraft and found that the noise from the fuselage-wing-slat junction was one of the main local noise sources, both in terms of peak and average sound power level (PWL) in dB(A). They also observed that high lift devices (HLDs) have a greater impact on smaller aircraft, such as the A320, with the slat playing a particularly important role. This was further confirmed by Siller et al. [14], whose noise visualisations reveal a high amplitude broadband noise near the fuselage-wing junction (e.g. figure 4.3 for a single frequency). To put that into perspective, Siller et al. [14] investigated an Airbus A320 in-flight with idle engines and retracted landing gear to identify noise sources of various high-lift devices in approach configuration. The spectral radiation of a single flyover for different noise emission angles is shown in figure 4.1, where the emission angles are defined as in figure 4.2. Siller et al. [14] included the fuselage-wing-slat junction noise as ‘slat horn’ noise. A few observations can be made:

- At lower frequencies (**250-1000 Hz** range), the **slat** is the loudest source with a slight directivity towards overhead and backwards, followed by the flaps and engine nozzles. The fuselage-wing-slat junction noise is evident at 400 Hz with a forward directivity, and gaining relative importance towards the 1000 Hz.
- In the **1000-1600 Hz** band, the **slats**, **fuselage-wing-slat junction** and **flaps** have comparable noise levels. The flap side-edge starts to radiate relatively more noise at this frequency.
- In the **1600-2000 Hz** range slats and junction noise are still comparable. In this frequency band, the dominant noise source is starting to move towards the **idle engine noise** (inlet and nozzle).
- In the **2000-3150 Hz** band, the **engine nozzle** is a noticeable source of tonal noise with a directivity in the overhead direction. This is likely due to a low-pressure turbine tone and its harmonics from the last two stages of the engine [14].

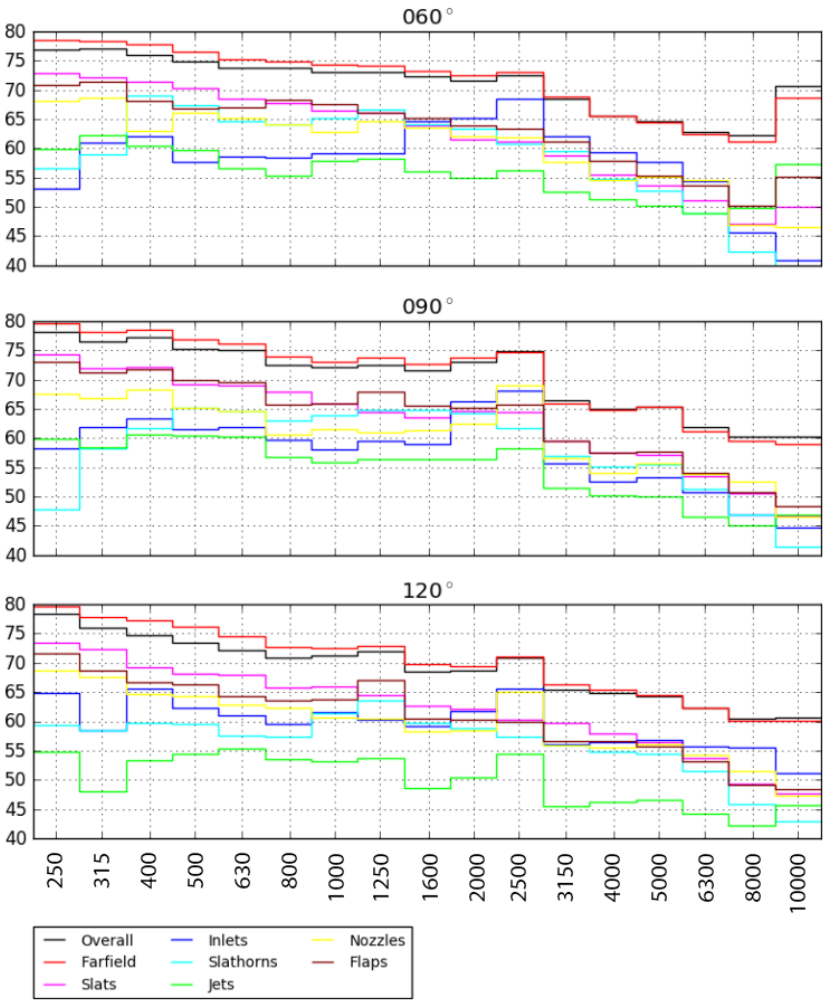

Figure 4.1: Spectral source breakdown of an Airbus A320 in approach configuration (with retracted landing gear) adapted from [14]. The y-axis represents the SPL (dB) and the x-axis shows the sound frequency (Hz).

- Above **3150 Hz**, the inlet, slats, fuselage-slat-wing junction and flaps have similar noise levels to each other, omnidirectional. The overall **noise levels are lower than at lower frequencies**.

These observations suggest that the fuselage-wing-slat junction generates a comparably loud noise as the

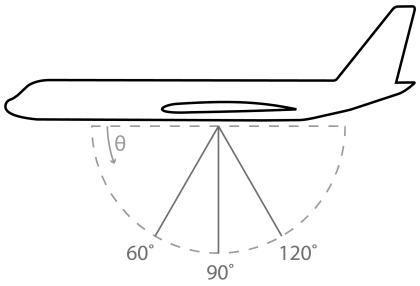

Figure 4.2: Definition of noise emission angles from a source

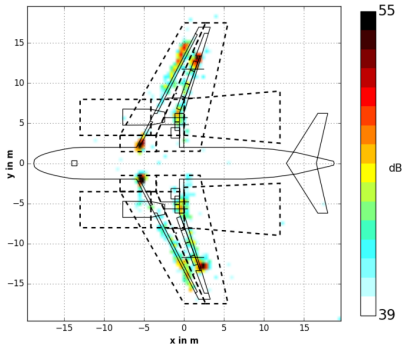

Figure 4.3: Noise source visualisation example of an Airbus A320 at $\theta = 60°$ at 1000 Hz [14].

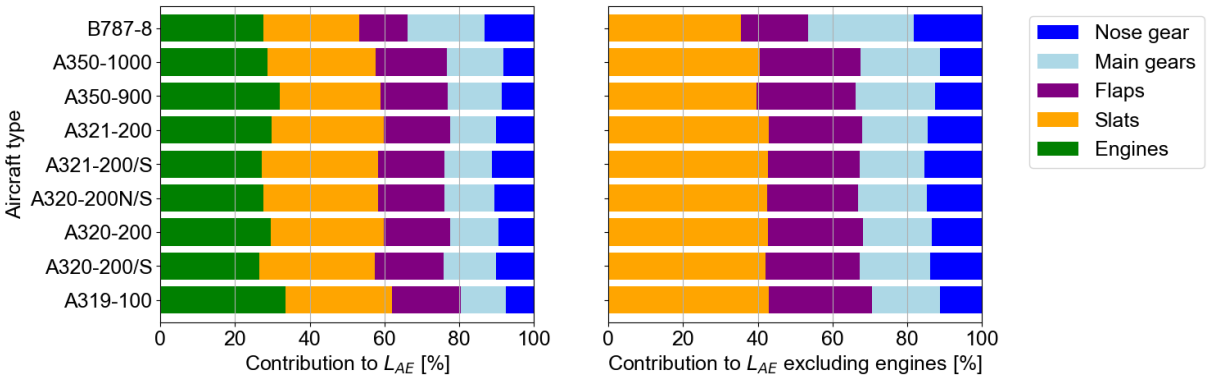

Figure 4.4: Relative contribution of aircraft noise components from several aircraft derived from beamforming integration areas, adapted from [45].

other loud airframe components, such as the slats, inlets, flaps, and nozzles among multiple frequency bands in approach configuration. Hence, reducing the junction noise will likely have a moderate yet measurable impact on the overall noise radiation. For example, in the $60°$ direction, taking the data from figure 4.1, a reduction of 3 dB of the 'slathorns' would lead to a ~ 0.34 dB reduction in the OSPL. Eliminating the fuselage-wing-slat junction noise would reduce the noise by ~ 0.71 dB. Details on the calculations are provided in appendix C. This outcome exemplifies that a holistic airframe noise reduction approach is necessary for industrial applications.

On final approach, the landing gears are deployed. Separating the noise from the deployed main landing gear in approach formation from the other sources (engines, flaps, and slats), however, is challenging due to the resolution constraints of Rayleigh's criterion [43]. Therefore, few studies include the main landing gear, flaps, and slats separately in their component-wise analysis. One such study by Takaishi et al. [44] uses domain integration of the acoustic map generated by a beamforming algorithm with data from a 30 m diameter microphone array setup. Ikuta [45] used the data acquired by Takaishi et al. [44] to analyse a multitude of airframes in terms of component OSPL in the overhead direction. Figure 4.4 shows the relative noise contribution per component of Airbus A320 and A350 variants, along with the Boeing 787-8 for comparison. The OSPL from the integrated beamforming data from Ikuta [45] suggests that Boeing's noise profile differs significantly from both Airbuses and that Airbus' slats dominate the total noise in approach.

From the available literature, it can be concluded that the contribution of the high-lift devices to the total noise is dominant for Airbus aircraft in approach configuration. The noise profile is broadband and omnidirectional. The slats offer the largest noise reduction potential, particularly at lower to mid-frequencies as they are the largest relative contributor at those frequencies. Damping the radiation from the fuselage-wing-slat junction will likely have a moderate, yet measurable effect on the OSPL of an Airbus A320 in approach configuration, which makes it worthy of further investigation.

4.1.2. Slat and junction noise mechanism

Slat noise from a 2.5D airfoil cross-section consists of multiple noise source generation mechanisms, which Choudhari and Khorrami [46] have schematically illustrated (figure 4.5). The cove (cavity, and impingement), the slat gap (TE turbulence radiation, vortex shedding, and main element impingement), the slat features (incidence, upper side curvature, chord length) and the slat edges (lateral flow separation due to pressure jumps) are the main factors that influence the noise generation [3]. Lu et al. [47] summarises the latest research into the noise generation mechanisms. The noise produced by the slat can be classified into three main types: low to mid-frequency broadband noise (corroborated by Takeda et al. [48] and Dobrzynski et al. [49]); narrow-band noise with multiple discrete frequencies on top of the low-mid-frequency broadband noise, which is thought to be caused by the cove's cavity-like geometry eliciting lower frequency discrete tones between 1 kHz and 3 kHz similar to Rossiter modes (corroborated by Dobrzynski et al. [49], Kolb et al. [50], and König et al. [51]); and high-frequency hump noise due to the vortex shedding at the trailing edge (corroborated by Storms et al. [52], Khorrami et al. [53] and Takeda et al. [54]). Figure 4.6 shows a schematic representation of the typical slat noise spectrum. The main sources of slat noise are located in the cove region near the trailing edge and close to the reattachment zone, where the turbulence

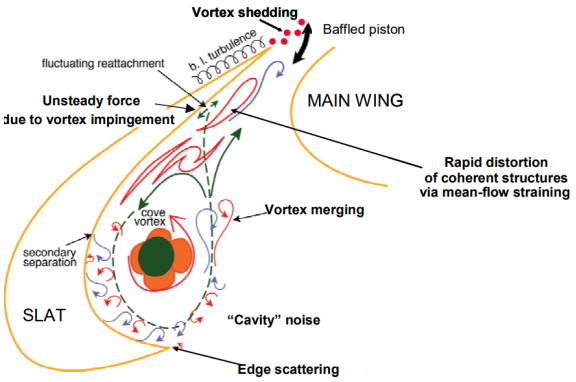

Figure 4.5: Sources and physical mechanisms behind noise generation of a slat [46]

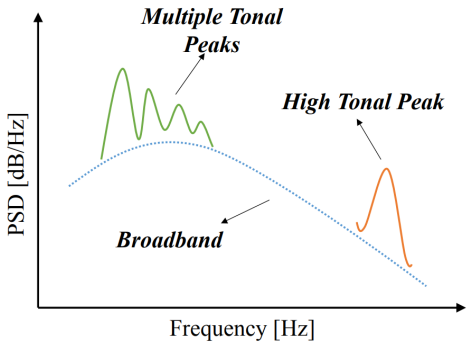

Figure 4.6: Typical slat noise spectrum [56]

and pressure fluctuations are most intense [55]. The forces and stresses on the turbulent structures at the impingement zone transform kinetic energy into acoustic energy.

The influence of **slat tracks** and slat track cut-out has received less academic attention. Murayama et al. [57, 58] used wind tunnel tests and CFD/CAA simulations to show that slat tracks have a significant impact on the noise spectrum and level, up to 10 dB according to wind tunnel data from Yokokawa et al. [59]. Following these studies Chen et al. [60] simulated the flow field including slat tracks and found that the additional noise generation should not be ignored as the slat tracks cause a significant increase in the low-frequency broadband noise in the far-field spectrum, especially at a low angle of attack (AoA). The inclusion of slat tracks again resulted in an OSPL increase of about 10 dB at an AoA of 5° compared to the clean configuration. The slat track generates a spiral wake pair, which is identified as the main source of the additional noise. The slat track amplifies the interaction between the turbulent flow from the slat cove and the boundary layer on the main wing's upper side. This shifts the dominant source from the slat to the main wing, i.e., the change in the flow field due to the presence of the slat track significantly increases the main wing LE turbulent impingement noise. Van Bokhorst et al. [61] performed a parametric wind-tunnel study on several slat track designs and showed that small changes to the design, such as a tilted fairing and a flow cut-out, could lower the slat noise considerably across the frequency spectrum.

Fuselage-wing-slat junction noise has been the subject of few studies. Bai et al. [62] analysed the noise characteristics of the junction noise to reveal the noise generation mechanism. The study attributes the noise to horseshoe vortices (HSVs) impinging on the fuselage (which the author questions, subsection 4.3.2), and to slat side-edge noise. Previous studies, e.g. Molin et al. [63], assumed the noise generation to be similar to the flap side-edge noise generation even though the flow structures are dissimilar (as shown by multiple sources [64, 65, 66, 62]). The next section aims to give a generalised description of the main features of a fuselage-wing-slat junction and thereafter provides an overview of conclusions from studies exploring fuselage-wing-slat junction noise.

4.2. Description of the fuselage-wing-slat junction

This section briefly compares the geometry of the fuselage-wing-slat junction for in-flight and approach configuration. Thereafter, constraints to potential alterations will be discussed by describing the aerodynamic and structural functions of different components in the junction.

4.2.1. Geometric description of the fuselage-wing-slat junction

The deployment of the slat significantly modifies the junction region, as depicted in figure 4.7. This region is not just defined by the wing, slat, and fuselage, but also by the slat horn, slat stump, slat tracks, and the fairing that bridges the wing and the fuselage. The slat horn refers to the horn-like extension at the inboard edge of the slat. The slat stump, on the other hand, is the component that links the fuselage to the slat horn when the aircraft is in cruise configuration. Upon the deployment of the slats, the slat stump protrudes slightly from the main wing. These additions are designed to enhance the aerodynamic efficiency of the inboard wing during cruise. However, the junction between the fuselage and the wing is characterised by high-pressure gradients, gaps, and multiple exposed edges parallel and perpendicular to the flow, which

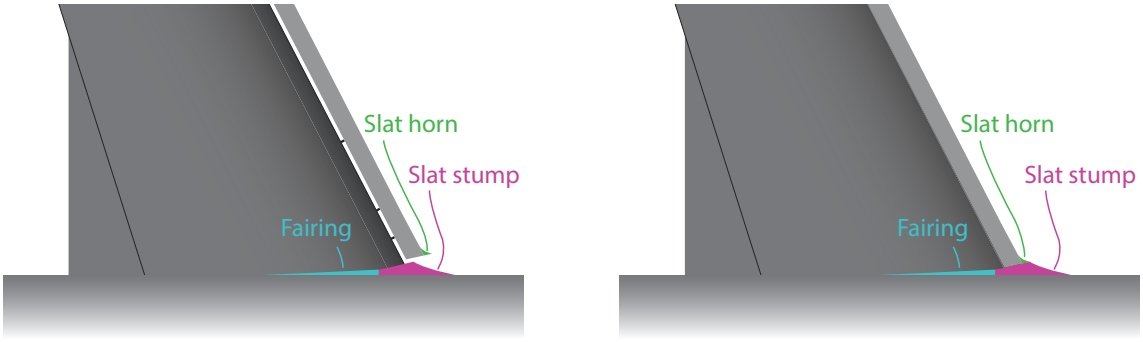

(a) Deployed slat **(b)** Retracted slat

Figure 4.7: Fuselage-wing junction definitions

lead to 3D flow phenomena, likely contributing to noise radiation.

4.2.2. Constraints subject to fuselage-wing-slat junction alterations

The aerodynamic and structural functions of the components in the fuselage-wing-slat junction dictate the breadth of possible modifications for noise reduction in the region. Table 4.1 provides an overview of simplified aerodynamic and structural design requirements for the slat horn, slat track, and slat stump. The **aerodynamic function** of the slat horn while in-flight is to create a smooth transition between the wing and fuselage. In approach configuration the slat horn helps to create a stronger vortex at the wing root to reduce the inclination for root stall at high AoA [65]. If the junction noise source is primarily influenced by the vortex formed by the slat horn, then a noise abatement solution should not remove the vortex altogether as it conflicts with its purpose. The slat track's function is to carry the slat deployment. The **structural criticality** of the slat horn is lower than for the slat track as the aerodynamic function of the slat track is to reliably carry the slat deployment, which is vital for successful landing. These structural requirements are imperative to the primary goal of the component, i.e. ancillary.

Table 4.1: Design requirements for components in the fuselage-wing-slat junction

	Design requirements	Slat horn	Slat track	Slat stump	Comment
Aerodynamic	Create a strong streamwise vortex to reduce the separation inclination of the flow along the wing root.	Primary	N/A	N/A	The goal of the slat horn is to create a strong vortex. Hence a noise abatement solution cannot be to reduce the vortex strength
	Carry the slat deployment	N/A	Primary	N/A	The slat track are only a support system on which the slats rest, actuators and rollers are used to guide the track to deploy and retract
	Merge the wing and fuselage in-flight	Primary	N/A	Primary	
Structural	Low weight	General	General	General	-
	High stiffness	General	Ancillary	General	-
	High strength and toughness to resist fracture under high stress and impact	General	Ancillary	General	-
	High reliability/long fatigue life	General	General	General	-
	High resistance against environmental wear	General	General	General	e.g. structural hydrogen embrittlement

4.3. Review of fuselage-wing-slat junction studies

This section reviews the literature on the aerodynamic structures present in the fuselage-wing-slat junction. Thereafter, the literature on the acoustic response from the fuselage-wing-slat junction is reviewed, including a tabulated comparison of the different research setups and conclusions.

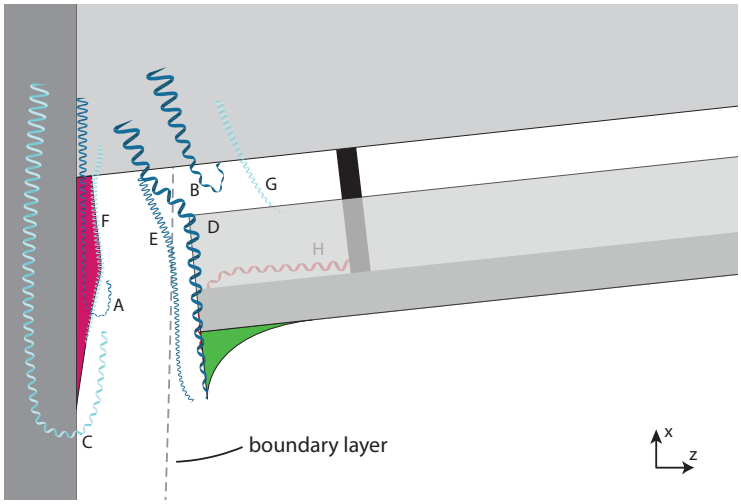

Figure 4.8: Schematic representation of the different vortices at the fuselage-wing-slat junction. Vortices C, F and G rotate in contra direction compared with A, B, D and E (depicted in light and dark blue respectively). The figure illustrates the difference between horseshoe vortices and other vortices. Additionally, the sizes of the depicted vortices are indicative of their strength. The slat's upper surface is shown partly transparent to visualise the corner flow and the slat track.

Table 4.2: Overview of turbulent flow-surface interactions.

ID	Surface	Flow phenomena	
S1	Fuselage	A	D
S2	Main wing SS	A (LE)	F (LE)
S3	Main wing PS	A (LE)	
S4	Slat chord SS	X (TE)	D (TE)
S5	Slat chord PS	H	Y (TE)
S6	Slat cusp SS	G (TE)	E (TE)
S7	Slat cusp PS	X (TE)	
S8	Slat track	H	E
S9	Slat side-edge	H	
S10	Slat stump	A	F

Table 4.3: Description of flow phenomena. A-H correspond the lettering used in figure 4.8

Letter	Flow phenomenon
A (B,C)	3D: horseshoe vortices
D	3D: slat chord side-edge streamwise vortex (includes slat horn)
E	3D: slat cusp side-edge streamwise vortex
F	3D: slat stump side-edge streamwise vortex
G	2D: recirculated turbulent flow in cove
H	3D: side-edge spanwise shear impingement from corner vortices
X	2D: turbulent boundary layer
Y	2D: slat cusp chordwise shear impingement

4.3.1. Aerodynamic description of the fuselage-wing-slat junction

Melber-Wilkending [65] describes the flow phenomena extensively, based on simulations on a generic high-lift aircraft. Three types of vortices exist near the junction: horseshoe vortices (HSVs), side-edge vortices, and slat-cove vortices; schematically summarised in figure 4.8. The region's surface (table 4.2) and vortex (table 4.3) interaction will contribute to the local noise radiation.

Horseshoe vortices form when boundary layer flow meets a body oriented perpendicular to the wall that causes the boundary layer, such as a wing to a fuselage. Two primary horseshoe vortices are formed: the slat stump HSV (A, in figure 4.8) and the wing LE HSV (B). The slat stump HSV runs along the fuselage and disappears quickly because it is weak. The wing LE HSV is stronger and more persistent. A secondary HSV (C), is induced by the slat side-edge vortex and the wing downwash. It runs parallel to the primary slat stump HSV and has a counter-rotating behaviour that makes it move downwards due to its own induced velocity.

Side-edge vortices form because of a loading differential: near the slat side-edge (D) and near the slat stump side-edge (F). The slat side-edge vortex propagates over the upper surface of the wing towards the TE and rotates in the same direction as the primary horseshoe vortices (due to the roll-up from pressure to

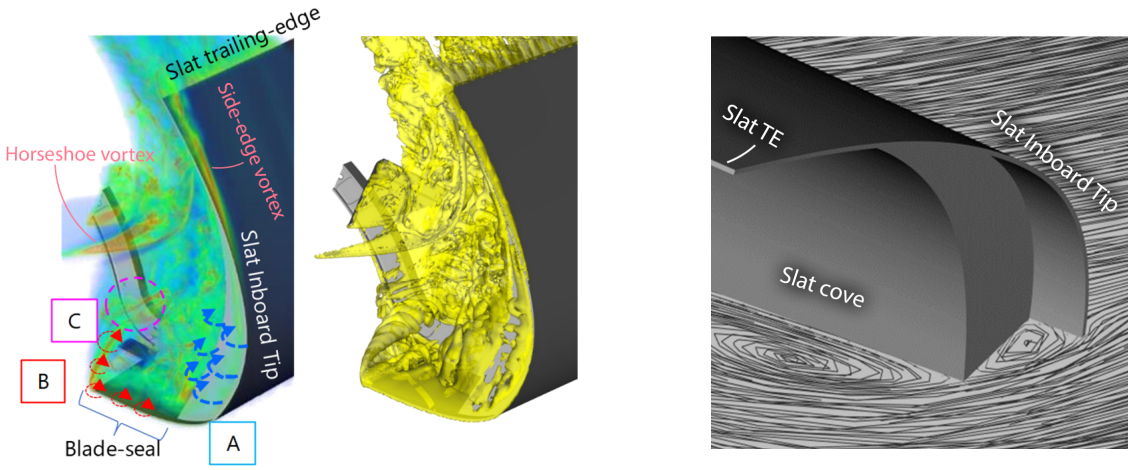

Figure 4.9: Vorticity magnitude (left) and iso-surface (right) visualisations **(a)** including the identified flow structures at the inboard slat tip (side-edge), adapted from [35]. 'A' indicates both the upper surface to side-edge vortex flow and the side-edge to cove vortex flow, more clearly shown in the streamline visualisation **(b)**, adapted from [35]. 'B' indicates the longitudinal vorticity along the blade-seal, the separation, and the outboard propagation. 'C' shows the area where the longitudinal vortex impinges on the inboard slat track. The horseshoe and side-edge vortex indicators were added by the author.

suction side). Its strength increases with the angle of attack and its location is higher above the wing at higher AoA because of the freestream flow direction. Interestingly, experimental research by Molin et al. [63] using a tuft suggests that the vortices roll up from the slat upper side towards the slat cove, opposite of the vortex roll-up from a flap side-edge. Molin et al. [63] made a noise and vortex prediction model for the slat and flap side-edges based on these observations. However, the author notes that these conclusions were drawn based on a single tuft. The reversed loading and hence vortices at the slat side-edge, if present at all, might be influenced by the usage of a low aspect ratio wing, and a thick wind tunnel boundary layer. The numerical results from Melber-Wilkending [65] indicate that the vortices roll up from the slat cove to the upper side. The orientation of the slat side-edge vortex is largely platform-dependent as its orientation depends on the direction of the loading of the slat, the spanwise velocity, and their interaction. The slat stump side-edge vortex forms on the outboard side of the slat stump and merges with the primary slat stump HSV. A secondary side-edge vortex (E), is induced by the gapflow and the slat side-edge and rotates in the same direction as the primary slat stump HSV.

The slat-cove vortices form due to flow recirculation from the slat cusp in the slat cove that gets convected towards the slat TE, and separate at the pressure side of the slat (G). Murayama et al. [35] describes some additional junction vortex structures, which are visualised in figure 4.9, through vorticity magnitude and iso-surface visualisations. Figure 4.9a identifies three additional coherent vortex structures that could affect the aerodynamic efficiency and the noise radiation of the fuselage-wing junction region. Two corner vortices (combined in H): the top surface to side-edge vortex and the side-edge to slat cove vortex (best visualised in figure 4.9b). Another vortex is on the blade-seal (or slat cusp) (combined with E in figure 4.8) which convects towards the inboard slat track. The flow moves in spanwise direction due to the pressure difference between the low-pressure slat cove and the high-pressure wing stagnation point. Murayama et al. [35] do not mention the horseshoe vortices or the tip side-edge vortex, but the author believes that they are visible in the figure 4.9 and has consequently added the labels to the figure.

4.3.2. Acoustic description of the fuselage-wing-slat junction

The noise intensity at the junction is a significant contributor to overall airframe noise. Davy and Remy [67] demonstrated through wind tunnel beamforming integrations on a 1:11 Airbus model ($Re \sim 1 \cdot 10^6 - 3 \cdot 10^6$) that the noise level at the junction was only 3 dB lower than the total noise level. The noise spectrum collapsed with Strouhal scaling up to 2 kHz, above which the spectrum shape remained constant and the amplitude varied with velocity to the 6th power. More recent junction noise scaling estimates from Bai et al. [62] on a 9.24% Dornier 728 half-model (Re $1.0 \cdot 10^6 - 9.0 \cdot 10^6$) reported varying velocity scaling values, ranging from 4.2 to 4.6, depending on the beamforming deconvolution algorithm used.

These measurements are closer in line with 5th-order power scaling from noise radiation near a scattering half-plane [30].

The influence of a fuselage-slat gap on the noise characteristics of the junction is significant. Research conducted by Ribeiro et al. [34] demonstrated that integrating the slat side-edge with the fuselage of the OTOMO2 model geometry resulted in a reduction of the Sound Pressure Level (SPL) across all frequencies by approximately 3 dB, as observed in both wind-tunnel and numerical experiments. However, the study did not provide quantification of the noise reduction in a closed-gap geometry with the presence of slat tracks, leaving the impact of side-edge-to-track flow interactions unexplored. Research by Lockard et al. [68] indicated that transitions from the slat side-edge to the wing (both stepped [69], and flexible [70]) designed by Turner et al. [71], in conjunction with a slat gap filler, effectively mitigated noise, even when slat tracks were included. Unfortunately, the study did not quantify the noise reduction that can be solely attributed to closing the fuselage-slat gap.

The noise at the fuselage-wing-slat junction is often attributed to the existence and impingement of vortical structures near the slat side-edge and near the fuselage. Molin et al. [63] suggested that a vortex from the slat side-edge impinging on the side-edge and near the main wing was the leading cause of junction noise. However, upon inspection, the high-intensity main wing pressure fluctuations are more likely related to turbulent structures from separated flow near the slat track, as researched by Van Bokhorst et al. [61]. Moreover, Molin et al. [63] predicts that the side-edge vortex moves from the upper slat surface to inside the slat cove, which is contrasted by newer studies from Melber-Wilkending [65], Ribeiro et al. [34], and Murayama et al. [35] who all predict a roll-up from the slat cove to upper slat surface. Bai et al. [62] corroborated the side-edge noise source from Molin et al. [63]. They showed an additional distributed fuselage noise source, caused by horseshoe vortices near the fuselage-wing junction. The existence of the fuselage noise source seems platform dependent, however, as Ribeiro et al. [34] does not report on this phenomenon. Additionally, the pressure fluctuation intensity (illustrated in figure 4.11) caused by the horseshoe vortices in the numerical study from Lockard et al. [72] do not match the location of the noise source shown by Bai et al. [62]. Instead, Lockard et al. [72] attributed the largest pressure fluctuation intensity in the junction to the presence of a ‘step’ slat stump. Lockard et al. [72] specifically notes that the inclusion of a ‘smooth’ slat stump could have reduced the unsteadiness at the fuselage-wing junction.

The influence of aero-structural design on the aeroacoustic characteristics of the junction has predominantly been examined concerning modifications of the slat features or assessing the impact of the angle of attack. Molin et al. [63] and Bai et al. [62] agree that the junction noise increases with angle of attack, emerging as the most significant high-frequency noise source at elevated angles of attack across all components [63]. At a more fundamental level, the noise mechanism is associated with the loading of the slat, which affects the pressure fluctuation intensities stemming from side-edge vortices. Ribeiro et al. [34] found that increasing the sweep angle by $\sim 5^\circ$ lowered the OSPL noise by ~ 1.5 dB. They attributed this phenomenon to less impingement from side-edge vortices inside the slat cove, creating a ‘quiet zone’. Murayama et al. [35] identified that alterations to the slat side-edge which weaken roll-up vortices from the slat cusp and minimise separation-induced turbulent structures at the slat side-edge, reduce the junction broadband noise by preventing impingement near the slat track and in the slat cove. This contrasts earlier work from

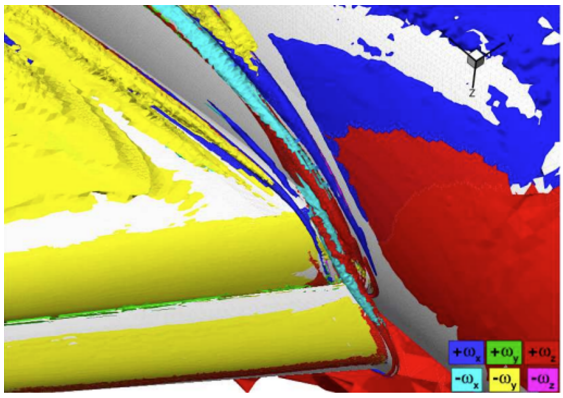

Figure 4.10: Visualisation of the fuselage-wing-slat junction vortical structures coloured by the vorticity orientation [65].

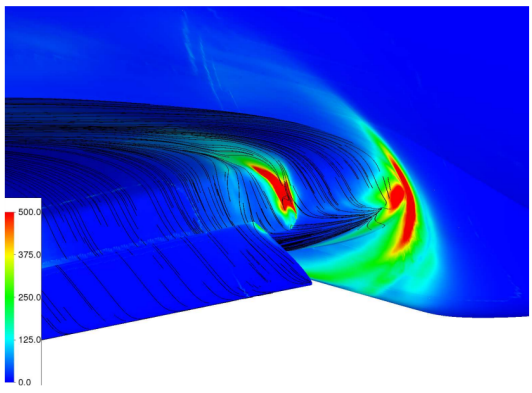

Figure 4.11: Pressure fluctuation intensity at the fuselage-wing-slat junction [72].

Molin et al. [63], which reported that geometrical details such as the slat horn shape did not meaningfully alter the noise radiation. It seems likely that proper side-edge noise abatement alterations are highly platform dependent, as Murayama et al. [35] reported that implementation of similar side-edge alterations on a wind tunnel validation model provided less prominent noise reduction results.

4.3.3. Fuselage-wing-slat junction research overview

The previous section described different studies discussing the fuselage-wing-slat junction noise. The model and flow conditions of these different studies are compared in table 4.4. The studies are difficult to reproduce as either the geometry data is not fully public, and/or the flow conditions are not fully specified. None of the studies describe the effect of the shape of the slat horn and the slat stump.

Table 4.4: Model specification and flow condition comparison from fuselage-wing-slat junction studies.

	Molin et al. (2003) [63]	Lockard et al. (2017) [72]	Lockard et al. (2022) [68]	Ribeiro et al. (2022) [34]	Bai et al. (2023) [62]	Murayama et al. (2023) [35]
Simulation	N/A	LBM (free-flow)	LBM (free-flow)	LBM (free-flow)	N/A	LBM (free-flow)
Wind tunnel	Open Jet	N/A	Open Jet	Open Jet	Closed Jet	Closed Jet
No. walls	2	N/A	1	1	4	4
Model geom.	Simplified junction section	10% scale HL-CRM half-aircraft	10% scale HL-CRM half-aircraft	Junction modified OTOMO2	9.24% scale Dornier 728 half-aircraft	10% scale 'Regional Jet' type half-aircraft
Airfoil (public data)	N/S (No)	NASA CRM-HL based (On request)	NASA CRM-HL based (On request)	JAXA JSM based (On request)	N/S (No)	N/S (No)
Slat horn	Present & absent configurations[a]	Absent	Absent	Absent	Absent	Absent
Slat stump	Step & smooth configurations[a]	Step	Step	Step	Step	Step
Slat flange	N/S	N/S	N/S	Present	Present	Present
Slat track (fidelity)	Present (low)	Present (N/S)	Present (N/S)	Present (high)	Present (high)	Present (high)
Sweep (deg)	Yes (N/S)	Yes (35)	Yes (35)	Yes (27-37)	Yes (23.5)	Yes (N/S)
Chord (m)	N/S	0.70	0.70	0.57	0.35	N/S
Half-span (m)	N/S	2.94	2.94	1.15	1.44	N/S
AR (half-span/ chord)	N/S ($\ll 1$)	4.2	4.2	2.0	4.1	N/S (~ 4)
Re. number	N/S	3.3e6	3.3e6	2.6e6	1.0e6 - 9.0e6	N/S
Mach number	N/S	0.20	0.12 - 0.20	0.20	0.15 - 0.25	N/S
Velocity (m/s)	60 - 80	N/S	N/S	N/S	N/S	N/S

[a] Article does not individually report on the different configurations.

The available measurements for each study are compared in table 4.5. The displayed parameters and measurements between studies were mostly similar, although none of the studies presented all six categories of measurements. Because of this, the probable cause of conflicting findings between studies is difficult to address.

Table 4.5: Available parameters and measurement locations from fuselage-wing-slat junction studies.

	Molin et al. (2003) [63]	Lockard et al. (2017) [72]	Lockard et al. (2022) [68]	Ribeiro et al. (2022) [34]	Bai et al. (2023) [62]	Murayama et al. (2023) [35]
Cross-section static pressure	-	Available on a section of the inboard slat.[a]	Available on a section of the inboard slat.[a]	Available on the midsection of the inboard slat.[a]	-	-
Wall pressure fluctuation spectra	Numerous locations on the slat and main wing.	-	Numerous locations on the slat and main wing.	-	-	-
Wall pressure fluctuation intensity (RMS)	-	Available on the main wing, slat stump and fuselage	Available on the main wing and slat stump.[b]	Available in the slat cove and on the slat side-edge	-	Available in the slat cove and slat side-edge for certain frequencies
Sound power spectra	Spectra available with and without fuselage-slat gap	-	-	Spectra from modified geometries w.r.t. baseline available	Standard geometry far-field spectrum above 5 kHz model scale.	Spectra from modified geometries w.r.t. baseline available
Beamforming	-	Num. data.	Exp. & num. data.[c]	-	Exp. data.	Exp. data.
Vortex visualisation	Tuft near the slat side-edge[d]	-	-	'0'-total-pressure-coefficient-isosurfaces at the slat cove and slat side-edge	-	Vorticity magnitude and isosurface at the slat cove, and slat side-edge
Complimentary data from a WT	-	N/A	Cross-section static pressure, wall pressure spectra, and beamforming.	Cross-section static pressure, and far-field noise spectrum	-	Beamforming, and far-field noise spectrum from a similar geometry

[a] The static pressure results show a large pressure differential between the pressure and suction side.
[b] The Integrated noise spectrum shows a large slat discrepancy between experiments and simulation on the slat.
[c] Discrepancy in the noise levels between experimental and numerical results. However, the location for mid and high-frequency shows extensive inboard slat noise. Nothing on the fuselage or stump.
[d] Shows a possible roll-up from suction to pressure side, instead of pressure to suction side.

4.4. Conclusions from the literature review

Studies conducted during aircraft flyovers reveal that approximately 40% of the total noise produced by the airframe of Airbus aircraft originates from the slats. Furthermore, the fuselage-wing-slat junction is a consistent source of high-intensity noise across the entire frequency range. Studies on fuselage-wing-slat junction noise radiation indicate that eliminating the slat gap, and hence many of the 3D flow structures, can significantly lower the overall junction noise. However, these studies have all been performed on different, and hard to reproduce models. The literature showed it was necessary for the numerical model and the experimental validation model to closely correspond to arrive at comparable conclusions about noise reduction. This suggests a strong correlation between the noise radiation and the aero-structure's design. The junction noise increases with higher angles of attack (more fundamentally the slat loading), and a lower sweep angle. Some studies claim that the shape of the side-edge is not of large influence, whereas other studies show clear noise reduction by changing the shape of the side-edge and/or slat horn. It is evident that there is a gap in understanding and agreement on how the design of the aero-structure influences the aeroacoustic footprint.

II

Research set-up, verification & validation, and results

This part discusses the designed research set-up and geometrical models in chapter 5, after which the numerical domain is described in chapter 6. In chapter 7, the numerical research set-up is verified for grid independence, and the model's flow phenomena and noise radiation are contextualised by comparing the model to literature. Chapter 8 presents the results of the aeroacoustic analysis of a fuselage-wing-slat junction.

5

Geometrical set-up

This chapter describes the fuselage-wing-slat junction research set-up. Section 5.1 describes the model's cross-section. In section 5.2, the designs of the 3D surface elements relevant to the final model geometry are outlined, and in section 5.3 the model is characterised to facilitate literature comparison.

5.1. Cross-section: two-element modified 30P30N

One of the challenges in studying the flow behaviour and acoustic radiation of a fuselage-wind-slat junction region is the absence of a common model geometry. Consequently, in this study, a model was developed based on the 30P30N airfoil cross-section, an open-source geometry commonly investigated in slat noise studies. Additionally, the geometry coordinates are readily available. The original 30P30N geometry has three elements: a slat, a main element, and a flap, with the dimensions given in figure 5.1 and table 5.1.

The research set-up is designed for open-jet wind tunnel testing. Terracol et al. [74] explain that experimental studies of slat noise are challenging due to the trade-offs between aerodynamic and acoustic performance of different wind tunnel types. Open-jet anechoic wind tunnels are often used in aeroacoustics, and Merino-Martínez et al. [75] summarises that achieving reliable absolute sound pressure levels is only possible in an open-jet facility, which eases comparison of the model's noise spectrum to full-scale fuselage-wing-slat junction flyover spectra. Open-jet facilities have drawbacks for testing a loaded three-element airfoil. Terracol et al. [74] explain that high loading deflects the streamlines in the test section significantly. This can result in irregular flow speeds for closed-loop wind tunnels. Additionally, the deflected flow can impinge on the collector, which introduces spurious noise sources in the domain.

The model is specifically designed for testing and validation in the TU Delft A-tunnel, although the wind tunnel validation itself is not part of the thesis. The A-tunnel is an anechoic open-jet tunnel which allows for interchangeable nozzles mounted to the exit of the nozzle contraction [75]. The set-up is designed for the largest rectangular nozzle, the 50×50 cm nozzle, to simplify the manufacturing of small parts like the

Table 5.1: Primary dimensions of the 30P30N

Slat chord	c_s	$0.15c$
Flap chord	c_f	$0.3c$
Slat deflection angle	δ_s	$30°$
Flap deflection angle	δ_f	$30°$

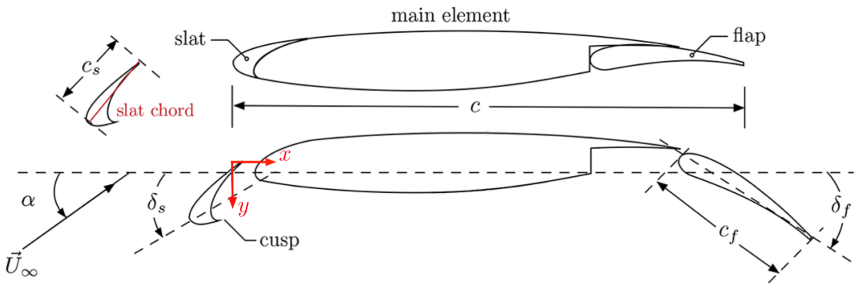

Figure 5.1: Description of the 30P30N airfoil adapted from Zhang et al. [73].

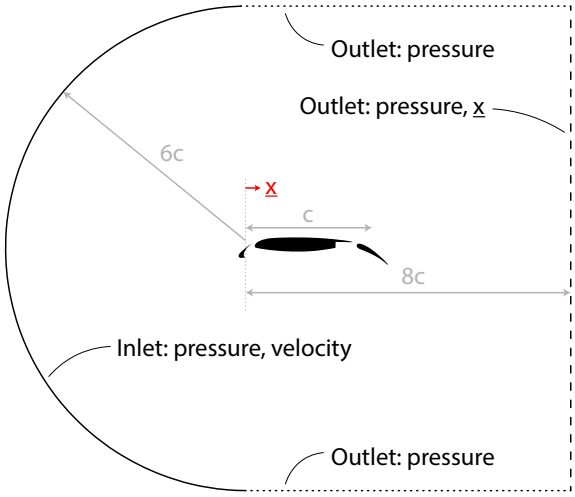

Figure 5.2: Schematic representation of the RANS domain and boundary conditions, not to scale.

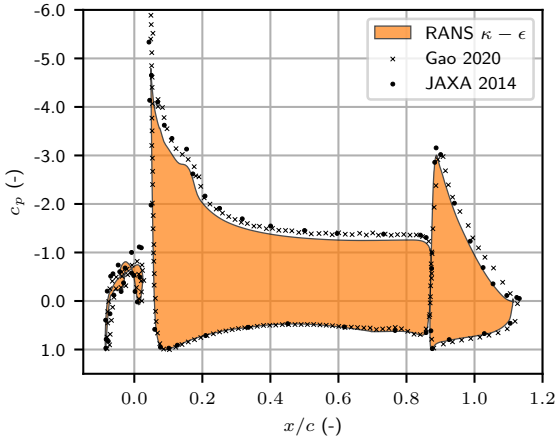

Figure 5.3: Pressure coefficient distribution of RANS $\kappa-\epsilon$ compared to numerical data (Gao) at $\alpha = 4.0°$ [76] and experimental data (JAXA) at $\alpha = 3.5°$ [77].

slat, and incorporates sideplates to minimise jet expansion effects. The maximum nozzle exit velocity of the 50×50 cm nozzle is 38.8 m/s.

A three-element 30P30N cross-section at an angle of attack of $\alpha = 4°$ (approach condition) has a highly loaded main element and flap. This study uses a de-lifted two-element 30P30N modification. The modification strives to keep the pressure gradient on the slat and near the leading edge similar to the original three-element cross-section, following the influence of loading on junction flow structures derived from literature. A method described by Terracol et al. [74] modifies the airfoil for minimal streamline deflections and similar slat cove recirculation based on two parameters: the trailing edge y-location of the cross-section $y|_{x/c=1}$, and the angle of attack α, using RANS simulations. This research uses a similar approach, but instead of streamline-similarity, the loading on the slat and near the leading edge is used for converting the three-element 30P30N $4.0°$ AoA cross-section to a de-lifted two-element 30P30N cross-section.

The description of the RANS domain and boundary conditions is shown in figure 5.2. A free-stream velocity of $U_\infty = 30$ m/s and a chord length of $c = 0.5$ m (following section 5.2) were used. For the three-element verification, a relatively coarse and small domain was created to expedite the simulation time. The simulation uses a $\kappa-\epsilon$ solver and is compared to numerical data from Gao et al. [76] and experimental data from JAXA, illustrated by Murayama et al. [77], shown in figure 5.3. The results are based on a mesh with an average suction and pressure side y^+ of 20 and 10, respectively. The smallest cell size on the

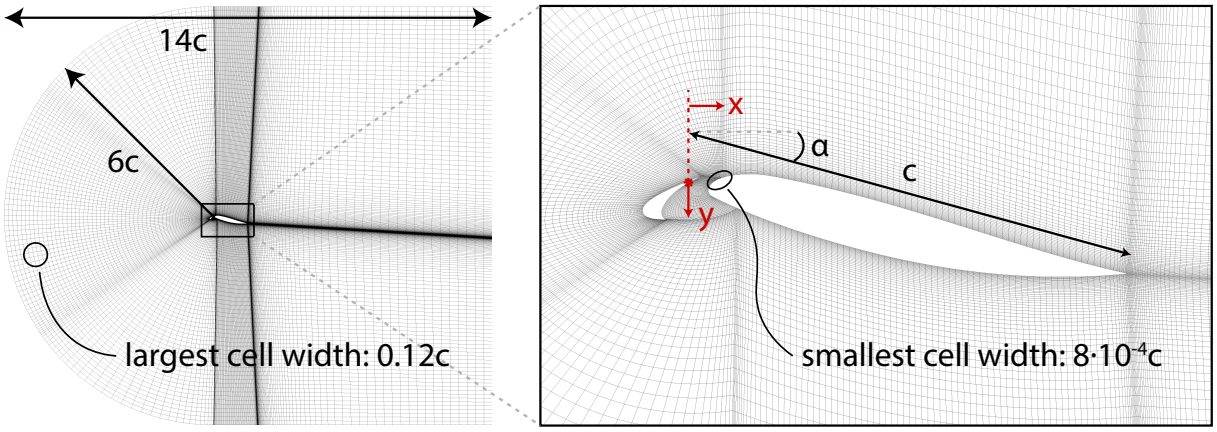

Figure 5.4: Visualisation of the RANS mesh for the two-element $\alpha = 16°$, $y/c\,|_{x/c=1} = 0.06$ geometry.

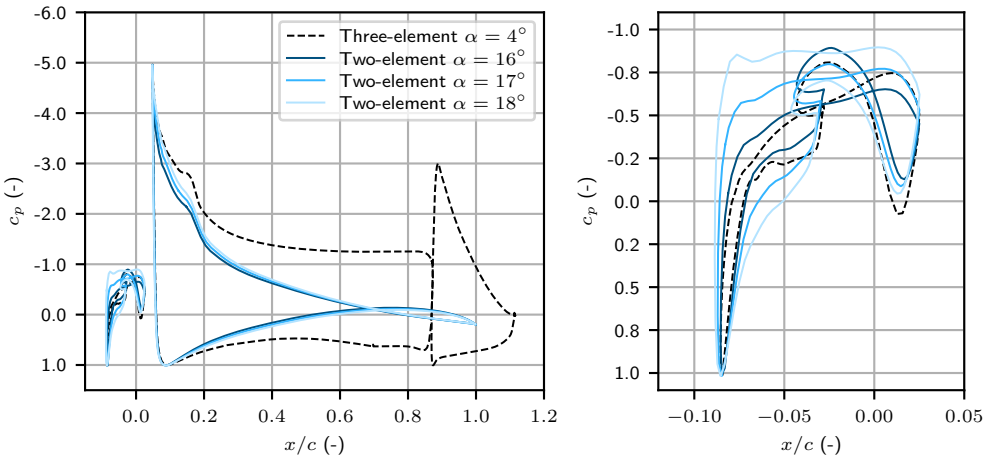

Figure 5.5: Pressure coefficient distribution by angles of attack α for two-element geometries at $y/c\,|_{x/c=1} = 0.06$ from RANS.

suction side was $6 \cdot 10^{-5}$ m ($1.2 \cdot 10^{-4}c$), and on the pressure side $2.5 \cdot 10^{-4}$ m, or ($5.0 \cdot 10^{-4}c$). The size of the cells increases to 0.12 m ($0.24c$), after which they stay constant in size.

Figure 5.3 shows that the slat loading largely matches the simulations from Gao et al. [76], and similarly deviates from experimental tests on the slat suction side. The pressure side of all three elements matches both the numerical and experimental data. The main element suction side loading extent is slightly underpredicted. This is likely a result of the coarse mesh failing to completely capture the acceleration near the suction peak as the y^+ near the suction peak jumps to 60. However, for the two-element modification exercise, the absolute magnitude of the loading is less relevant than capturing the same flow physics as seen in literature. The slope trend of the RANS simulation is consistent with both the numerical simulations from Gao et al. [76], and experimental tests from Murayama et al. [77], which indicates that the simulation captures the expected flow phenomena at the correct locations.

The domain for the two-element model is visualised in figure 5.4 and follows the same flow physics based criteria. The mesh blocking is kept simple for quick adaptation when α or $y|_{x/c=1}$ are iterated. The two-element domain has an average y^+ of 40, with a smallest cell size of $4 \cdot 10^{-4}$ m ($8 \cdot 10^{-4}c$), which exponentially grows to 0.06 m ($0.12c$). For the two-element model, the leading edge at the suction side was kept unchanged up to $x/c = 0.47$, and on the pressure side up to $x/c = 0.40$ after which a spline interpolation smoothly connects the leading edge with the trailing edge location. Terracol et al. [74] used an FNG-type cross-section, which is similar to the 30P30N. Hence, their optimised parameters of $\alpha = 18°$ and $y/c\,|_{x/c=1} = 0.06$ were chosen as starting points of the modification process. The two-element geometry was varied in terms of operating angle of attack α and trailing edge y-location $y/c\,|_{x/c=1}$ to achieve similar slat streamwise loading, main element suction peak extent and, main element leading edge loading between the two- and three-element geometries. The pressure distribution to operating angle of attack α comparison results for the $y/c\,|_{x/c=1} = 0.06$ case are shown in figure 5.5. A de-lifted geometry

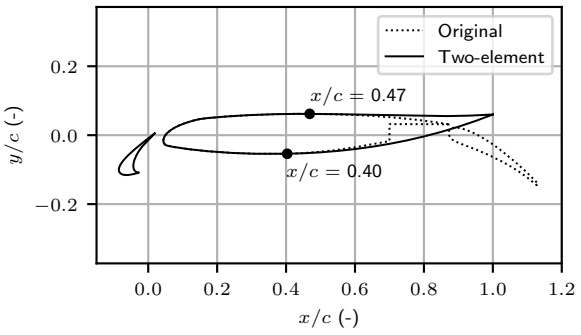

Figure 5.6: Two element geometry vs the original three element geometry

with a trailing edge position of $y/c\,|_{x/c=1} = 0.06$ and an operating angle of attack $\alpha = 16°$ was created. A comparison of the original three-element cross-section is provided in figure 5.6.

5.2. Model: swept two-element 30P30N with junction surfaces

This section describes the fuselage-wing-slat junction modified 30P30N model. Firstly, the planform design is described, thereafter the slat stump, horn, and flange design are shown. Lastly, the angle of attack correction for an open-jet experiment is described.

5.2.1. Planform design of the model

The wing planform design is engineered to mimic an aircraft's planform design objectives. A primary objective is to achieve an elliptical spanwise pressure distribution, which minimises drag caused by tip vortices. This is achieved through wing tapering, twist, and a Yehudi. Ideally, the streamwise pressure distribution across spanwise sections should be similar when normalised by the local chord length. In addition to these aerodynamic considerations, the model must be manufacturable. Therefore, elements such as the slat cannot be excessively small, and the edges must have a certain thickness. The minimum edge thickness used was 0.15 mm. Edges thinner than this pose a safety risk during a wind tunnel validation campaign. A minimum slat chord length of $\sim c_s = 6$ cm should be maintained to preserve the slat shape which does not remove much material at the 'thick' slat trailing edge. These considerations ensure that the model is both representative of an actual aircraft and feasible to produce.

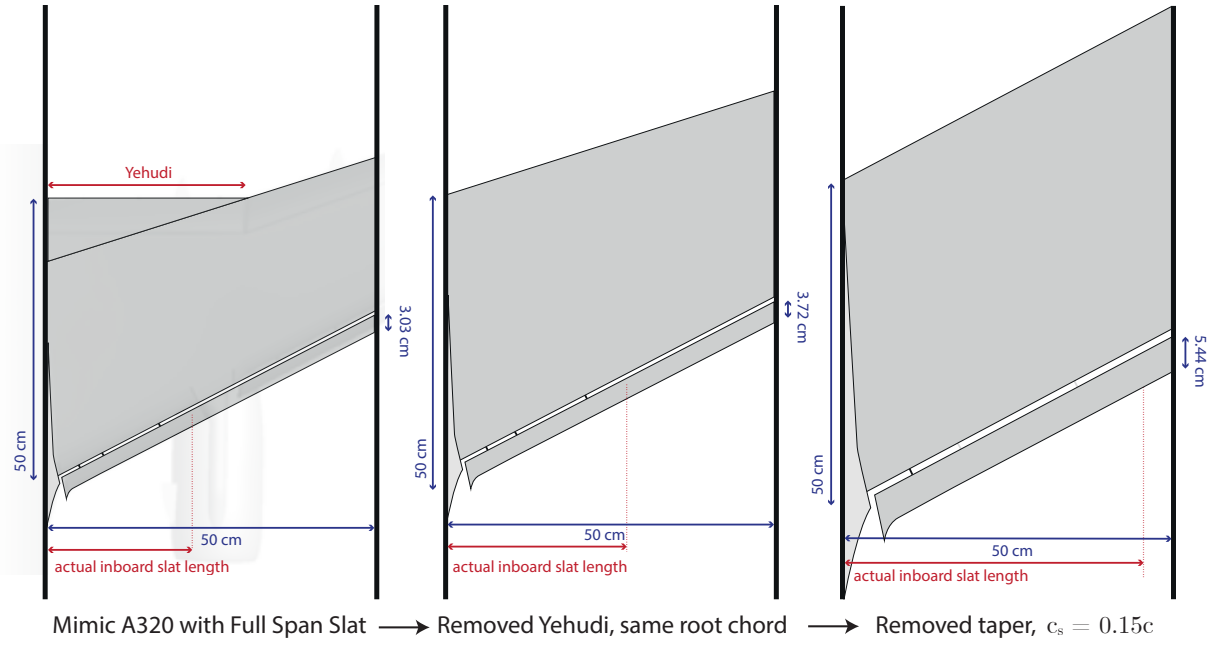

Figure 5.7: Main fuselage-wing-slat junction research model design iterations

The design process, as depicted in figure 5.7, began with a simplified top-down view of the Airbus A320 half-planform, fitted between two sideplates. The maximum span was set to 50 cm to align with the jet of the 50×50 cm nozzle. The aspect ratio, defined as $AR = c_{\text{root}}/d_{\text{plates}}$, was set to a minimum of $AR = 1$, yielding a root chord of 50 cm. Subsequently, the Yehudi was removed from the model geometry, given its structural objectives are not pertinent to the research model, which is focused on aeroacoustic similarity. While the Yehudi serves an aerodynamic purpose in reducing the spanwise "mitteneffekt" - a decrease in lift at the centre of two swept wings due to interference between their pressure profiles - this effect is not present in a half-wing model. The modified 30P30N was designed to ensure that the slat and leading edge loading closely resembled that of the three-element model. To prevent alteration of the slat loading, the ratio between the wing and slat length was maintained at $c_s = 0.15c$, leading to the removal of the taper. The research model features two sideplates which eliminate the tip vortices. Hence, tapering to reduce downwash is unnecessary. The removal of the taper also negates the need for differential spanwise twist

to achieve a similar streamwise pressure distribution across spanwise sections when normalised by the local chord length. Finally, to concentrate solely on the effect of the fuselage-wing-slat junction, the two outboard slat tracks were removed.

The final design is a significantly simplified planform that still largely adheres to aircraft aerodynamic loading principles. The planform has a slat length of approximately 5.4 cm from a top view (a slat chord length of $c_s = 0.15c = 7.5$ cm). This design strikes a balance between the need for manufacturing simplicity and the design objectives of a wing planform.

5.2.2. Model variations & junction surfaces

Three model variants were developed to assess the impact of specific geometrical features on the flow structures and noise radiation near the junction. The 'No Gap' (NG) geometry, which features a full-span slat and no fuselage-slat gap, serves as a control geometry. Two additional geometries incorporating varying junction surfaces were also designed. The first, a 'No Horn & Step Stump' (NH) geometry, features a simple slat side-edge and a step-transition (step slat stump) between the sideplate and wing. The second, a 'Horn & Smooth Stump' (H) geometry, features a slat horn on the slat side-edge and a smooth slat stump.

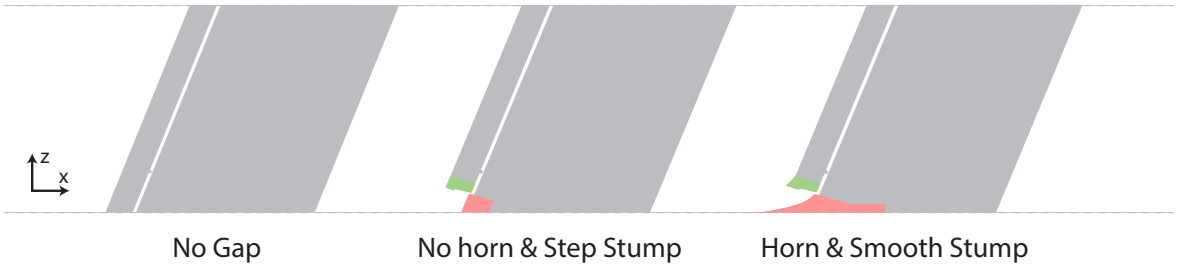

Figure 5.8: Schematic representation of the three research model variants

All variants, visualised in figure 5.8, are part of a sideplate+model setup. The sideplate length was selected to ensure that the relative boundary layer thickness mirrors the relative thickness of the fuselage boundary layer of an Airbus A320 compared to the fuselage-slat distance. This ratio is maintained to achieve similar slat-side-edge and junction horseshoe vortex interaction effects.

Each geometry features a slat flange that overlaps with the stump when retracted, ensuring that the stump and slat side-edges do not come into contact. The slat track is designed as a rectangle extruded with a spline, positioned and oriented at the same relative distance to the sideplate as the inboard-track-fuselage distance of an Airbus A320. The spline was designed to mimic the shape of a slat track on the Airbus A320, but high-fidelity geometrical details were omitted for this study.

The 'Horn & Smooth Stump' geometry was designed to approximate the junction surfaces of an Airbus

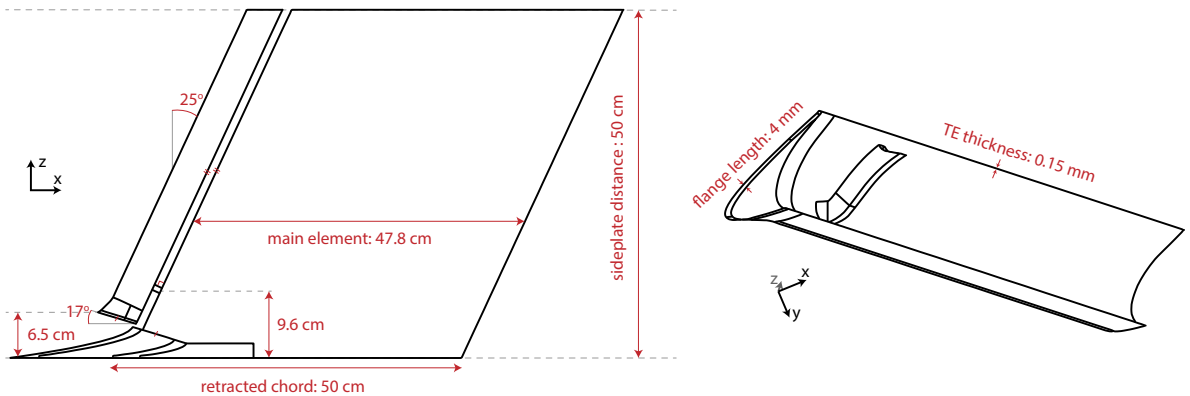

Figure 5.9: Schematic representation of the finalised design including relevant dimensions of the 'Horn & Smooth Stump' geometry.

A320. Literature indicated that the slat horn and slat stump should be included. The slat horn was shaped such that when the slat is retracted, the wing morphs with the fuselage. Furthermore, the junction surfaces are based on visual similarity to their implementation on the Airbus A320 due to the unavailability of their exact design or underlying design principles. The final schematics are provided in figure 5.9.

5.2.3. Open-jet angle of attack correction

The research model is designed for an open-jet wind tunnel set-up. The open-jet simulation angle of attack must be tuned such that the model $c_p(x)$ matches the steady-state free-flow $c_p(x)$ at the operating angle of attack. The angle of attack correction aims to obtain a minimal Root Mean Square Error (RMSE) between the $c_p(x)$ curves of the midsection ($z = 0.5b$) of the 'H' model variant using coarse grid simulations in PowerFlow, and the 2D two-element free-flow RANS simulation, eq. (5.1). The 3D model is swept by ϕ which is taken into account via eq. (5.2). The suitability of using a coarse grid for $c_p(x)$ comparisons is discussed in the grid convergence study in subsection 7.1.4.

$$RMSE = \sqrt{\frac{1}{n}\sum_{i=1}^{n}(c^i_{p,\,oj} - c^i_{p,\,RANS})^2} \tag{5.1}$$

$$c_p = \frac{p - p_\infty}{\frac{1}{2}\rho_\infty(\cos(\phi)\cdot U_\infty)^2} \tag{5.2}$$

Due to jet expansion, blockage, and jet deflection, the angle of attack needs to be increased to obtain a similar loading. Terracol et al. [74] performed a correction on a similar set-up in which a $18°$ two-element model was corrected to a geometrical angle of $25°$. Therefore, as a starting value for the angle of attack correction, a geometrical angle of $25/18 \cdot 16 = 22.2°$ was chosen. Figure 5.10 shows that an operating angle of attack of $26.2°$ best mimicked the free-flow RANS simulation. The RMSE is determined separately for the slat and airfoil pressure and suction side and summed for the total RMSE. The absolute pressure coefficient error based on chord position, $|c^i_{p,\,oj} - c^i_{p,\,RANS}|$, per element are further shown in appendix D.

The angle of attack corrected 3D PowerFLOW loading is shown in figure 5.11 for multiple grid refinements (described in section 6.2), and compared to the two-element RANS results at $16°$ and the slat loading from Gao et al. [76]. The distributions show similar $c_p - x$ loading trends on both the slat and the main element, indicating that the simulations capture similar flow phenomena, such as the loading reversal locations on the slat, and the main element suction side pressure rise at $x = 0.15$ m.

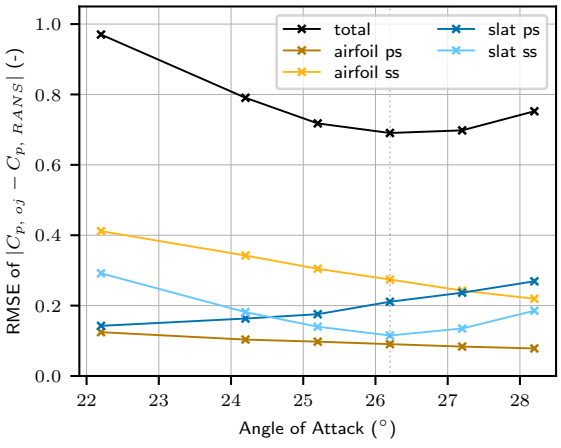

Figure 5.10: Operation angle of attack determination based on the root mean square error (RMSE) compared to the $16°$ RANS case.

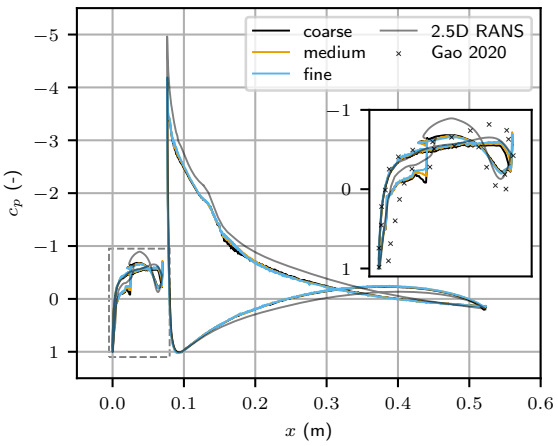

Figure 5.11: Pressure coefficient distribution of the RANS simulation and the 3D PowerFLOW mesh refinements.

5.3. Characterisation of the model

This section quantifies the loading and flow features of the research set-up, such that the model can be compared to literature. Similar $c_p(x)$-distribution across spanwise sections when normalised by the

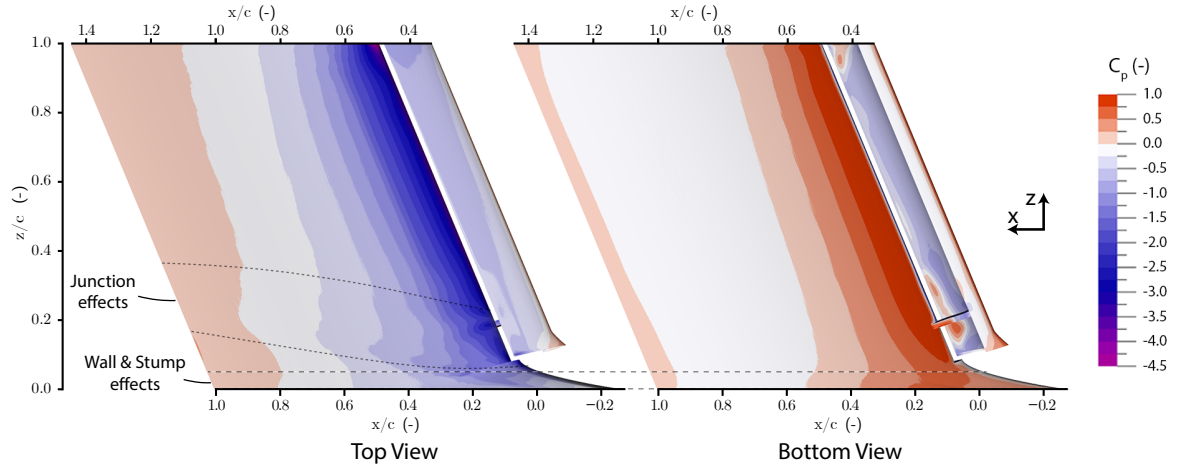

Figure 5.12: Surface static pressure c_p of the 'Horn & Smooth Stump' geometry

local chord length, as described in subsection 5.2.1, is equivalent to the isobars on the research model remaining parallel to the sweep. Figure 5.12 shows that the research set-up was largely successful in keeping parallel isobars, especially at the leading edge. Anticipated set-up effects are visible in the isobar contours, such as the deviation from sweep-parallel isobars behind the junction and near the walls and stumps.

The desired boundary layer thickness was calculated using eq. (5.3), as per subsection 5.2.2.

$$\delta_{\text{set-up}} = \frac{d_{\text{sideplate-slat, set-up}}}{d_{\text{fuselage-slat, A320}}} \cdot \delta_{\text{A320}} \tag{5.3}$$

where $d_{\text{sideplate-slat, set-up}}$ was set to 6.5 cm and $d_{\text{fuselage-slat, A320}}$ estimated at 20 cm resulting in $\delta_{\text{set-up}} \approx 5$ cm with the boundary layer thickness from the Airbus A320 in the junction δ_{A320} being estimated using flat plate theory approximations, eq. (5.4), as provided by White [78, p. 434].

$$\delta \approx x \frac{0.16}{Re_x^{1/7}} \tag{5.4}$$

where x is the streamwise location on the flat plate. This results in an approximate fuselage-boundary layer thickness near the junction of

$$\delta_{\text{A320}} = \frac{0.16 x_{\text{tip-junction}}}{Re_{x_{\text{tip-junction}}}^{1/7}} \approx 16 \text{ cm}$$

with $x_{\text{tip-junction}} \approx 12.7$ m, $Re_{x_{\text{tip-junction}}} = x_{\text{tip-junction}} \cdot U_{\text{approach}}/\nu \approx 58 \cdot 10^6$ with $U_{\text{approach}} \approx 67$ m/s and the kinematic viscosity $\nu \approx 1.46 \cdot 10^{-5}$ m^2/s. To achieve a boundary layer thickness of approximately 5 cm, the design incorporates a no-slip wall nozzle with a trip positioned 2.7 m upstream of the junction. The position of the trip is determined using eq. (5.4), with a flow velocity U of 30 m/s, suitable for the 50×50 cm A-tunnel nozzle. The method proposed by Spalart and Watmuff [79] is utilised to determine the achieved boundary layer thickness of the simulation. This method estimates the δ_{99} boundary layer thickness - 99% of the end velocity U_e - calculated by the integrated vorticity along the wall-normal direction, $U_e = \int_0^\infty \omega_y dz$. This results in a boundary layer thickness of $\delta_{99} \approx 6.8$ cm for the grid refinement applied in the analysis in chapter 8. The possible impact of the boundary layer thickness overshoot is discussed in chapter 10.

The two-element 30P30N was de-lifted to maintain similar slat loading and leading edge loading, with an angle of attack correction performed on the 'H' geometry. Figure 5.13 displays the pressure coefficient distributions of the three variants in the midsection $z = 0.5b$. The 'NH' loading is virtually identical to the 'H' loading. The 'NG' geometry matches 2D RANS suction extent in the slat cove more closely than the variants with a sideplate-slat gap. This indicates that the flow in the slat cove is altered by the introduction

of a gap. This flow alteration is extensively analysed in chapter 8. The effect on the loading on the main element remains negligible.

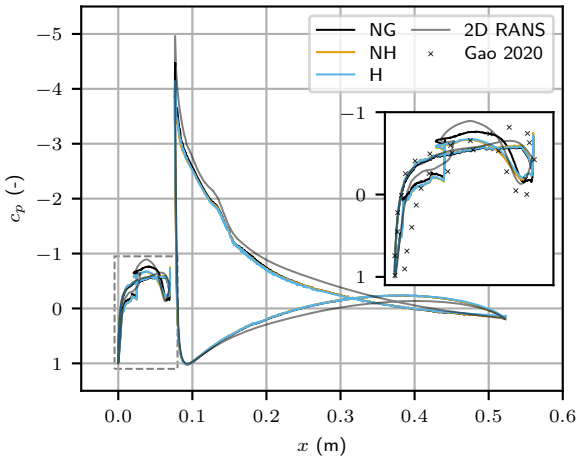

Figure 5.13: Pressure coefficient distributions of the three model variants at $26.2°$, compared to the results from 2D RANS at $16°$, and slat numerical results from Gao et al. [76] at $4°$.

6

Numerical set-up

This chapter discusses the development of the numerical simulation. Firstly, the boundary conditions are described in section 6.1. Thereafter, the mesh is described in section 6.2 and the anechoic sponge zone definition is explained in section 6.3. The main measurement criteria are shortly discussed in section 6.4.

6.1. Domain & boundary conditions

A cubic numerical domain of $80c \times 80c \times 80c$ was created to ensure minimal interference from the jet wake with the domain boundaries and allow for proper acoustic damping in the domain to minimise reflections. As depicted in figure 6.1 all six outside boundaries are set to a static pressure outlet. Additionally, a total pressure inlet boundary condition was placed inside the slip, i.e. frictionless, nozzle. The total pressure equates to $p_t = p_s + q$, where the static pressure is defined as $p_s = 101325$ Pa, the static air pressure at sea level, and the dynamic pressure is defined as $q = \frac{1}{2}\rho_\infty U_\infty^2$, with the density defined according to the perfect gas law $\rho_\infty = \frac{p_s}{RT} \approx 1.225$ kg/m^3 as the gas constant for air R is roughly 287.05 J/kg K, and the temperature at sea level T was set to 288.15 K. Lastly, the inflow velocity at the nozzle U_∞ was set to 30 m/s, which is near the upper bound of the maximum flow velocity of the A-tunnel's 50×50 cm nozzle. The velocity in the nozzle was hence induced by the pressure differential between the in- and outlet conditions equal to the dynamic pressure at 30 m/s. This option was preferred over a purely velocity-based inlet boundary condition as it more closely mimics the behaviour of a wind tunnel, and a constant total pressure inlet condition is similar to a constant rate of energy over the boundary. Hence, the same amount of energy is supplied to the domain at every timestep of the simulation. An overview of the fluid and flow conditions is provided in table 6.1.

The other boundaries in the domain are either slip, i.e. frictionless walls, or no-slip walls. All walls situated within the nozzle jet, except for the slip nozzle (figure 6.1), are no-slip walls. All walls situated outside the nozzle jet, e.g. the outsides of the sideplates, are slip walls. The no-slip nozzle starts 2.7 m upstream of the sideplate-slat junction. At the start of the no-slip nozzle, the flow is tripped to ensure a turbulent boundary layer is created.

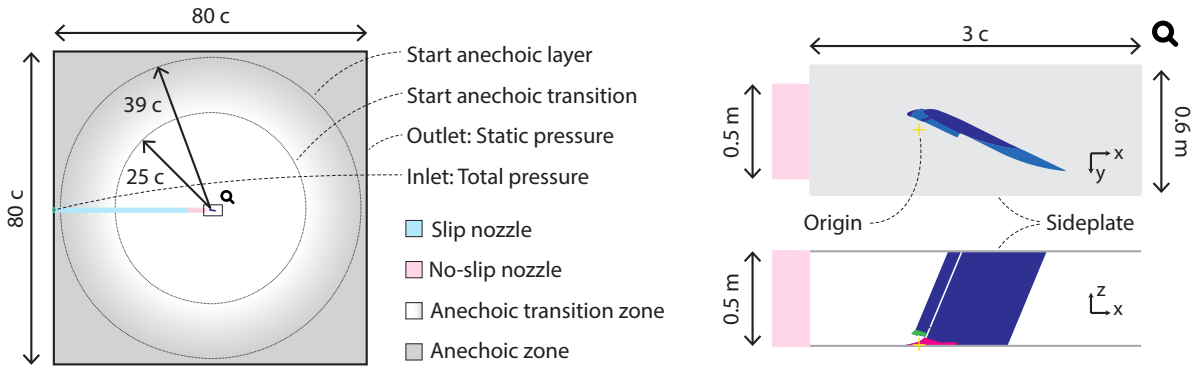

Figure 6.1: Schematics of the numerical fuselage-wing-slat junction research set-up

The simulation was set up for a sampling period of approximately 20 chord flow passings, i.e.

$$t_{\text{sampling}} = (N_{\text{passings}} \cdot c)/U_\infty \approx 0.333 \text{ s}.$$

Before sampling the flow is initialised with a transient time. The transient time depends on whether the simulation is seeded from a previous run or not, given by

$$t_{\text{transient}} = \begin{cases} (N_{\text{paths seeded}} \cdot c)/U_\infty \approx 0.066 \text{ s}, & \text{if seeded} \\ (N_{\text{domain lengths}} \cdot 2r_{\text{domain}})/U_\infty \approx 1.333 \text{ s}, & \text{otherwise} \end{cases}$$

where $N_{\text{paths seeded}} = 4$, $N_{\text{domain lengths}} = 1$, and $r_{\text{domain}} = 20$ m. Note that non-seeded simulations are only run on very coarse meshes, and were designed to properly initialise the flow inside the nozzle, and the jet flow from the nozzle exit to all domain boundaries.

Table 6.1: Fluid and flow conditions of the simulation

Density	ρ	(kg m^{-3})	1.225
Ambient static pressure	p_s	(Pa)	101325
Speed of sound	c_{sos}	(m s^{-1})	340.3
Dynamic viscosity	μ	(kg m^{-1} s^{-1})	$1.79 \cdot 10^{-5}$
Temperature	T	(K)	288.15
Free-stream velocity	U_∞	(m s^{-1})	30
Chord Reynolds number	Re_c	(-)	$1.03 \cdot 10^6$

6.2. Grid discretisation

The discretisation of the domain is described in figure 6.2. The domain is discretised using a Cartesian mesh, also known as a lattice. A unit of the lattice is defined as a voxel in PowerFLOW's solver. The lattice is comprised of Variable Resolution (VR) zones where higher numbers indicate smaller voxel widths, i.e. VR0 $\geq$ VR1 $\geq$ VR2 $\geq$ ... The widths of voxels vary by a factor of 2 in adjacent resolution regions. Surface elements, referred to as surfels, are used to discretise surfaces of solid bodies at the positions where they intersect with a voxel. All voxel sizes of all VR zones are scaled by the size of the finest voxel. The simulation domain, discretised by VR0 voxels, consists of four blocks, with VR1 to VR4 sized voxels, respectively, centred around the research set-up's leading edge and elongated towards the wake of the set-up. Surrounding the inside of the no-slip nozzle and the sideplates, two offset refinement zones, with VR5 and VR6-sized voxels, are used to capture the boundary layer flow in the nozzle. Near the research model, similar offsets are used, including an additional offset refinement with VR7-sized voxels. This refinement layer is thicker at the suction side than the pressure side to capture the flow fluctuations moving over the model stemming from the slot and slat trailing edge. Lastly, near the slat, the leading edge of the main element, and in the slat cove, a final refinement (VR8) is introduced to capture the small-scale turbulent structures within the slat cove and to reduce the y^+ near the suction peak of the main element. All offset refinements (VR5 - VR8) are 12 voxels wide in the 'medium' simulation, except for the main element suction side's VR7 zone, which is 24 medium voxels wide to simulate the trailing edge slat turbulent structures. Three meshes, a coarse, medium, and fine mesh, separated by a refinement factor of $r = 1.5$ were analysed. The smallest scale voxel (VR8) has a resolution of $4.88 \cdot 10^{-4}$ m ($c/1024$), $3.26 \cdot 10^{-4}$ m ($c/1536$), and $2.17 \cdot 10^{-4}$ m ($c/2304$) for the coarse, medium, and fine mesh, respectively.

The mesh is designed to simulate the highly energetic and unstable turbulent flow structures within the slat cove's mixing layer. Terracol et al. [74] propose that the vorticity thickness, δ_ω, of a slat shear layer can be approximated as a mixing layer of two parallel flows. The vorticity thickness can then be calculated using the formula:

$$\delta_\omega = \frac{|U_1 - U_2|}{\max\left(\frac{\partial U}{\partial n}\right)} \tag{6.1}$$

Here, U_1 and U_2 represent the velocities of the two layers, and n is the direction perpendicular to the shear plane. According to Terracol et al. [74], the most unstable wavelengths in the perpendicular x and z directions are given by $\lambda_x = 7\delta_\omega$ m, and $\lambda_z = 14/3\delta_\omega$ m, respectively.

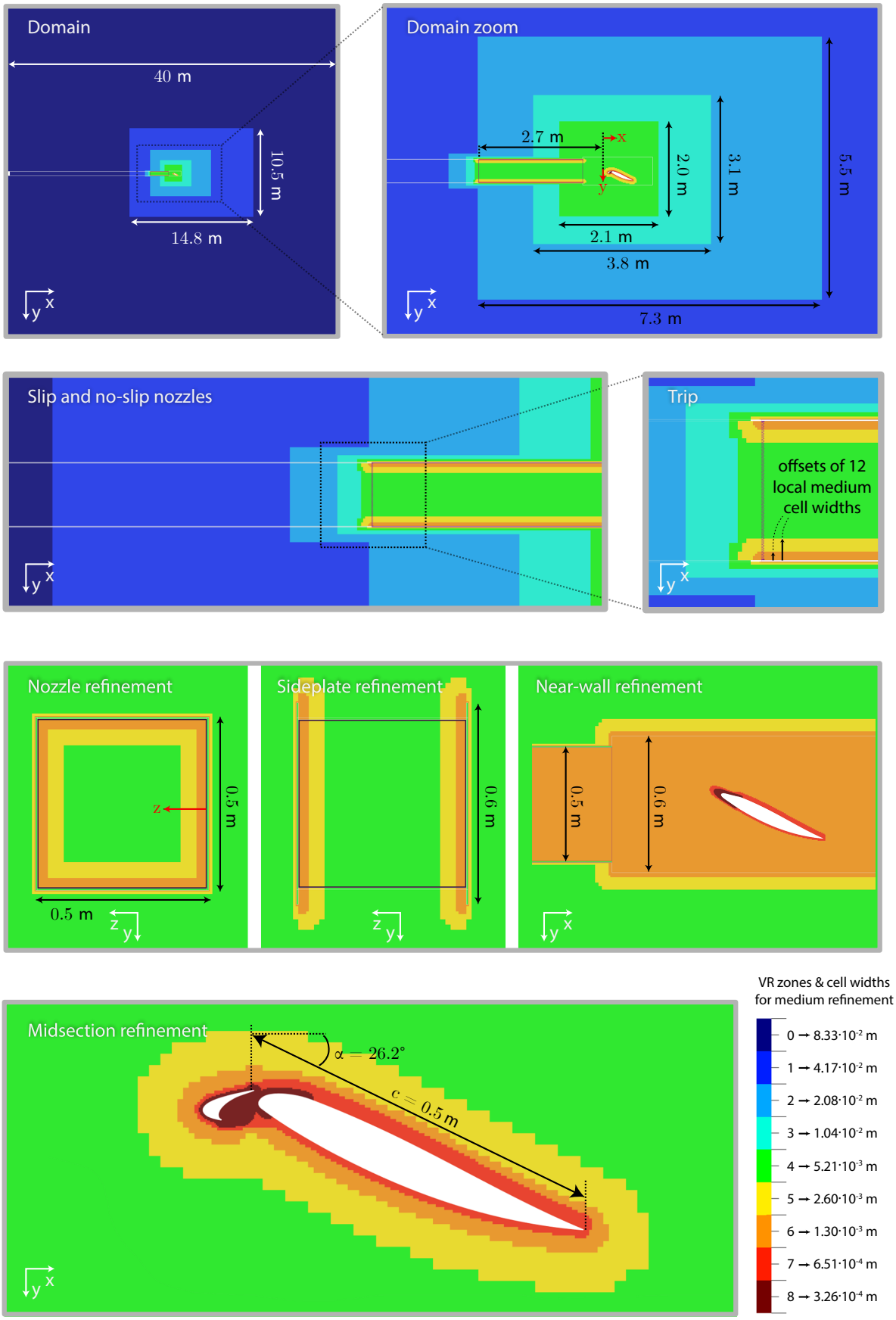

Figure 6.2: Description of mesh discretisation by Variable Resolution (VR) zones. The cell widths per VR zone are provided for the medium grid refinement.

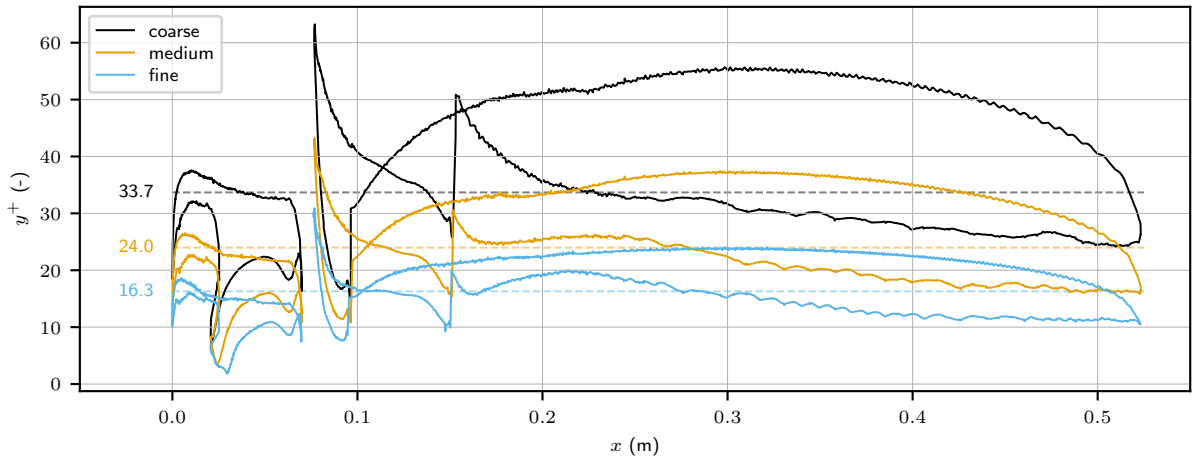

Figure 6.3: Distribution of y^+ on the midsection ($z = 0.5b$) of the 'Horn & Smooth Stump' geometry for three different mesh refinements. The median y^+ of each refinement is shown using a dashed ($--$) line.

Botero et al. [80] performed a simulation on a slat of similar size at a comparable Reynolds number, without sweep. They found a vorticity thickness of $\delta_\omega \approx 7.4 \cdot 10^{-4}$ m near the slat cusp, which is the most critical point for the vortices, at 10% of the cusp-to-trailing-edge shear line. Assuming a vortex thickness similar to that found by Botero et al. [80], there are 11, 16, and 24 cells for the most unsteady λ_x wavelengths for the coarse, medium, and fine simulations, respectively. For λ_z unsteadiness, there are 7, 11, and 16 cells for the coarse, medium, and fine simulations, respectively. Assuming it requires 4 cells to capture the swirling motion of an eddy, all refinements may capture the instabilities. However, the margins for the coarse variants are small, especially considering that the vortex thickness is based on data from literature. A grid convergence analysis will provide further insights into the performance of each grid refinement. The results of the grid convergence analysis, based on Roache [81], are presented in section 7.1.

The y^+ target for the simulation on which the aeroacoustic analysis is to be performed was 25 - a value based on earlier open-jet PowerFLOW aeroacoustic research by Teruna et al. [82], who found satisfactory mesh convergence at $y^+ = 25$. A finer y^+ was considered infeasible due to the relatively high chord-based Reynolds number of about a million, and the need for simulation of the boundary layer within the no-slip nozzle. Figure 6.3 illustrates the achieved y^+ distribution of the coarse, medium, and fine refinements on the midsection of the 'Horn & Smooth Stump' geometry. The set-up has a median y^+ of approximately 24.0 for the medium refinement. The substantial y^+ jump at $x = 0.15$ m is a result of the VR-zone change.

6.3. Acoustic sponge zone definition

Boundaries reflect a wave as the wave's fluctuations must go to zero at a wall which sends a mirrored/reflected wave back to the source. Similarly, any numerical boundary with a prescribed property will cause reflections (illustrated in appendix E). To minimise numerical acoustic reflections, either a very large domain must be used, or the acoustic fluctuations must be dampened while largely keeping the aerodynamic response the same. A numerical acoustic sponge zone placed far enough away from the nozzle exit achieves this by increasing the fluid's viscosity to temperature ν/T ratio, which enhances the fluid's resistance to fluctuations [82]. A step change in this ratio will induce its own reflections, therefore the ν/T ratio should be altered such that its value and its derivatives smoothly transition to a prescribed increased value. For this purpose an S-shaped logical function starting from $(\nu/T)_{min}$ to $(\nu/T)_{max}$ was developed

$$\frac{\nu}{T}(r) = (\nu/T)_{min} + \frac{(\nu/T)_{max} - (\nu/T)_{min}}{1 + \exp(-s(r - r_{\text{inflexion}}))} \tag{6.2}$$

where r is the radial distance from the domain centre, $r_{\text{inflexion}}$ the location of the inflexion point of the S-shaped function and s the steepness of the curve. PowerFLOW allows for prescribing additional ν/T (see appendix E for a more elaborate manual on how to use an anechoic sponge zone with PowerFLOW). A visualisation of the ν/T addition used in this study is provided in figure 6.4.

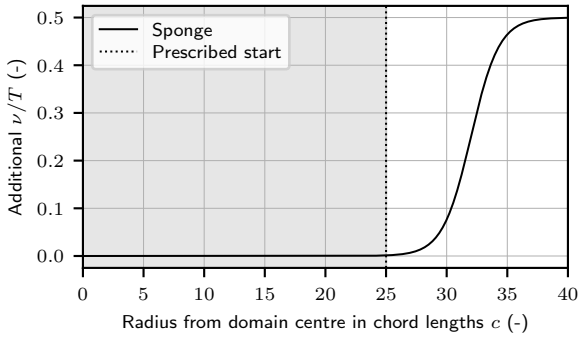

Figure 6.4: Visualisation of the transition of the viscosity over temperature ratio ν/T.

6.4. Description of measurements

The numerical measurements defined for each simulation are based on verifying the **simulation** itself, checking the **design** considerations from literature, addressing the research **questions** defined in section 2.2, comparing to measurements from **literature** described in table 4.5, and performing a grid **convergence** study between different mesh refinements. A full overview of all measurements, their location, their goal, their relation to the five categories defined above, their resolution, measurement time, averaging period and averaging frequency are provided in appendix F.

7

Verification & validation

This chapter discusses the grid independence analysis in section 7.1, compares the research set-up and model to other scaled studies in section 7.2, and rescales the noise radiation to full-scale conditions, after which it is compared to flyover and full-Reynolds number results in section 7.3.

7.1. Grid independence analysis

A tabulated overview of the grid refinement parameters is provided in subsection 7.1.1. Thereafter, sections 7.1.2, 7.1.3, 7.1.4, and 7.1.5 analyse the grid in terms of asymptotic convergence for lift & drag, surface streamline topology, streamwise loading, and far-field noise, respectively.

7.1.1. Grid parameters overview

A coarse, medium, and fine grid separated by a refinement factor of $r = 1.5$ were considered. All grids employ nine VR zones at the same locations, depicted in figure 6.2. The largest voxel size VR0, smallest voxel VR8, median y^+, total number of voxels N_{voxels}, number of fine equivalent voxels $N_{fine\ eq.}$, number of timesteps $N_{timesteps}$, and the number of CPU hours CPUh are provided in table 7.1.

Table 7.1: Grid refinement parameters

		Coarse	Medium	Fine
VR0 size	(m)	$c/4$	$c/6$	$c/9$
VR8 size	(m)	$c/1024$	$c/1536$	$c/2304$
Median y^+	(-)	33.7	24.0	16.3
N_{voxels}	(-)	$138 \cdot 10^6$	$451 \cdot 10^6$	$1465 \cdot 10^6$
$N_{fine\ eq.}$	(-)	$34.1 \cdot 10^6$	$109 \cdot 10^6$	$349 \cdot 10^6$
$N_{timesteps}$	(-)	$483 \cdot 10^3$	$724 \cdot 10^3$	$1086 \cdot 10^3$
CPUh	(h)	$5.659 \cdot 10^3$	$23.81 \cdot 10^3$	$83.41 \cdot 10^3$

7.1.2. Lift & drag based grid convergence

The grid convergence analysis aims to select the cheapest grid that shows adequately converged results. The grid independence analysis was performed on the Horn & Smooth Stump geometry. The Grid Convergence Index GCI helps estimate the deviation of an integral parameter on a given grid to an asymptotic solution for an infinitely fine grid. The asymptotic solution can be estimated using a Richardson extrapolation [81]. Figure 7.1 demonstrates the convergence trend of the integral lift and drag coefficients C_l and C_d. The drag coefficient shows a negative order of convergence p, i.e. the deviation between the medium and fine grid is larger than the deviation between the medium and coarse grid, indicating it has not reached a satisfactory asymptotic convergence. The GCI for the lift coefficient transitioned from coarse to medium grid at $GCI_{c,m} = 0.257\%$ and from medium to fine grid at $GCI_{m,f} = 0.096\%$, yielding a GCI ratio of approximately 1, specifically 1.0095. The calculated order of convergence p was 2.50. The small value of the medium GCI and the GCI-ratio close to unity indicates that the medium refinement lies within the asymptotic range of convergence for the lift coefficient [81].

The stability over time of the lift and drag coefficients is subject to discussion. The mean progression of the coefficients by averaging period visualised in figure 7.2, indicates neither force has fully reached

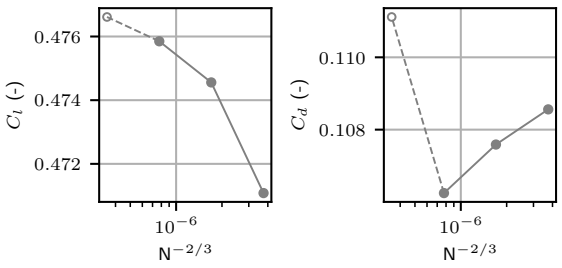

Figure 7.1: Richardson extrapolation of the lift (left) and drag (right) coefficient of the 'Horn & Smooth Stump' model.

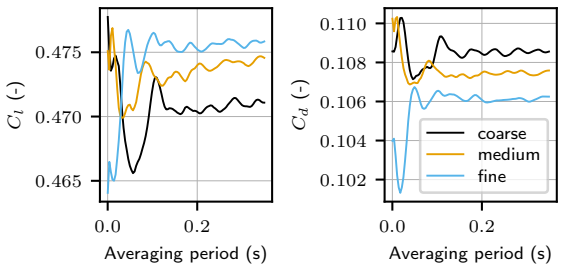

Figure 7.2: Mean progression of the lift (left) and the drag (right) by averaging period of the 'Horn & Smooth Stump' model.

its asymptotic mean, questioning the validity of the Richardson extrapolation's magnitudes. However, the trends show that increasing the lift coefficient's C_l averaging period will result in a smaller deviation between the medium and fine grids, than between the medium and coarse grid, indicating asymptotic convergence.

7.1.3. Time-averaged surface streamlines

Surface streamline visualisations allow for qualitative assessment and comparison of the flow behaviour across grid refinements. Figure 7.3 presents a comparison of streamlines and skin friction across grid refinements on the set-up's suction side and inside the slat cove (a plane looking towards the mean flow direction). Streamlines on the suction side of the element exhibit similar flow patterns across all cases, where the medium and fine case are in close agreement on the slat stump (region A in Figure 7.3), near the leading edge (B) and near the outboard sideplate (C). This indicates that vortices arising near the

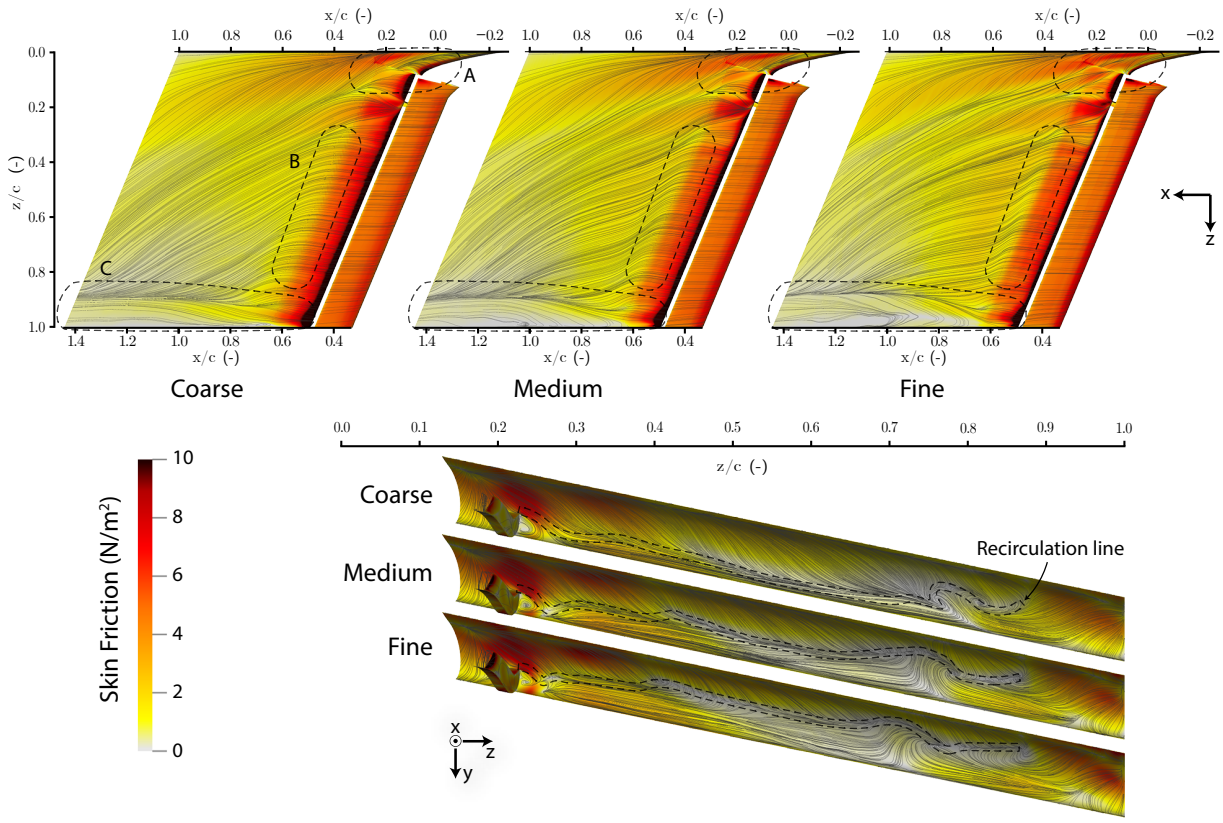

Figure 7.3: Streamline and skin friction visualisation of the three grid refinements of the 'Horn & Smooth Stump' model using an averaging period of 0.33 s, resulting in roughly 130 slat flow-throughs at a slat-based Strouhal number of $St_{c_s} = 8.3 \cdot 10^{-3}$.

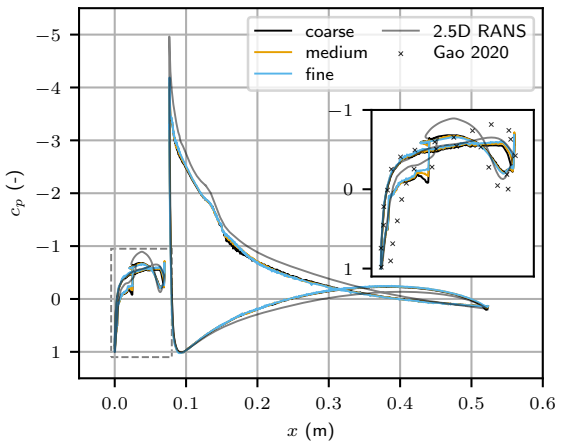

Figure 7.4: Pressure coefficient distribution of the mesh refinements and the 2D RANS simulation of the 'Horn & Smooth Stump' model.

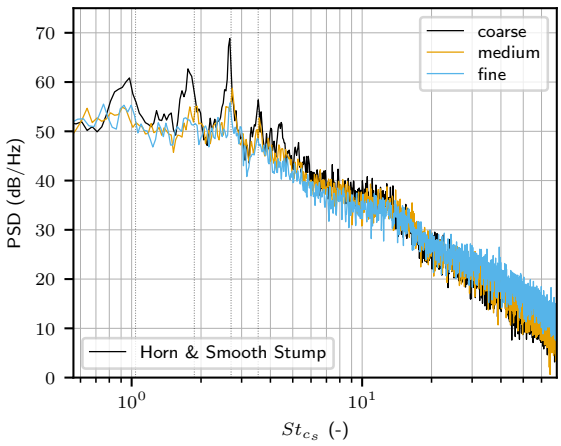

Figure 7.5: Power spectral density of the mesh refinements with a resolution of $\Delta f = 12$ Hz $\rightarrow \Delta St_{c_s} \approx 0.034$ at $x, y, z = (0.0, 1.6c, 0.5b)$ of the 'Horn & Smooth Stump' model.

junctions are similar between the medium and fine cases, and to a lesser degree to the coarse case. The skin friction and streamlines within the slat cove show a significant deviation between the coarse case, and the medium & fine cases. The recirculation line extends considerably further towards the slat cusp in the coarse simulation. The fine simulation predicts a recirculation area (from the slat trailing edge to the recirculation line) slightly smaller than the medium case. Their overall patterns are similar. In conclusion, the medium and fine cases are in close agreement in terms of flow pattern, whereas the coarse case deviates from the other two.

7.1.4. Time-averaged streamwise loading at z = 0.5b

The streamwise pressure coefficient distribution describes the streamwise force distribution per spanwise section. Figure 7.4 displays the loading of three PowerFLOW grid refinements, the 2D two-element RANS simulation for the slat and main element, and the 2D three-element RANS simulation from Gao et al. [76] for the slat. A finer grid corresponds slightly more closely with the RANS 2D case. Each refinement results in an increased extent of the suction peak, showing still a minimal trend towards complete convergence. The point of loading reversal on the main element is positioned more forward in the PowerFLOW simulations than in the RANS, likely attributable to the jet expansion in the PowerFLOW open-jet setup. The trends in the loading curves are captured identically in all refinements. Lastly, the PowerFLOW cases align more closely to the numerical data from Gao et al. [76] than the two-element RANS performed for this study. In short, all grid refinements are near-converged in terms of streamwise loading. This observation provides confidence in using a coarse grid to perform preliminary analyses such as an effective angle of attack correction, as described in subsection 5.2.3.

7.1.5. Far-field noise

Figure 7.5 compares the effect of grid refinement on far-field noise from a numerical probe in the mid-plane $z = 0.5b$, $1.6c$ below the slat-retracted leading edge, $(x, y, z) = (0.0, 1.6c, 0.5b)$, by considering the acoustic pressure power spectral density (PSD). The observations will be discussed in terms of broadband noise and narrow-band Rossiter-like slat peak noise. The broadband noise across grid refinements is largely similar. A finer grid decreases the broadband noise below a slat-based Strouhal number of $St_{c_s} \approx 15$, above which a finer grid increases the broadband noise. The coarse grid predicts significantly higher intensity narrow-band peaks than the medium and fine case. In short, the medium and fine case show similar noise radiation, and noise radiation patterns, which makes the medium refinement as good for noise mechanism analyses as the fine case. The sharp difference with the coarse variant is likely related to the dissimilar flow patterns in the slat cove, as the slat peaks are the dominant noise sources.

7.2. Scaled junction model literature comparison

Subsection 7.2.1 tabulates the main set-up characteristics for available fuselage-wing-slat junction studies. Subsection 7.2.2 discusses the (dis)similarities of the models and results for available comparable data.

7.2.1. Scaled junction model research set-up overview

Table 7.2 compares the literature research set-ups to the set-up used in this study. The overview shows that all simulated junction studies have been performed using LBM solvers. The geometries are often difficult to reproduce, either because of the availability of the geometry, or because of the size of the model, which only fit in large wind tunnels. None of the studies reports on the effect of different slat horn or slat stump surface geometries. Sweep is used in all models, but only Ribeiro et al. [34] report on its effect on noise. In short, the set-ups from literature were created to study specific aspects of the fuselage-wing-slat junction noise mechanism. This study, instead, aims to provide a more holistic overview of the possible noise sources. Moreover, the simple geometry used in this study, based on open-source data, improves the reproducibility for future fuselage-wing-slat junction studies.

Table 7.2: Model specification and flow condition comparison from fuselage-wing-slat junction studies.

	Molin et al. (2003) [63]	Lockard et al. (2017) [72]	Lockard et al. (2022) [68]	Ribeiro et al. (2022) [34]	Bai et al. (2023) [62]	Murayama et al. (2023) [35]	This study Piera (2024)
Simulation	N/A	LBM (free-flow)	LBM (free-flow)	LBM (free-flow)	N/A	LBM (free-flow)	LBM (open-jet)
Wind tunnel	Open Jet	N/A	Open Jet	Open Jet	Closed Jet	Closed Jet	Open Jet[a]
No. walls	2	N/A	1	1	4	4	2
Model geom.	Simplified junction section	10% scale HL-CRM half-aircraft	10% scale HL-CRM half-aircraft	Junction modified OTOMO2	9.24% scale Dornier 728 half-aircraft[b]	10% scale 'Regional Jet' type half-aircraft	Modified 30p30n junction section
Airfoil (public data)	N/S (No)	NASA CRM-HL based (On request)	NASA CRM-HL based (On request)	JAXA JSM based (On request)	N/S (No)	N/S (No)	Modified two-element 30P30N (Yes)
Slat horn	Present & absent configurations[c]	Absent	Absent	Absent	Absent	Absent[d]	Present & absent configurations
Slat stump	Step & smooth configurations[c]	Step	Step	Step	Step	Step	Step & smooth configurations
Slat flange	N/S	N/S	N/S	Present	Present	Present	Present
Slat track (fidelity)	Present (low)	Present (N/S)	Present (N/S)	Present (high)	Present (high)	Present (high)	Present (low)
Sweep (°)	Yes (N/S)	Yes (35)	Yes (35)	Yes (27-37)	Yes (23.5)	Yes (N/S)	Yes (25)
Chord (m)	N/S	0.70	0.70	0.57	0.35	N/S	0.50
Half-span (m)	N/S	2.94	2.94	1.15	1.44	N/S	0.50
AR (half-span/ chord)	N/S ($\ll 1$)	4.2	4.2	2.0	4.1	N/S (~ 4)	1.0
Re. number	N/S	$3.3 \cdot 10^6$	$3.3 \cdot 10^6$	$2.6 \cdot 10^6$	$1 \cdot 10^6$ - $9 \cdot 10^6$	N/S	$1.0 \cdot 10^6$
Mach number	N/S	0.20	0.12 - 0.20	0.20	0.15 - 0.25	N/S	0.09
Velocity (m/s)	60 - 80	N/S	N/S	N/S	N/S	N/S	30

[a] Designed for a numerical and experimental open-jet tunnel. Experiments not performed in this study.
[b] Unlike suggested by the article, the model used has a Krüger flap as inboard leading edge high-lift device.
[c] Article does not individually report on the different configurations.
[d] Does propose other side-edge modifications, such as a smooth side-edge, and a modified slat cusp.

7.2.2. Scaled junction model literature comparison

Out of the six fuselage-wing-slat junction studies, the work from Ribeiro et al. [34] and Murayama et al. [35] have discussed similar measurements as this study. Therefore, only results from those studies will be

compared to the present case.

Slat loading

The slat loading is hypothesised to have a large influence on the fuselage-wing-slat vortices and noise response. This study used a largely unloaded slat, as the 30P30N at an angle of attack of $4.0°$ is largely unloaded. Ribeiro et al. [34] analysed the junction noise using a research set-up employing a loaded slat. A comparison between slat loading is provided in figure 7.6. Neither pressure coefficients have been corrected for sweep angle. The study from Ribeiro et al. [34] revealed a noise increase with the introduction of a fuselage-slat gap. However, as will be presented in chapter 8, this study did not find a noise increase when opening the gap. Unfortunately, Ribeiro et al. [34] does not provide a visualisation of vortices and their strength in the junction, hence it is uncertain whether their noise increase from a fuselage-slat gap is caused by the size and strength of slat-loading based roll-up vortices. The effect of slat loading on a model with a fuselage-slat gap would be an interesting follow-up to this study.

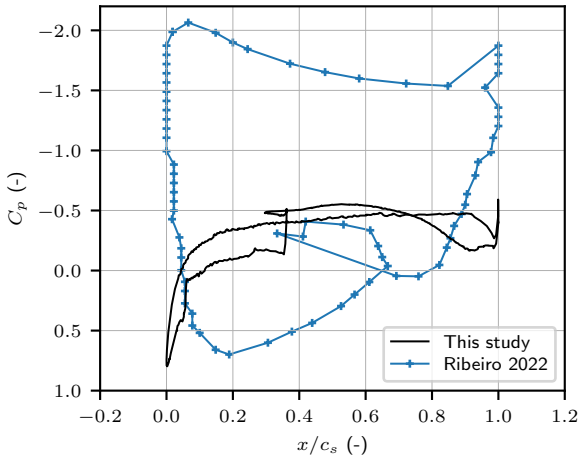

Figure 7.6: Comparison of slat pressure coefficient C_p distribution between this study and the study from Ribeiro et al. [34].

Slat surface pressure fluctuation intensity

Surface pressure fluctuation intensity can serve as an indication of impingement noise radiation. It can also provide insights into the turbulent structures near the surface. Ribeiro et al. [34] presents the pressure fluctuation intensities inside the slat cove near the slat root. Figure 7.7 qualitatively compares

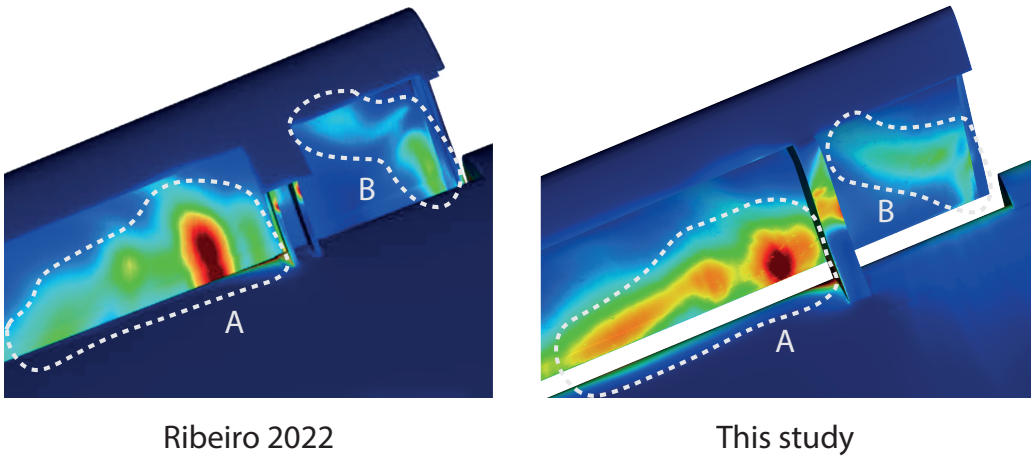

Figure 7.7: Qualitative pressure fluctuation intensity comparison to Ribeiro et al. [34] in the slat cove near the slat side-edge. The right image, this study, uses a colour range between p'_{rms} $0 - 200$ Pa.

the pressure fluctuation intensity between their study and the No Horn & Step Stump geometry from this study. Unfortunately, Ribeiro et al. [34] does not present the limits of the p'_{RMS} colouring. Two similar behaving regions can be distinguished. Region A, outboard of the slat track, shows the highest pressure fluctuation area just aft of the track for both studies, aft of which more secondary interactions occur. These secondary fluctuations are relatively weaker for the study from Ribeiro et al. [34] than for this study. Region B encircles the pressure fluctuations from turbulent structures that move via the slat side-edge to inside the cove. These interactions seem similar in both cases. Based on these fluctuation intensity patterns it seems that the flow structures inside the slat cove are similarly influenced by the cross-flow from the slat-side edge. Therefore, both simulations capture a similar effect of the cross-flow on turbulent structures inside the slat cove, further explored in chapter 8.

Vorticity in the slat cove near the side-edge

The vorticity magnitude visualisations in figure 7.8 show similar flow structures, and flow behaviour, which aids the confidence in the simulation. However, some discrepancies are present. Murayama et al. [35] identified the impingement of a slat cusp roll-up vortex with the slat track as a possible noise source. By comparison, this study did not generate a similarly coherent slat cusp roll-up vortex (figure 7.8, region A). Unfortunately, Murayama et al. [35] did not present the pressure coefficient distribution of the slat. Hence, whether this discrepancy is influenced by a difference in slat loading is unknown. However, it remains uncertain whether the vortex impingement from Murayama et al. [35] is actually a dominant noise source. Their band-passed filtered surface pressure fluctuation intensity visualisations show no meaningfully different intensity on the track itself, compared with the rest of the slat cove.

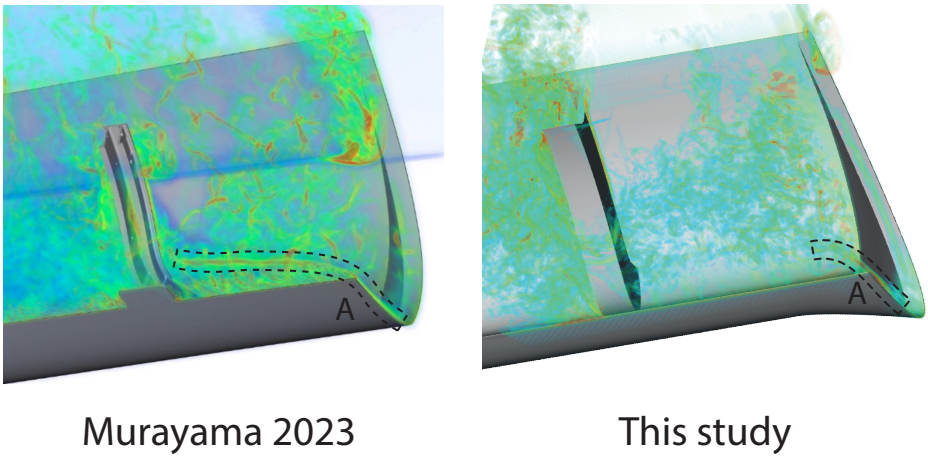

Figure 7.8: Qualitative vorticity magnitude comparison to Murayama et al. [35]. The right image visualises the vorticity magnitudes between 10000 Hz and 60000 Hz.

This study questions if track impingement is a high-intensity noise source. A high-intensity pressure fluctuation source is predicted at the aft-side of the track due to recirculated flow, as shown in figure 7.9. An FW-H analysis (verified in section 8.1), however, reveals that the track noise is insignificant compared to the total noise, as shown in figure 7.10. The 'No Gap' geometry has less track noise due to minimal separation aft of the slat track. However, this is not measurable in the total noise radiation when compared to the 'NH' and 'H' models. Therefore, it is unlikely that impingement on the track is the root cause of noise. A noise reduction method devised by Murayama et al. [35] to minimise track impingement noise did decrease the total noise. However, their side-edge modification likely helps to minimise the impingement of separated turbulent structures in the entire slat cove, not just on the slat track, as further explored in chapter 10.

Noise radiation

Some trend comparisons can be struck between our latest study and the study from Ribeiro et al. [34]. Ribeiro et al. [34] also compared a 'No Gap'-variant with a 'Gap'-variant, both of which without slat tracks. In their case, the introduction of a fuselage-slat gap increased the noise by roughly 4 dB above 1000 Hz in

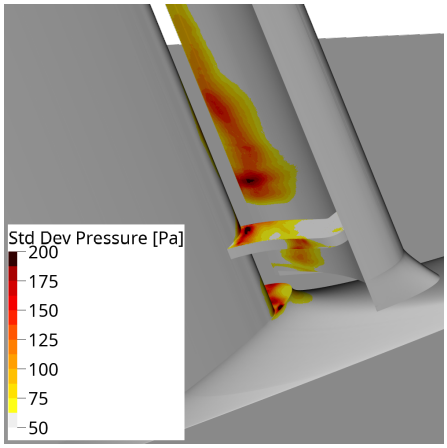

Figure 7.9: Pressure fluctuation intensity on the slat track through the standard deviation of the surface static pressure.

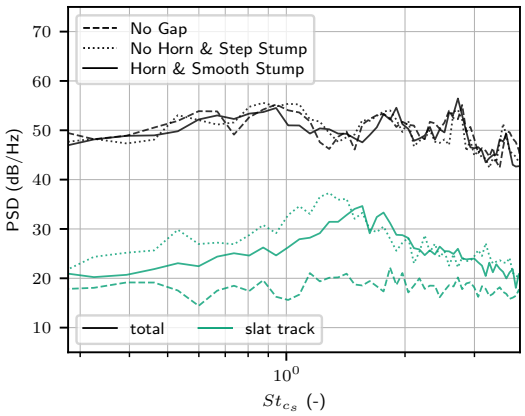

Figure 7.10: Power spectral density from a solid formulation of the FW-H equation for total and slat track noise with a resolution of $\Delta f = 24$ Hz $\rightarrow \Delta St_{c_s} \approx 0.067$ at $x, y, z = (0.0, 1.6c, 0.5b)$.

model frequency, which, given a slat chord length of $c_s = 0.15c$ with $c \approx 0.57$, Mach number of $M \approx 0.2$ and a sweep of $\phi = 33°$ is roughly equivalent to a noise increase above $St_{c_s} \approx 1.5$. This contrasts the results presented in chapter 8, which describes a slight noise decrease for the 'Gap'-variants. The author hypothesises that this discrepancy is two-fold. Firstly, Ribeiro et al. [34] compares the two geometries without the presence of a slat track. However, the difference in noise radiation for two of their 'No Gap' geometries - one with, and one without slat tracks - showed a significant $5+$ dB noise increase for the case with tracks, exceeding the noise increase from the introduction of a fuselage-slat gap. It could be that the presence of tracks nullifies the noise increase from the fuselage-slat gap itself. A second explanation was already briefly alluded to: the more significant slat loading from Ribeiro et al. [34] could result in larger coherent roll-up vortices causing intense pressure fluctuations near the slat trailing edge.

7.3. Full-scale junction noise literature comparison

This section investigates the correlation between the far-field noise of the scaled research model and the flyover data from an Airbus A320. The results of the noise scaling will serve as an indicator of whether the measured intensities correspond to full-scale noise, and thus the correct noise generation mechanisms. The comparative flyover data is derived from the paper by Siller et al. [14], who presented a component-based third-octave band noise spectrum using Doppler shift corrected deconvoluted beamforming integration areas. The spectra from a single A320 flyover have already been shown in figure 4.1. In their results, the fuselage-wing-slat junction was referred to as the 'slathorn'.

Table 7.3: Noise scaling properties for the Airbus A320 and the fuselage-wing-slat junction model.

Property	Value	Source	Comment
Slat chord length Airbus A320	0.51 m	[83]	Through comparative analysis of other given lengths
Approach certification speed Airbus A320	77 m/s	[84]	Based on $V_{cert} = V_{app} + 10$ kts [85]
Span part of beamforming integration window	1.52 m	[14]	Through comparative analysis of other given lengths
Distance to microphone array	120 m	[14]	Normalised and atmospheric absorption corrected
Slat chord scaled model	0.075 m	-	From $c_s = 0.15c$ with $c = 0.5$ m
Flow speed scaled model	29.6 m/s	-	Nozzle exit velocity through pressure differential
Span scaled model	0.5 m	-	Width of the 50×50 cm nozzle
Distance to microphone probe	0.738 m	-	Euclidean distance from radiation centre to probe

7.3.1. Noise power and frequency scaling

The scaling properties used are detailed in table 7.3. The airspeed of the Airbus A320 from the flyover data, as provided by Siller et al. [14], was not available. Therefore, an estimate was made for the likely certification speed, based on online sources and the definition of the certification speed. Furthermore,

the slat chord length of the Airbus A320 is not publicly accessible. An estimate was made for the chord length through a comparative analysis of other available length scales. The implications of the velocity assumptions will be addressed in subsequent sections.

Sound corrections in decibel scale can be performed through addition. For this comparison, the corrections described in eq. (7.1) and table 7.4 were performed based on the values provided in table 7.3.

$$L_{\text{corr}} = L_{\text{raw}} + \Delta L_{\text{flow speed}} + \Delta L_{\text{turb scale}} + \Delta L_{\text{span}} + \Delta L_{\text{N sides}} + \Delta L_{\text{distance}} + \Delta L_{\text{reflections}} \tag{7.1}$$

Table 7.4: Definitions of sound scaling corrections

Correction	Scales on	Relation	On model	On A320
$\Delta L_{\text{flow speed}}$	Velocity U^5	$+5 \cdot 10 \cdot \log\left(U_{\text{A320}}/U_{\text{model}}\right)$	Yes	No
$\Delta L_{\text{turb scale}}$	Turbulence scale $\delta \sim c_s$	$+1 \cdot 10 \cdot \log\left(c_{s_{\text{A320}}}/c_{s_{\text{model}}}\right)$	Yes	No
ΔL_{span}	Span b	$+1 \cdot 10 \cdot \log\left(b_{\text{Siller 'slathorn'}}/b_{\text{model}}\right)$	Yes	No
$\Delta L_{\text{N sides}}$	No. sides $N = 2$	$+1 \cdot 10 \cdot \log\left(2\right)$	Yes	No
$\Delta L_{\text{distance}}$	Distance d^{-2}	$-2 \cdot 10 \cdot \log\left(d_{\text{A320}}/d_{\text{model}}\right)$	Yes	No
$\Delta L_{\text{reflections}}$	Reflection correction for hard surfaces 2^{-2}	$-2 \cdot 10 \cdot \log\left(2\right)$	no	Yes

Both the full-scale and model-scale consider the primary noise radiation direction to be perpendicular to the slat chord, dependent on the slat deflection δ_s and the angle of attack α. Figure 7.11 illustrates the significant angles for calculating the effective comparative emission angle η. The position of the microphone is considered to align with the radiation centre in the z-direction. The power spectra from Siller et al. [14], recorded at an approximate height of 120 m, lead to the assumption that the radiation centre and microphone locations align in the x-direction, resulting in an effective emission angle of:

$$\eta_{\text{A320}} = \gamma_{\text{A320}} = \delta_{s_{\text{A320}}} - \alpha_{\text{A320}} \approx 23°$$

as per figure 7.11a with $\delta_{s_{\text{A320}}} \approx 27°$ and $\alpha_{\text{A320}} \approx 4°$ for the spectra presented as overhead $90°$. The scaled model probe data was taken much closer to the radiation centre, which is why for the scaled model the effective emission angle was taken to be

$$\eta_{\text{model}} = \zeta_{\text{model}} + \gamma_{\text{model}} = \arctan\left(\frac{x_c - x_m}{y_m - y_c}\right) + \delta_{s_{\text{model}}} - \alpha_{\text{model}} \approx 19.5°$$

as per figure 7.11b with $(x, y)_c = (0.2, 0.09)$ m, $(x, y)_m = (0.0, 0.8)$ m, $\delta_{s_{\text{model}}} \approx 30°$ and $\alpha_{\text{model}} \approx 26.2°$. Sound diffraction of the open-jet shear layer was not taken into account, since the FW-H analysis (from

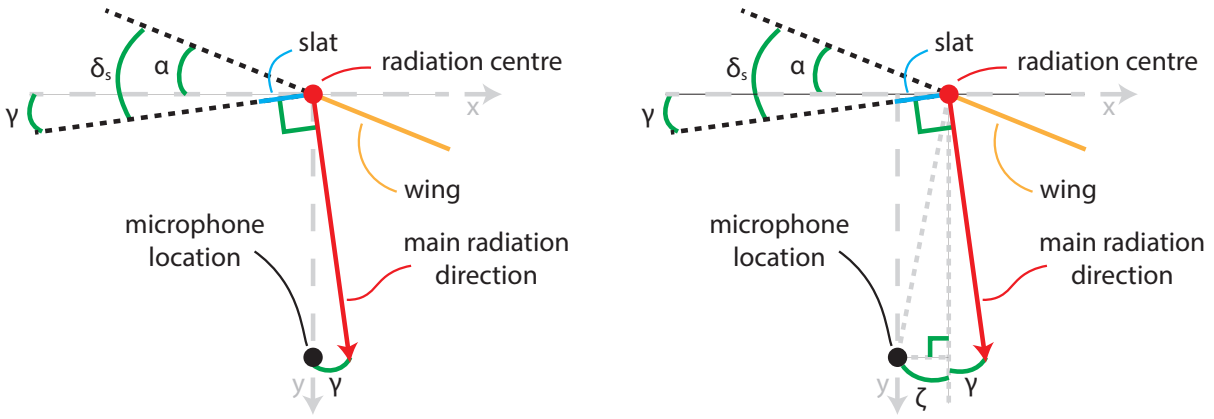

(a) Microphone directly below radiation centre

(b) Microphone offset from radiation centre

Figure 7.11: Definition of angles to determine the effective emission angle

which the model radiation centre was taken as well) was near-identical to the probe data, even though diffraction was not taken into account. This main noise radiation angle analysis reveals that overhead $90°$ spectra from Siller et al. [14] should correspond with the microphone location placed in the scaled model simulation, assuming that the approximate orientation of the slat chord determines the directivity pattern.

In addition to the noise power, the noise frequency also requires scaling. Strouhal frequency scaling, based on the slat chord, was employed as the slat noise was the dominant noise source across the frequency domain for the research setup and typically scales with Strouhal. The data from Siller et al. [14] is provided in third-octave bands. Consequently, the model probe frequency data was initially scaled to full-scale using the following formula:

$$f_{\text{full-scale}} = \frac{c_{s_{\text{model}}}}{U_{\text{model}}} \cdot \frac{U_{\text{A320}}}{c_{s_{\text{A320}}}} \cdot f_{\text{model}}$$

Subsequently, third-octave binning was performed. Following this, both the data from Siller et al. [14] and this study were non-dimensionalised to the slat-based Strouhal number, based on the full-scale velocity and length properties.

7.3.2. Comparison of flyover and full-scale Reynolds measurements

Figure 7.12a provides a third-octave band comparison between the reflection corrected 'slathorn' spectrum from Siller et al. [14], and the scaled spectrum of the research model used in this study for both the overhead $90°$ and the forward $60°$ direction. The $\pm 10\%$ U_∞ sensitivity bandwidth shows that, although the scaling is sensitive to the velocity, which was not provided by Siller et al. [14], in both power and frequency, the trends of the spectra remain largely unchanged. Above a Strouhal number of 8 the magnitude, slope, and general behaviour look remarkably similar. Below 8 the behaviour starts to deviate, with a slightly better match for the overhead $60°$ direction. Two possible explanations for this discrepancy, namely the Reynolds number difference, and the influence of Rayleigh's criterion, will be discussed in the next paragraphs.

The scaled research model in this study was tested at a Reynolds number of approximately one million, while an Airbus A320 in approach configuration operates at a Reynolds number of around twenty million. The discrepancy in low-frequency could be attributed to the higher Reynolds number promoting the transition from K-H-like isotropic turbulent structures, which induce the narrow-band peak resonance mechanism [87, 88], to 3D turbulent structures. The absence of resonance could explain the reduced amplitude of low-frequency noise radiation in figure 7.12a.

Ahlefeldt [86] conducted wind tunnel tests on a model Airbus A320 at full Reynolds scale ($Re_{MAC} = 20.06 \cdot 10^6$, $M = 0.2$). The data from their study represents the noise spectrum from full-span slat beamforming integration, not the fuselage-wing-slat junction. Figure 7.12b compares the scaled noise radiation spectrum to Siller et al. [14] quantitatively and to Ahlefeldt [86] qualitatively using third-octave

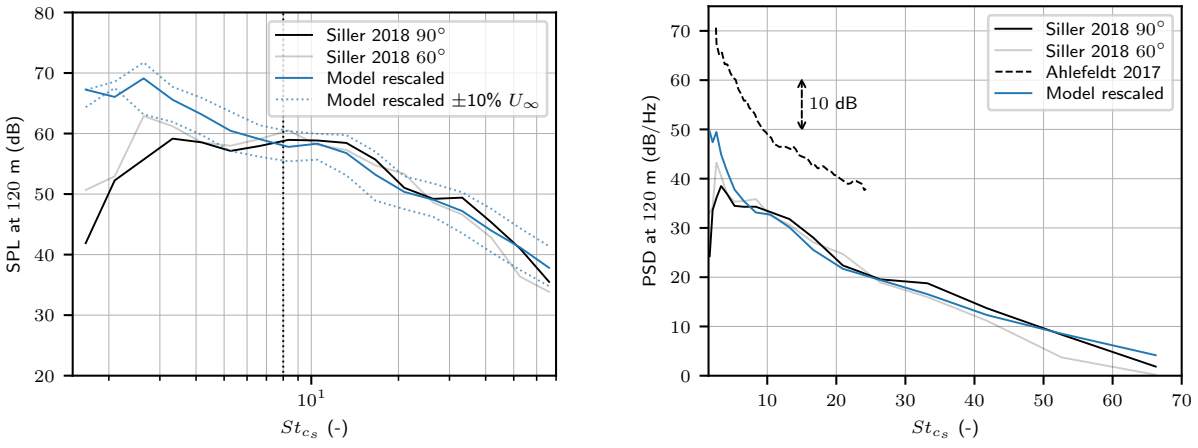

(a) Flyover to rescaled model far-field noise comparison in third-octave band SPL

(b) Flyover, full-scale Reynolds, and rescaled model far-field noise comparison in third-octave band PSD. The data from Ahlefeldt [86] was taken at $\alpha = 3°$

Figure 7.12: Rescaled model to full-scale far-field noise comparison

bands converted to power spectral density. Ahlefeldt [86] does not provide magnitudes for its noise spectra, only the scaling in dB, therefore their results are solely used for comparing spectral trends. The full-scale Reynolds number test from Ahlefeldt [86] results in narrow-band peaks, although not explicitly discussed in their paper. Furthermore, the slope of the noise radiation spectrum between this study and Ahlefeldt [86] is similar both below and above a Strouhal number of 8, as depicted in figure 7.12b. Therefore, the Reynolds number decreasing the low-frequency slat noise is not a plausible explanation for the low-frequency magnitude discrepancy.

The beamforming results for a model Airbus A320 at high Reynolds numbers are displayed in [86, fig. 10, 11]. These figures provide insights into the power discrepancy below $St_{c_s} = 8$. At low frequencies, specifically when $St_{MAC} = 20 \rightarrow St_{c_s} \approx 2.4$ (near a narrow-band resonance frequency), the inboard slat exhibits limited noise radiation compared to the outboard slats. The noise radiation from the outboard slat appears to originate from the slat cove between consecutive slat tracks. Conversely, at higher frequencies, such as $St_{MAC} = 190 \rightarrow St_{c_s} \approx 23$, the fuselage-wing-slat junction exhibits increased noise radiation compared to the outboard slats. The noise sources at these frequencies are located near the stump and the slat tracks, rather than between the tracks. The findings from Ahlefeldt [86] suggest that the presence of side-edge surfaces and multiple slat tracks near the inboard slat may reduce the low-frequency resonance mechanism and enhance the high-frequency impingement noise.

In conclusion, a higher Reynolds number is unlikely to account for the low-frequency noise discrepancy. Moreover, the magnitude-frequency trend between the full Reynolds number tests from Ahlefeldt [86] and this study seem to correlate both below and above $St_{c_s} = 8$. A possible physical explanation for the noise discrepancy at lower frequencies for the scaled model compared to flyover noise could be an over-prediction of narrow-band resonance noise in the absence of multiple slat tracks. However, this does not account for the full $10+$ dB difference. Therefore, another source of the discrepancy is more likely.

The deconvoluted beamforming data integrated by Siller et al. [14] is likely to underestimate the low-frequency noise originating from the fuselage-wing-slat junction. This observation calls for a critical examination of the Rayleigh criterion [43] by frequency. For small angles, the Rayleigh criterion is given by

$$W = \frac{rD}{\lambda z} \tag{7.2}$$

where r is the distance between two sources, D is the diameter of the microphone array, λ is an acoustic wavelength, and z is the distance from the source to the array (in this case the aircraft height). For this analysis, a Rayleigh criterion value of $W = 1.22$ is assumed, which is true for a circular microphone array with a continuous aperture. The microphone array used by Siller et al. [14] is 35×43 m, elongated along the flight path of the aircraft. In this analysis, a circular diameter of $D = 35$ m together with a speed of sound of $c_{sos} = 340$ m/s are used. Using the relation between frequency, speed of sound and wavelength, and eq. (7.2), the Rayleigh Radius r can be plotted against the frequency, as seen in figure 7.13. The figure

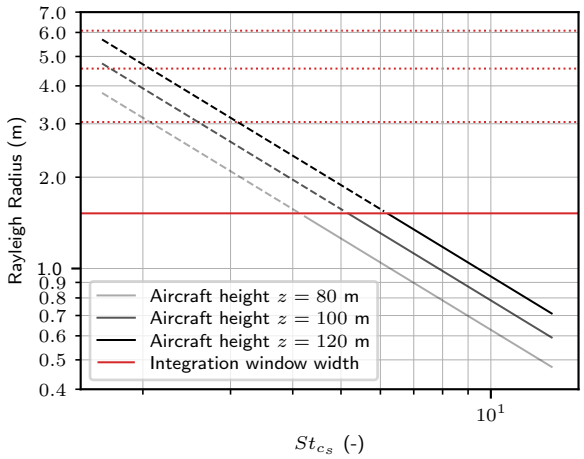

Figure 7.13: Rayleigh Radius r plotted against St_{c_s} for different flyover heights z compared to the integration window width of ~ 1.52 m used by Siller et al. [14]. The red dotted lines represent consecutive multiples of the integration window width.

displays the frequency above which two separate sources can still be distinguished within the integration window from Siller et al. [14] by solid lines. Dashed lines represent frequencies with a larger wavelength than the integration window width. Depending on the altitude of the particular flyover, the cross-over frequency varies. Nonetheless, given the Rayleigh radius for frequencies below $St_{c_s} = 8$, it is likely that some of the acoustic energy is not captured by the integration window, even though Siller et al. [14] aims to mitigate this by employing deconvolution methods on the raw beamforming data.

In conclusion, the far-field noise from the scaled research model generally agrees with full-scale fuselage-wing-slat junction measurements. The sound power discrepancy below $St_{c_s} = 8$ likely stems from a limitation of integrated beamforming noise spectra at low frequency as a consequence of the Rayleigh criterion, and possibly a limited over-prediction of the physical low-frequency resonance noise mechanism in the scaled research model.

8

Results

This section describes the main research findings of the report. Section 8.1 details the far-field noise radiation spectra of the three model geometries and discusses the far-field analysis approach. Section 8.2 describes the vortices in the junction and their effect on the noise production of the model. Lastly, Section 8.3 describes the influence of a sideplate-slat gap on the noise radiation from the slat cove. Lastly, the statistical significance of the noise radiation differences between the three model variations is discussed in section 8.4.

Table 8.1: Sound pressure level (SPL) and ΔSPL, compared to the NG geometry, in dB around the main Rossiter-like modes.

	$500-800$ Hz St_{c_s} $1.40-2.24$		$850-1150$ Hz St_{c_s} $2.38-3.22$		$1200-1500$ Hz St_{c_s} $3.35-4.19$	
NG	76.70,	N/A	77.58,	N/A	74.43,	N/A
NH	76.67,	-0.03	75.61,	-1.97	74.02,	-0.41
H	75.99,	-0.71	77.36,	-0.22	72.98,	-1.44

8.1. Far-field noise description of the model variants

This section explores the far-field noise radiation of the three different geometries using a direct numerical probe, and a solid formulation of the FW-H equation. All analyses are performed using the medium refinement. Figure 8.1 suggests that the geometries have the same spectral characteristics. At least four Rossiter-like modes are visible below $St_{cS} \approx 4$, after which the sound power tapers off. Between the Strouhal number of 10 and 20 a hump is present in the noise spectrum, which is related to the slat trailing edge turbulence [52, 53]. The geometries with a sideplate-slat gap (H and NH) consistently display (slightly) lower noise magnitudes at the main narrow-band peaks, resulting in an OSPL (St_{c_s} $0.3-70$) of

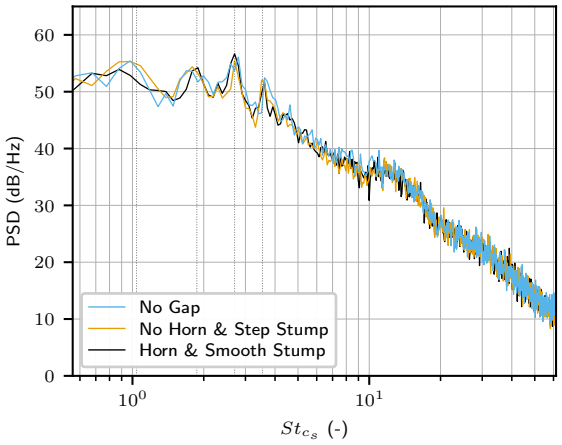

Figure 8.1: Power spectral density with a resolution of $\Delta f = 36$ Hz $\rightarrow \Delta St_{c_s} \approx 0.101$ at $x, y, z = (0.0, 1.6c, 0.5b)$.

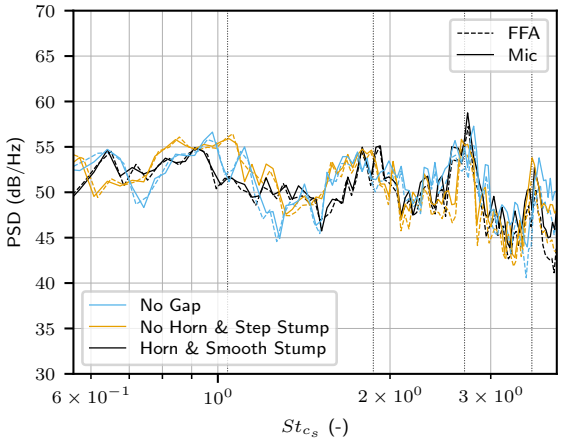

Figure 8.2: Probe and far-field analysis using a solid formulation of the FW-H equation with a resolution of $\Delta f = 12$ Hz $\rightarrow \Delta St_{c_s} \approx 0.034$ at $x, y, z = (0.0, 1.6c, 0.5b)$.

83.2 dB and 83.3 dB respectively, compared to 83.8 dB for the NG variant, as quantified by table 8.1. This contradicts earlier findings from literature that found a multiple decibel increase when a fuselage-slat gap was introduced [34, 68]. A second observation reveals that the NG geometry has its narrow-band peaks at slightly higher frequencies than the geometries with a sideplate-slat gap. These observations are further explained in subsequent sections.

The validity of using the solid formulation of the FW-H acoustic analogy is evaluated to provide confidence in the far-field analyses (FFA) performed in this study. Figure 8.2 compares the direct probe and FFA results for the three different geometries. In all three geometries, the FFA resulted in near-identical power spectral densities. The radiation starts to deviate slightly after a Strouhal number of 3.0, as the surface measurements from which the far-field radiations are constructed had a sampling frequency of roughly 5.5 times that number. The close match between the probe and far-field propagation provides confidence to use the FW-H-based results for a more in-depth analysis of the far-field noise mechanisms at Strouhal numbers below 3.0.

8.2. Impingement noise in the fuselage-wing-slat junction

The edges of surfaces in the junction cause vortex roll-up and flow separation. The vortical topology, surface pressure fluctuation intensities, and FW-H-based noise radiation per surface are discussed in sections 8.2.1, 8.2.2, and 8.2.3, respectively, to describe the flow and noise in the region from impingement.

8.2.1. Vortical topology in the junction

The fuselage-wing-slat junction generates multiple coherent vortices [65], which are hypothesised to influence the pressure fluctuation intensity on the surfaces, and hence the far-field noise radiation. A comparison of the vortex topology between the No Horn & Step Stump (NH) and Horn & Smooth Stump (H) designs is provided in figure 8.3. The vortices are visualised using a λ_2-criterion at $-4 \cdot 10^7$ and coloured by the streamwise vorticity. Both the NH and H geometries produce a roll-up vortex on the slat chord, where the H geometry's roll-up vortex is of greater size and vorticity strength due to the elongated side-edge (figure 8.3, region A). For both geometries, the vortex impinges on the slat trailing edge corner, after which it moves past the wing without impinging. The vortex arising at the trailing edge of the slat cusp, which traverses inside the slat cove, as predicted by Murayama et al. [35], is also more coherent for the H geometry (figure 8.3, region B). At the edge between the stump and wing, multiple vortices arise, which are of greater streamwise vorticity strength for the NH geometry. The vortices impinge on the side-edge of the slat stump, and on the main wing. A clear horseshoe vortex on the slat stump has not materialised for either geometry. In short, roll-up vortices are created on the slat side-edge, which scale on its length. These vortices, however, do not impinge meaningfully near the junction but might impinge on the stump side-edge, the slat trailing edge, and in the slat cove. However, the strength of these vortices is limited, likely related to the weak loading of the 30P30N's slat at the approach angle of attack of $4.0°$.

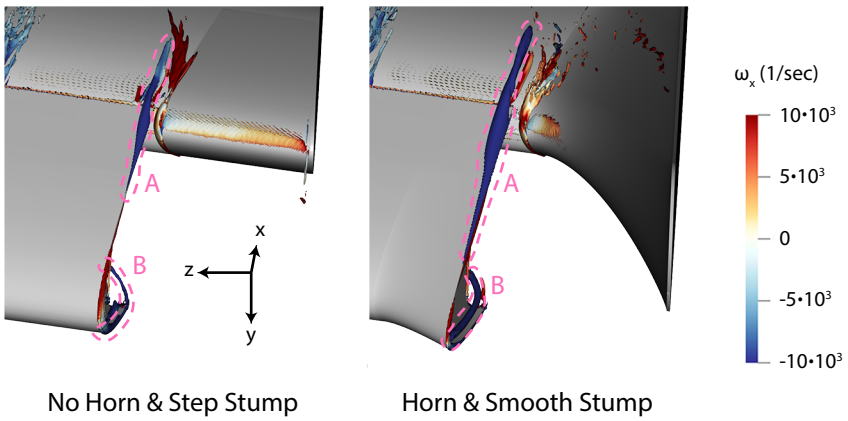

Figure 8.3: Vortex topology through $(\lambda_2 = -4 \cdot 10^7)$-iso-surfaces, coloured by the streamwise vorticity with an averaging period of roughly 4 streamwise slat passages or 0.0067 s. Blue indicates negative vorticity and red indicates positive vorticity.

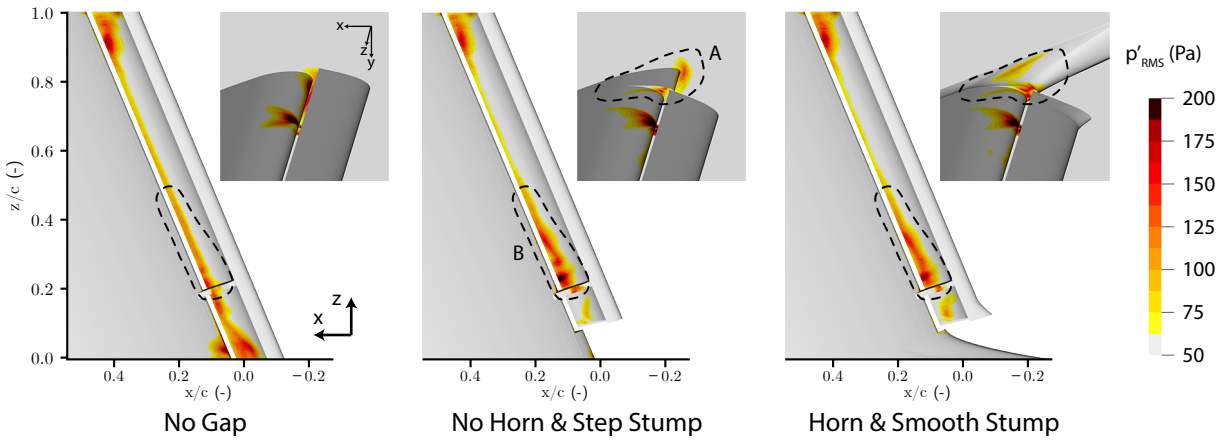

Figure 8.4: Pressure fluctuation intensities through p'_{rms} values for a flow duration of 0.33 s at a measurement frequency equal to the simulation's timestep frequency.

8.2.2. Surface pressure fluctuation intensity

If impingements from vortices in the junction are a root cause for the research set-up's noise, these would show up in surface p'_{rms} visualisations. Figure 8.4 presents the broadband surface pressure fluctuation intensity for all geometries. The intensities of the fluctuations originating from the expected vortices in the junction, encircled by region A in figure 8.4, are relatively weak. The fluctuation intensity from the side-edge roll-up vortex is barely discernible on the slat trailing edge. The side of the slat stump and the slat stump itself exhibit only moderate pressure fluctuation intensities compared to fluctuations stemming from turbulent structures from the slat track impinging on the main element's wing. Inside the slat cove, the influence of the sideplate-slat gap is clearly visible. The geometries that include a gap display a deep extent of high-pressure fluctuation intensities outboard of the slat track, encircled by region B in figure 8.4, with the highest intensity region just aft of the track. This pattern is not visible in the No Gap geometry, hence it must be related to the interplay between the sideplate-slat gap, and the track.

8.2.3. Noise radiation of different slat horn & stump geometries

The contributions to the total far-field noise per component can be quantified using the FW-H propagation of the surface pressure fluctuations, which has been verified in section 8.1. Figure 8.5 reveals that for both 'Gap'-geometries pressure fluctuations stemming from the slat span dominate the spectrum above $St_{c_s} \approx 1.1$, below which the wing is the dominant noise contributor. This trend continues for higher

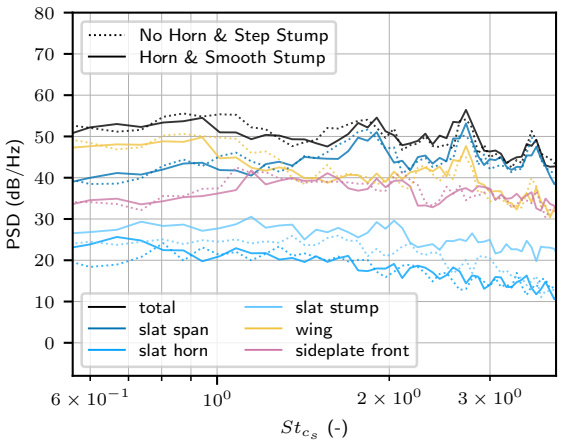

Figure 8.5: Component power spectral density from a solid formulation of the FW-H equation with a resolution of $\Delta f = 24$ Hz $\rightarrow \Delta St_{c_s} \approx 0.067$ at $x, y, z = (0.0, 1.6c, 0.5b)$.

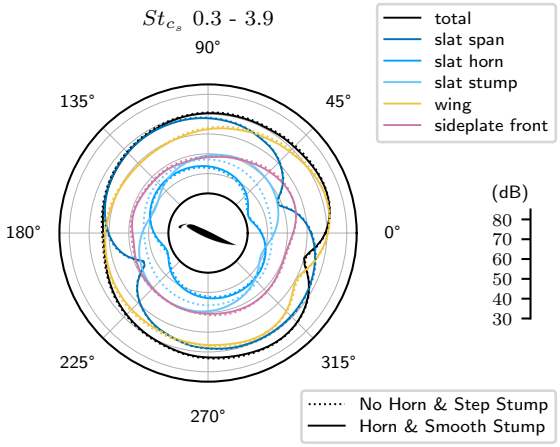

Figure 8.6: Directivity of the sound pressure level (SPL) from a solid formulation of the FW-H equation.

frequencies, although not visualised. Slight differences are present between the NH and H geometries. The PSD for all frequencies from the smooth stump exceeds those from the step stump (figure 8.5). However, this is likely caused by the increased surface area of the smooth stump, as the noise spectrum starts to correlate to the front sideplate (e.g. at $St_{c_s} \approx 2.0$). The marginally increased size and strength of the side-edge roll-up vortex for an elongated slat horn do not lead to a significantly altered far-field noise radiation. In short, given the current flow and loading conditions, the change in horn and stump design do not alter the noise radiation.

This observation holds for other directions as well. Figure 8.6 depicts the sound pressure levels derived from the solid FW-H propagation between St_{c_s} 0.3 and 3.9 in all directions in the midplane $z = 0.5b$, with the x_i, y_i coordinates of the microphones given by

$$\theta_i = 2\pi \cdot i / N_{\text{mics}} \qquad i = 0, 1, \ldots N_{\text{mics}} - 1$$
$$x_i = R \cdot \cos(\theta_i) + x_0$$
$$y_i = R \cdot \sin(\theta_i) + y_0$$

where the radius R was set to $4c$, and the origin x_0, y_0 to 0 m and 0.05 m respectively. The main difference between the two geometries is that the smooth slat stump exhibits a higher correlation with the front sideplate as it effectively morphs the sideplate with the main wing. Additionally, the clear dipole pattern of the slat span dominates the noise, except where the dipoles cancel each other ($30°$ and $210°$), at which point the wing noise level exceeds that of the slat. Lastly, in aft direction the total noise is shielded by the body, indicating that the main noise sources indeed lie near the leading edge of the research set-up. Hence, different horn and stump designs do not affect the total noise radiation under the current flow and loading conditions.

8.3. Slat cove noise influenced by large-scale 3D flow structures

Under the researched flow and loading conditions, noise due to direct impingements in the junction was not significant. However, as referenced in section 8.1, the model configuration that lacks a sideplate-slat gap exhibits higher intensity narrow-band peaks. Moreover, the frequencies of these narrow-band peaks deviate when the sideplate-slat gap is introduced. It is well recognised that these peaks emit noise in the form of Rossiter-like cavity noise across the slat span. Himeno et al. [88] have shown that the frequencies of the Rossiter modes vary based on the slat recirculation. The subsequent sections will clarify the mechanisms contributing to the amplified noise and the alterations in peak frequencies.

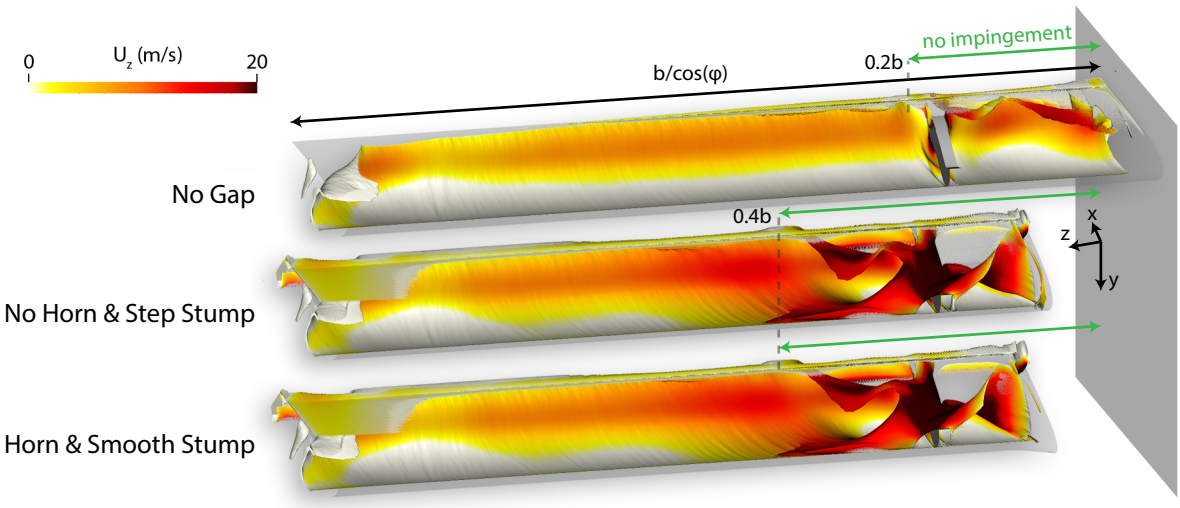

Figure 8.7: Comparison of the slat cove wake through ($C_{p,\,total} = 0$)-isosurface coloured by the outboard spanwise velocity in red using an averaging period of 0.33 s, resulting in roughly 130 slat flow-throughs at a slat-based Strouhal number of $St_{c_s} = 8.3 \cdot 10^{-3}$.

8.3.1. Slat cove flow dynamics

The turbulent structures in the slat cove and their flow direction play an important role in the noise radiation of the research set-up. Figure 8.7 displays the iso-surface of ambient total pressure, visualising the extent of the wake, coloured by the spanwise velocity inside the slat cove. The slat is shown partially transparent. The research set-up incorporates a sweep angle ϕ, a slat track, and a sideplate-slat gap, resulting in large-scale 3D flow phenomena inside the slat cove. The shape of the wake indicates that the introduction of the sideplate-slat gap significantly disrupts the coherency of the slat recirculation flow across a substantial portion of the slat span. Air is transported through the gap to inside the slat cove and accelerates over the slat track. This flow pattern enhances the turbulence just outboard of the slat track, as demonstrated by figure 8.4 region B. Himeno et al. [88] explain that for 2.5D slat geometries, acoustic waves stemming from the slat trailing edge impingement trigger the formation of new vortices at the cusp, forming a flow-acoustic interaction that selects certain frequencies, resulting in narrow-band resonance. In this set-up, however, the slat mean shear does not impinge near the trailing edge until $z = 0.4b$ for the geometries with a sideplate-slat gap. Additionally, as seen from the spanwise velocity colouring, the slat cove recirculation is altered across the entire span. Hence, although the pressure fluctuation intensity is increased aft of the slat track by the introduction of a sideplate-slat gap, canonical impingement of the mean shear line near the trailing edge does not occur until well into the slat span, possibly decreasing the narrow-band resonance.

8.3.2. Narrow-band resonance extent

The impact of the alteration of the slat cove's recirculation bubble on the Rossiter-like modes can be visualised using an FW-H-based noise source visualisation technique introduced by Casalino et al. [39]. This technique computes the contribution of each surface element to the far-field noise at a specific location using FW-H-based noise propagation. The method distinguishes between elements that contribute constructively (in-phase) and destructively (out-of-phase) per frequency band. Consequently, it can also describe the resonance of different source locations per frequency, as resonating elements are coherent. Therefore, an FW-H-based noise visualisation focused around a narrow-band peak such as the St_{c_s} $2.1-2.9$ band, will provide insights into the slat span-based extent of resonance of the tonal noise. Figure 8.8 visualises the Coherent Output Power (COP) on the left, i.e., all noise source mechanisms, regardless of whether they contribute in or out of phase to the far-field noise at the specified microphone location, the Coherent Power (CP), i.e. in phase contributions, in the middle, and the Destructive Power (DP),

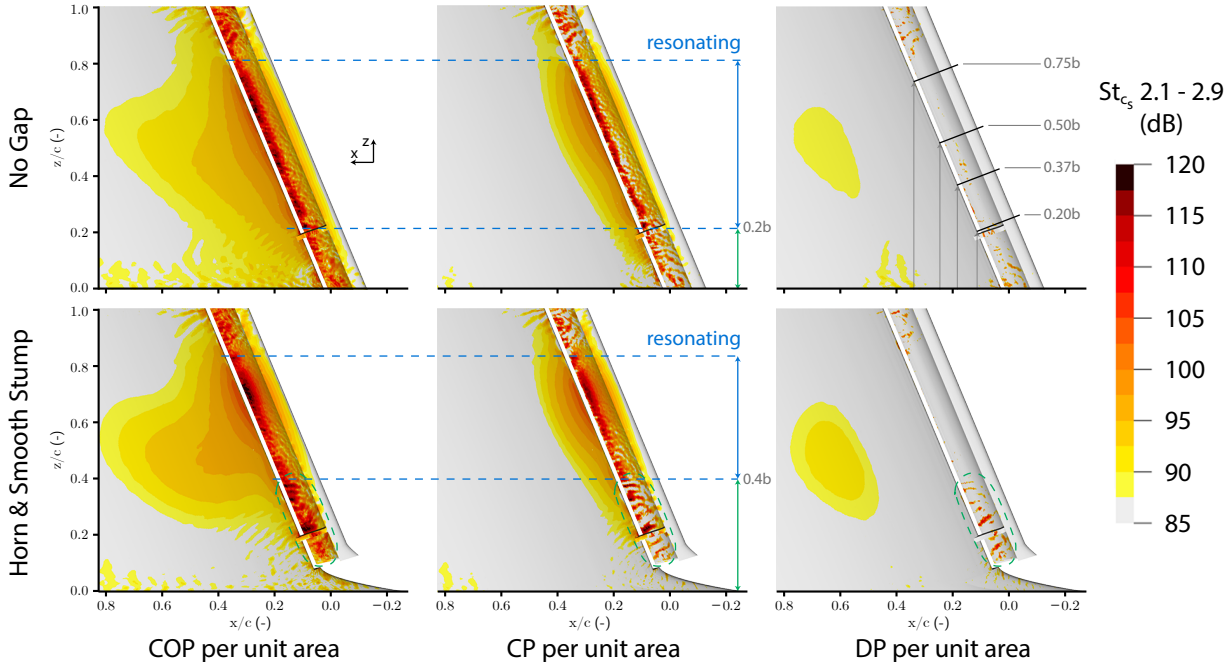

Figure 8.8: Coherent Output Power (COP), Constructive Power (CP), and Destructive Power (DP) comparison of a geometry with and without sideplate-slat gap between St_{c_s} $2.1 - 2.9$.

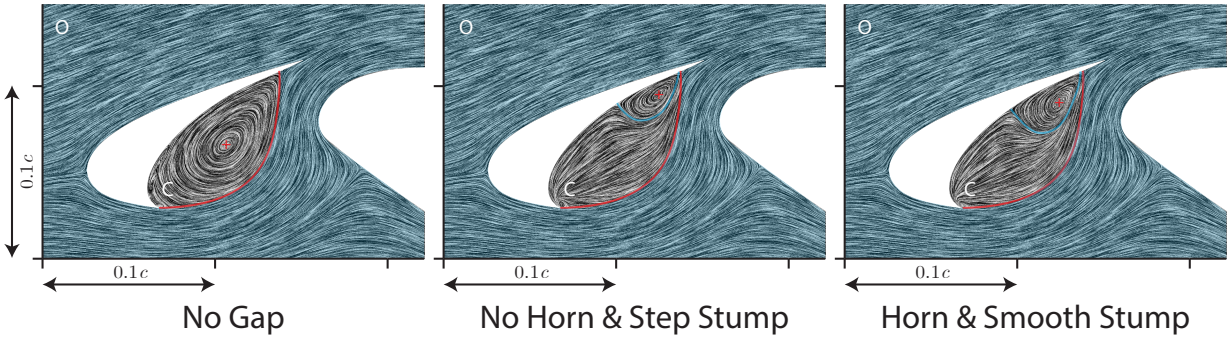

Figure 8.9: Flow topology through Line Integral Convolution (LIC) at $z = 0.75b$ (figure 8.8) averaged for 0.33 s. The centre of the recirculation is indicated with '+' symbol. The main shear line is shown in red, and optionally a secondary shear layer is shown in blue.

i.e. out-of-phase contributions, on the right. The slat chord trailing edge is the largest contributor to the total noise at this frequency band, as seen from the COP and CP. The resonating elements are visible in the CP visualisation. As suggested by the slat cove wake, the resonating area of the research model is considerably smaller when a sideplate-slat gap is present, in this case, the Horn & Smooth Stump geometry. The extent of the resonance is perhaps most clearly visible on the main element itself, which shows the acoustic reflections from the slat trailing edge. The resonance is broken by the additional high-intensity sources which show up alternatingly in- (CP) and out-of-phase (DP) (encircled in figure 8.8 in the Horn & Smooth Stump geometry). Casalino et al. [39] explain that such sources are ineffective at radiating noise to the far-field. The broken resonance is believed to be the primary mechanism causing the decrease in noise power of the narrow-band peaks when a sideplate-slat gap is present, as indicated in table 8.1.

8.3.3. Narrow-band centre frequencies

The introduction of a sideplate-slat gap appears to marginally reduce the frequency of each Rossiter-like mode (figure 8.1). The frequencies of the narrow-band peaks are only contingent on the shedding within the slat cove if Strouhal scaling is used. Figure 8.9 visualises the impact of the sideplate-slat gap on the slat cove recirculation through a Line Integral Convolution (LIC). The flow topology was captured on a plane perpendicular to the slat span at $z = 0.75b$ where all geometries were resonating, as per figure 8.8. The flow topologies outside the cove (O, in figure 8.9) exhibit similar patterns, whereas the flow topology within the cove (C, in figure 8.9) have undergone a stark alteration. The mean shear line and trailing edge impingement point are nearly identical in all cases. However, the NH and H geometries have an additional smaller recirculation area and an altered centre of the recirculation bubble. This was already suspected from the recirculation line depicted in figure 7.3. Frequency prediction models from both Terracol et al. [74] and Souza et al. [87] (the latter is given by eq. (8.1)) relate the centre of the narrow-band peaks to the acoustic path length L_a ($\sim$ straight line between impingement location and the slat cusp), the vortex path length L_v ($\sim$ mean shear line), and the mean vortex convective velocity V. Moreover, the work from Himeno et al. [88] indicates that an additional circulation bubble slows the mean vortex convective velocity, resulting in lower centre frequencies for the narrow-band peaks. Therefore, a retarded vortex convective velocity V is suspected to be the principal reason for the lower frequency of the narrow-band peaks when a sideplate-slat gap is introduced.

$$St_n = \left(n + \frac{1}{4}\right) \frac{c_s}{U_\infty} \frac{V c_{sos}}{c_{sos} L_v + V L_a} \tag{8.1}$$

The frequency of periodically shedding turbulent structures within the cove can be quantified using a Spectral Proper Orthogonal Decomposition (SPOD) analysis. The flow separation at the slat cusp gives rise to turbulent structures of varying sizes and consequently, different frequencies. Owing to the resonance mechanism between the acoustic radiation at the slat trailing edge, certain turbulent structures with a specific frequency are selected more frequently. In an SPOD analysis, if the first mode in a certain frequency band possesses a high energy ratio compared to the total energy, it implies that the turbulent structures are shed very consistently at that frequency band. Figure 8.10 demonstrates that at the narrow-band peak frequencies, the energy ratio of the first SPOD mode is significant at $z = 0.75b$. Moreover, the shedding frequencies in the No Gap configuration are slightly higher than those in the geometries with a

sideplate-slat gap, aligning with the noise spectra. Hence, a likely slower convective velocity reduces the frequency of the acoustic radiation which selects aerodynamic structures of a lower frequency, closing the resonance loop. Another interesting observation is that the energy ratio of the peaks in the “No Gap” geometry do not reach as high as the two configurations with the gap at $z = 0.75b$. Figure 8.8 does not imply that the noise intensity at a given spanwise slice is lower when the sideplate-slat gap is closed, nor does the far-field noise radiation from the microphone probe (figure 8.1). Therefore, this might merely be a coincidental result of the precise location of the spanwise plane used for the SPOD analysis. At $z = 0.37b$ and $z = 0.50b$ the geometries with a sideplate-slat gap do not show a high energy content in the turbulent structures surrounding the narrow-band peaks, reinforcing the evidence for lack of acoustic-flow resonance at those locations. At $z = 0.37b$ the geometries with a sideplate-slat gap show a large energy peak at lower frequencies, which is likely related to the wake structure shown in figure 8.7.

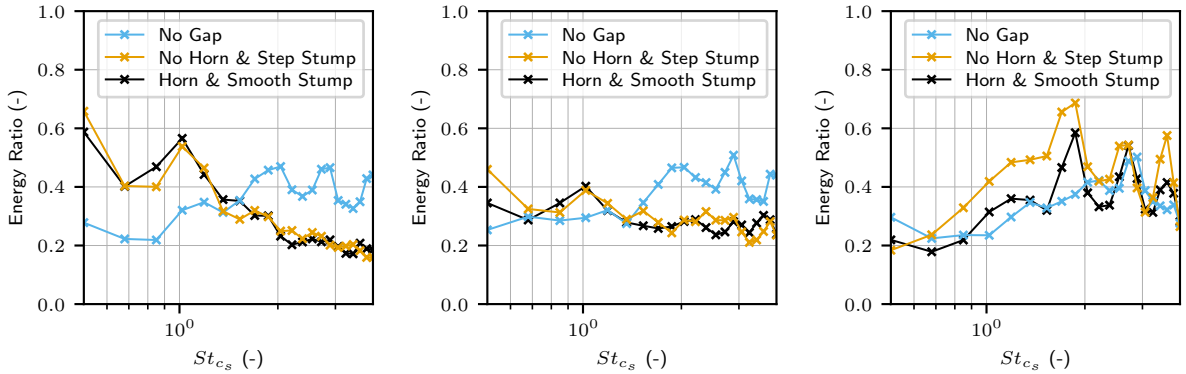

(a) $z = 0.37b$ **(b)** $z = 0.50b$ **(c)** $z = 0.75b$

Figure 8.10: Energy content of the first SPOD mode compared to the total energy at three planes defined in figure 8.8.

In conclusion, given the research model’s loading and flow conditions, the introduction of a sideplate-slat gap reduces the magnitude of the narrow-band peaks, because the slat side-edge wake starts interfering with the flow-acoustic resonance mechanism. Additionally, the gap introduces a second recirculation area which likely retards the convective velocity of the shed turbulent structures, therefore lowering the acoustic radiation frequency and hence the narrow-band peak frequencies.

8.4. Statistical significance of narrow-band peak power differences

The statistical significance of the low-frequency peak noise is analysed below, as the sampling duration of all noise measurements was limited to a relatively short 0.33 s. The evaluation of the mean power of the narrow-band peaks and their confidence intervals provide insights into the statistical significance of the noise differences between the model variants. The full pressure-time signal (no Welch blocks) for all variants was band-passed filtered using a Butterworth filter around the three analysed narrow-band peak bands St_{c_s} $(1.40, 2.24)$, $(2.38, 3.22)$, and $(3.35, 4.19)$. The SPL of each band was calculated by taking the mean of the absolute value of the band-passed signal’s Hilbert envelope and converting it to dB using a reference pressure of $p_{\text{ref}} = 2 \cdot 10^{-5}$ Pa. Figure 8.11 displays the band-passed filtered pressure-time signals for the ‘H’ geometry. The amplitude of the Hilbert transform is displayed by the black line. The confidence interval of the mean power of the amplitude can be calculated using

$$CI = \mu + z_0 \cdot \frac{\sigma}{\sqrt{n}}$$

where μ is the mean of the amplitude, z_0 the z-score which depends on the desired confidence interval, e.g. $z_0 = 1.960$ for an interval of 95%, σ is the standard deviation, and n is the number of samples, which is the number of peaks present per band-passed signal in figure 8.11.

Figure 8.12 displays the SPL of the narrow-band peaks and their respective 95% confidence intervals for each model variant. The mean magnitudes do not exactly correspond to the results from section 8.1, as there Welch’s signal processing approach was used. The width of the confidence interval decreases for

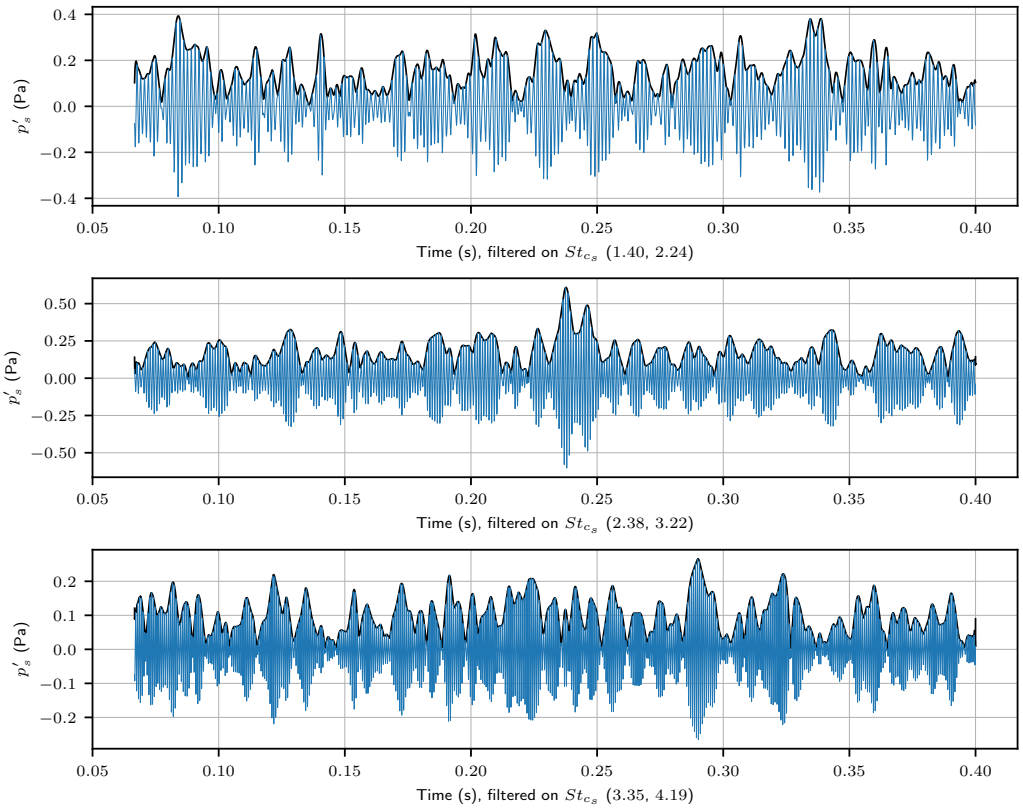

Figure 8.11: Band-passed filtered pressure-time signal around the Strouhal number bands St_{c_s} (1.40, 2.24), (2.38, 3.22), and (3.35, 4.19) for the 'Horn & Smooth Stump' geometry. Hilbert's envelope is visualised by the black line.

higher frequencies, as more instances of the frequencies are captured within a sampling period. Within a 95% confidence level, the first narrow-band peak shows a statistically similar noise power across all variants. The 'NH' variant shows a reduction in noise power compared to the 'NG' and 'H' variants for the second peak. At the third peak, both the 'NH' and 'H' variants show a noise reduction. Although the magnitude of these reductions is not yet very pronounced in this study, they are statistically significant. This provides confidence in exploiting this noise-reducing phenomenon in future aero-structural design optimisations.

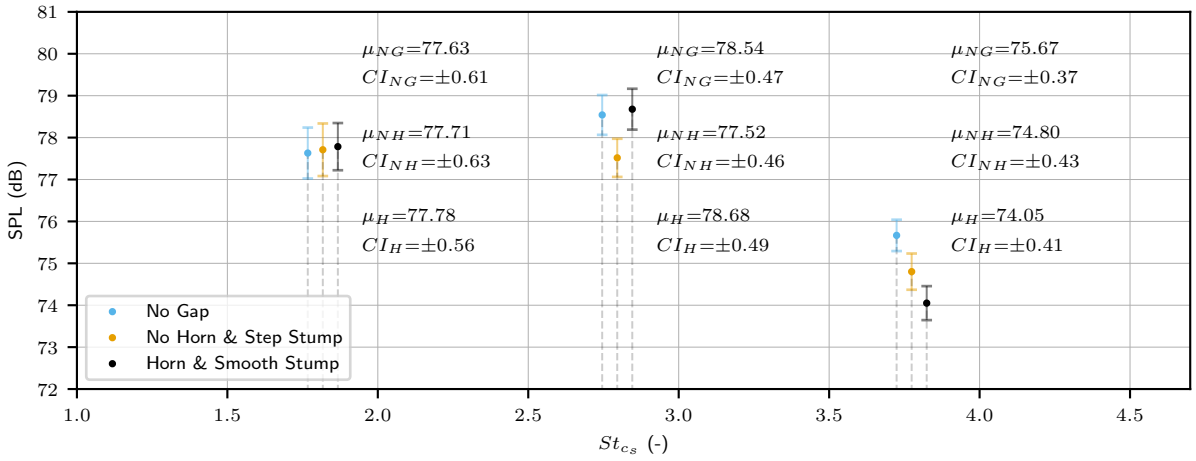

Figure 8.12: Mean SPL of the Strouhal number bands St_{c_s} (1.40, 2.24), (2.38, 3.22), and (3.35, 4.19), and their respective 95% confidence interval of the mean for all model variants.

III

Concluding remarks

This part presents the concluding remarks on the study on fuselage-wing-slat junction noise. The conclusions to the thesis are provided in chapter 9. Following this, chapter 10 provides recommendations for future research which can improve on the methodology, remove remaining uncertainties, and further the understanding of the fuselage-wing-slat junction noise and noise mechanism.

9

Conclusions

Airframe noise is becoming a prominent noise source during approach, largely due to the rise in aircraft equipped with quieter high-bypass turbofan engines. In recent commercial aircraft, airframe noise, mainly originating from landing gears and high-lift devices, often surpasses the jet exhaust noise [10, 9]. Noise source localisation results from flyover measurements have identified the inboard slat [12], and the junction between the slat, wing, and fuselage [13, 14] as significant localised noise sources across the frequency spectrum. However, it remains unclear how to design a fuselage-wing-slat junction optimised for loading and low noise. This study aimed to describe the relation between the aero-structural design of the fuselage-wing-slat junction and its aeroacoustic footprint for an aircraft in approach configuration. To properly describe the aeroacoustic characteristics of a fuselage-wing-slat junction, the first research question pertains to the creation of a suitable scaled research set-up.

RQ 1

*What is a suitable **scaled research model** that represents the aeroacoustic characteristics of a full-scale fuselage-wing-slat junction while being compatible with open-jet wind tunnel experiments?*

The creation of a suitable scaled research model requires describing the prevalent large- and small-scale turbulent structures in the region. The slat side-edge creates two coherent vortices. The first is a roll-up vortex at the slat chord trailing edge scaling with the slat side-edge length, hence also the slat horn - a hornlike protrusion on the slat-side edge which morphs the wing and fuselage when the slat is retracted, and the slat loading. The second is a vortex stemming from the slat cusp moving inside the slat cove by the spanwise cross-flow. Additionally, air inside the fuselage-slat gap separates from the slat side-edge and moves in spanwise to the slat cove. The slat track position influences this separation zone. Lastly, a horseshoe vortex is created at the fuselage-wing-slat junction, and at the slat stump-wing junction. These aerodynamic features should be incorporated into a model based on a widely researched, openly available airfoil cross-section in the context of slat noise, to improve reproduciblity and the possibilities for follow-up studies.

This study's research set-up was designed for open-jet numerical simulations using the commercial Lattice Boltzmann Method (LBM) based CFD solver PowerFLOW, with compatibility for experimental open-jet wind tunnel validation studies at the TU Delft's Anechoic A-tunnel. Three variations of a two-sideplate research set-up were created based on a slat-and-main-wing modified 30P30N airfoil cross-section. The loading on the slat and the leading edge of the main element were kept similar to the three-element 30P30N cross-section to achieve similar vortex structures as an in-flight 30P30N-based wing at an approach angle of attack of 4°. To isolate specific junction aeroacoustic effects three variants were created. A 'No Gap' (NG) geometry that connects the slat to both sideplates; a 'No Horn & Step Stump' (NH) geometry that has a simplified slat side-edge and slat stump, a feature that blends the main wing with the fuselage; and a 'Horn & Smooth Stump' (H) geometry, which incorporates a slat horn, and a slat stump, modelled after the Airbus A320. For all three variations, the relative size and positions of the fuselage boundary layer, the slat track, the slat side-edge, and other junction surfaces were modelled after the Airbus A320 as well.

This implementation specifically targets similarity to the Airbus A320, which is known to elicit the vortex structures described above. Similarity to the A320, however, is not strictly necessary, as long as the model generates the desired vortex structures.

The second research question addresses the relation between the aero-structural design of the scaled fuselage-wing-slat junction and its aeroacoustic footprint. Moreover, the answer to the question will help contextualise the characteristics of the scaled model compared to previous scaled junction studies, full-Reynolds number studies, and flyover noise measurements of a fuselage-wing-slat junction. The question is stated as follows:

RQ 2

*What are the **aeroacoustic characteristics** of the scaled fuselage-wing-slat junction model, and how do these characteristics compare to previous research findings?*

The noise spectrum of the scaled fuselage-wing-slat junction follows a similar Sound Pressure Level (SPL) to frequency trend as full-Reynolds scale slat measurements [86] when the frequency spectra are non-dimensionalised through Strouhal scaling. Compared to flyover data spectra from deconvoluted beamforming methods [14] the spectra converge for slat chord-based Strouhal numbers above 8 and deviate below that. The flyover data likely under-represents the low-frequency noise due to limitations of beamforming integration due to Rayleigh's criterion [89].

Surface pressure fluctuation intensity results in the slat cove hint at a similar slat cove wake structure compared to earlier scaled junction research from Ribeiro et al. [34], even though their slat is vastly more loaded. Additionally, the sizes of the turbulent flow structures in the slat cove are similar to earlier research from Murayama et al. [35], which provides confidence in the set-up and discretisation of this study's simulation.

Excess high-frequency noise in the junction was not measured in this study, in contrast to findings from Ahlefeldt [86]. This discrepancy is related to the lack of significant impingement from slat side-edge roll-up vortices, and fuselage-wing junction horseshoe vortices. The current set-up features a minimally loaded slat, which generates just a small vortex. Additionally, even though the study aimed to simulate horseshoe vortices in the fuselage-wing junction by creating a thick sideplate boundary layer, no significant horseshoe vortices were captured in the simulation.

This study showed that the spanwise extent of the slat narrow-band peak resonance mechanism can be decreased by modifying the slat cove wake shape. The introduction of a sideplate-slat gap increases the slat cove spanwise velocity which partially prevents slat-cusp-to-slat-trailing-edge impingement, without impacting the loading of the model. The slat wake shape is further modified by the inboard slat track which constricts the flow in the slat cove and accelerates the cross-flow. This acceleration further modifies the wake shape, preventing the resonance-inducing slat-cusp-to-slat-trailing-edge impingement further. Hence, the mechanism depends on the shape and relative orientation of the slat side-edge, slat cusp, and the slat track. These findings show that holistic aero-structure and aeroacoustic design can help reduce the junction noise radiation, without impacting the aircraft's loading.

10

Recommendations for future research

The current study has characterised a mechanism which decreases the slat narrow-band peak noise magnitude by altering the large-scale 3D slat cove flow structure. However, several uncertainties remain. This chapter details recommendations for future studies which can improve on this study's methodology, tackle uncertainties, and further the scientific understanding of the fuselage-wing-slat junction noise mechanism and noise attenuation. For more involved recommendations, visual supports are included to aid in understanding them.

Investigating large-scale horseshoe vortex generation in LBM simulations
The research set-up behaved largely as intended, apart from the creation of a large, strong horseshoe vortex. It remains uncertain whether the absence of a strong noise radiating horseshoe vortex was a consequence of the simulation or the geometrical research set-up. The boundary layer on the sideplate was thicker than desired, which could be due to either the trip being positioned too far away or an insufficient number of cells within the boundary layer. Specifically, the achieved boundary layer was 6.8 cm, whereas the target was 5 cm. This thick boundary layer might have prevented the formation of a strong horseshoe vortex as it interacted with the slat horn. Results from Ahlefeldt [86] suggest that horseshoe vortices are a source of high-frequency noise. To better understand the prerequisites for generating a horseshoe vortex in the LBM simulations, a new test domain should be created. This domain should involve boundary layer flow over a flat plate encountering a perpendicular cylinder, serving as a test bed to describe the requirements for correctly capturing horseshoe vortices in future fuselage-wing-slat junction LBM simulations.

Comparison of noise radiation for a similar set-up, excluding a no-slip nozzle
This study used a no-slip nozzle to both emulate the expected behaviour in the TU Delft A-tunnel, as well as create a thick boundary layer to mimic the relative boundary layer thickness in the junction of a commercial aircraft. A comparison between a slip nozzle and a no-slip nozzle in terms of noise radiation and flow structures can help describe which part of the noise generation mechanism can accurately be modelled and predicted without the usage of a more expensive no-slip nozzle. For low-frequency slat cove junction effects, a no-slip nozzle might not be necessary, potentially reducing CPU hours by roughly 16% for the medium refined simulations [1].

Describing the effect of large geometrical angles of attack for open-jet nozzle fuselage-wing-slat junction research
The final geometrical configuration presented some challenges from its high angle of attack. Two AoA corrections were performed, leading to a geometrical AoA of $26.2°$, which causes blockage effects in open-jet nozzles. This blockage is undesirable as it can affect the flow characteristics and the similarity of the simulation to non-modelled conditions. Additionally, the high AoA caused the slat stump to orient slightly upwards rather than solely forward, differing from real aircraft configurations. Although the slat and leading-edge main element loading in the current set-up were deemed viable, future studies can aim to achieve similar slat loading without requiring extensive AoA corrections. Removing the restriction on nozzle size after validating current results with experimental measurements can already resolve the blockage issue for numerical simulations.

[1] Assuming the offset layers scale with area, the slip nozzle reduces the refined area by 65% for the VR5 and VR6 voxel counts, equating to roughly 16% reduction in fine-equivalent (VR8) voxels. CPUh scale with the number of fine-equivalent voxels.

Validation of the numerical findings on the aeroacoustic characteristics of a scaled fuselage-wing-slat junction model through open-jet wind tunnel experiments at the TU Delft A-tunnel
The research set-up has been designed with validation at the TU Delft A-tunnel in mind. The three model variants could be based on a single modifiable structure. The variations can then be tested by swapping interchangeable slat side-edge, and slat stump shapes. For improved modularity the slat track, and its position, could be modifiable as well. Pressure tabs should be installed on the midsection of the model to validate the pressure distribution on the slat and main element. Validation of the noise radiation spectrum for all three variants can be performed by a single microphone. FW-H analyses are not possible in experimental studies. Hence, it is recommended to reduce spurious noise radiation from sources not present in a real aircraft, e.g. near the aft sideplate. Validating the slat cove wake shape and spanwise slat resonance extent is more involved. This likely requires placing PIV planes along multiple span locations in the slat cove. An SPOD analysis or a band-pass filter analysis can show which of these planes generates turbulent structures within the narrow-band peak ranges periodically and is hence contributing to resonance.

Experimental quantification of high-frequency noise in the scaled fuselage-wing-slat junction
The model variants with a sideplate-slat gap in this numerical study did not produce excess high-frequency noise compared to the 'No Gap' variant. However, the simulation did not capture a strong horseshoe vortex either. Instead of first characterising the prerequisites for LBM horseshoe vortices, experimental measurements can quantify whether this is a limitation of the current simulation, or if the geometrical model does not excite the creation of horseshoe vortices which generate the excess noise. However, this does require the creation of a physical fuselage-wing-slat junction model first.

Quantification of the effect of slat loading on the noise spectrum of a scaled fuselage-wing-slat junction model.
Either through numerical, or experimental studies the effect of slat loading on the noise spectrum should be addressed, as it was hypothesised that a higher slat loading increases fuselage-wing-slat junction noise. This can be done by increasing the angle of attack of the entire set-up, testing a different cross-section with a more loaded slat, or changing the angle of the slat separately from the main element.

Quantification of the effect of slat cusp tripping for the fuselage-wing-slat junction model
In this study, the slat and main element were not tripped, following common practices for the 30P30N set-up. The effect of slat cusp boundary layer tripping remains unresolved in literature. Dobrzynski et al. [49] describes an attenuation in narrow-band peak noise, whereas Murayama et al. [77] measures an increase in narrow-band peak noise by tripping the slat cusp flow. Investigating the turbulence in the slat cusp boundary layer, and the effect of the slat cusp boundary layer on slat narrow-band peak noise will help quantify to what extent narrow-band peak noise is present in commercial aircraft, and hence to what extent noise attenuation efforts decrease the overall aircraft noise.

Investigation into the slat narrow-band peak resonance mechanism for slat coves including cross-flow
The narrow-band peak resonance mechanism under cross-flow conditions has never been described in literature. Figure 10.1 provides a schematic representation of the convective and acoustic velocity paths for the slat-cusp-to-trailing-edge resonance mechanism. Souza et al. [87] and Terracol et al. [74] postulate that the centre frequencies of the narrow-band resonance peaks depend on both the mean vortex shedding path and the acoustic path, as well as their velocities. However, as seen from figure 10.1, for 3D geometries (solid lines), the vortex convective velocity path is considerably different from the canonical 2D case (dashed lines). There is no literature regarding the influence of cross-flow on either the centre frequency or the magnitude of the narrow-band peaks. Hence, it remains uncertain whether, for the 3D case in figure 10.1, the acoustic radiation excites the creation of resonating turbulent structures at other points on the slat cusp, apart from the location on the cusp closest to the acoustic radiation point. Investigating this mechanism in realistic aircraft conditions will provide valuable insights for future noise reduction solutions.

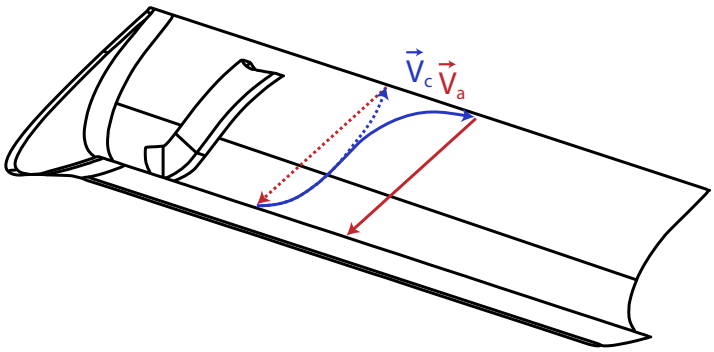

Figure 10.1: Schematic representation of the convective velocity V_c path and acoustic velocity V_a path for a 3D (swept, including slat track) slat cove geometry. The solid lines represent the 3D velocity paths, whereas the dotted lines represent the regular 2D velocity paths.

Optimisation of the fuselage-wing-slat junction aero-structure to minimise its aeroacoustic footprint while retaining its loading characteristics

The current study has characterised a noise reduction method for the slat narrow-band peaks by altering large-scale 3D slat cove flow structures. However, a complete relation between the aero-structural design of the fuselage-wing-slat junction and its aeroacoustic footprint has not yet been conclusively established. The recommendations provided earlier will help to properly describe the relation. This final recommendation is based on the hypothesised holistic noise generation mechanism of a fuselage-wing-slat junction. Therefore, first, a full overview of the author's current hypothesis will be provided, after which a to-be-investigated noise reduction strategy is provided. This hypothesis must be proven before investigating the proposed geometrical optimisations.

Before discussing the hypothesised noise mechanism of the fuselage-wing-slat junction, the impact of slat tracks, briefly mentioned in section 7.3, is further examined. Figure 10.2 illustrates the noise difference between an optimised slat track and a basic non-optimised track, as studied by Van Bokhorst et al. [61]. The measurements were conducted on a research set-up that included a sweep of $30°$, leading to some cross-flow, but without a sideplate-slat gap. The optimised track design features a tilted fairing, minimising the separation aft (in the cross-flow direction) of the slat track near the main wing. Compared to a basic slat track, the reduced separation significantly attenuates the noise above $St_{c_s} = 6$. Van Bokhorst et al. [61] suggest that this is likely due to less intense impingement on the slat trailing edge and main element leading edge by small-scale turbulent structures. However, below $St_{c_s} = 6$, the noise from the slat increases, particularly at the narrow-band peaks. This study showed that this increase could be related to an extended slat-span resonance resulting from a smaller separation zone, as detailed in chapter 8.

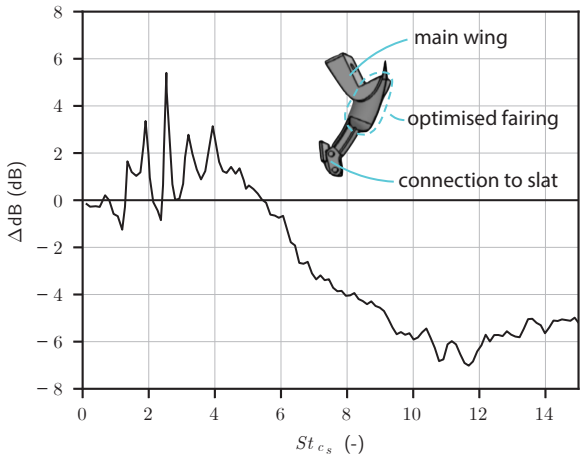

Figure 10.2: Power integrated spectrum of a slat cove surrounding a noise optimised slat track (upper right) compared to an integrated spectrum with a basic slat track, adapted from Van Bokhorst et al. [61].

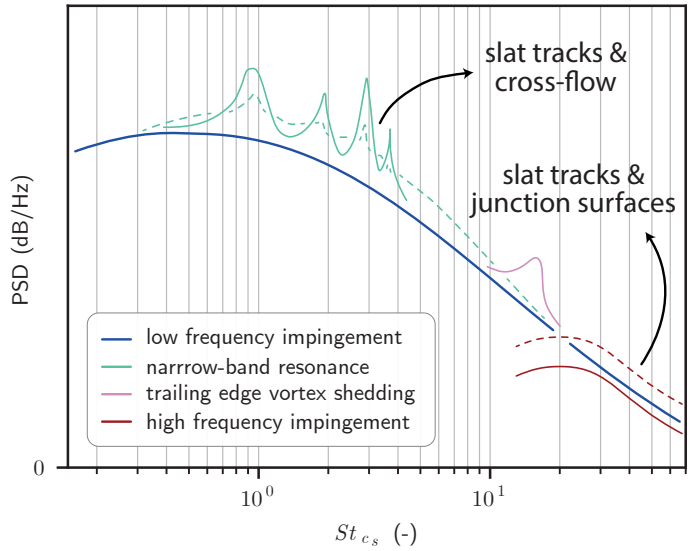

Figure 10.3: Spectrum of hypothesised junction noise mechanisms. Solid lines represent the traditional slat noise pattern and dashed lines represent the influence of components in the fuselage-wing-slat junction.

Canonical slat cove noise is key to understanding the hypothesised junction noise mechanism. Figure 10.3 presents a customised slat cove noise spectrum for the fuselage-wing-slat junction (modified from figure 4.6). This spectrum includes four distinct noise mechanisms: a low-frequency broadband component, narrow-band resonance, trailing edge vortex shedding, and high-frequency impingement. Additionally, two influencing factors are hypothesised. The first, *(1)*, is the presence of slat tracks, which work in conjunction with cross-flow in the slat cove. The second, *(2)*, is the presence of all 'upstream' surfaces, which include the slat track and junction surfaces such as the slat side-edge, slat horn, slat stump, and the fuselage. These two features are hypothesised to alter the noise spectrum from a canonical slat cove (solid lines in figure 10.3) to the fuselage-wing-slat junction spectrum (dashed lines).

Factor *(1)* acknowledges that slat tracks generally amplify noise due to flow separation. However, depending on the cross-flow and the wake shape aft of the slat track (in the spanwise direction), slat tracks can also disrupt the spanwise extent of the narrow-band resonance mechanism, reducing the narrow-band peak magnitude and altering the peak frequencies. Factor *(2)* arises from small-scale turbulent structures emerging in the junction and near the track due to separation, which impinge near the junction and track.

The hypothesised influence of these two features can be used to design an optimised fuselage-wing-slat junction, without impacting the aerodynamic loading. The main goal of the geometrical alterations near the junction should be two-fold. Firstly, to accelerate the cross-flow in the slat cove, preventing canonical slat-cusp-to-slat-trailing-edge impingement, reducing the resonance extent. Secondly, minimising separation

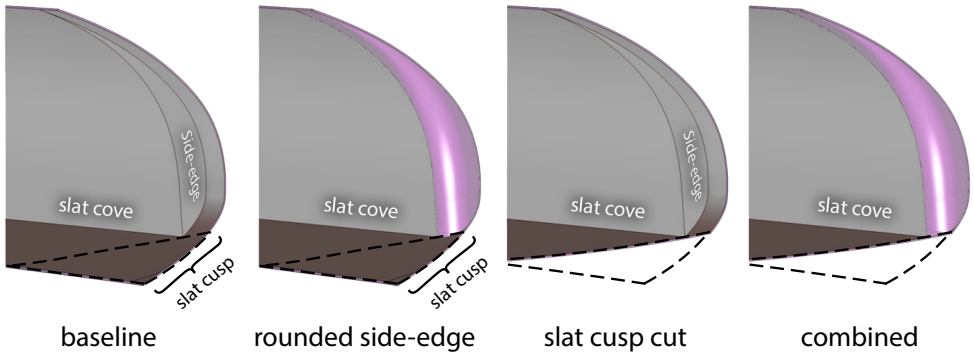

Figure 10.4: Proposed slat side-edge modifications, adapted from Murayama et al. [35]

at the slat side-edge and slat tracks to minimise the production of small-scale turbulent structures. Both of these goals involve alterations of the slat side-edge and the slat track design, and their interplay. These modifications should be tailor-made depending on the aircraft they are applied to. Some general design alteration strategies are proposed here.

The side-edge modifications proposed by Murayama et al. [35], illustrated in figure 10.4, introduce a rounded slat side-edge and a 'cut' slat cusp which serve to reduce separation and hence impingement of small-scale turbulent structures on the slat and main wing. Additionally, the author suspects both alterations increase the cross-flow velocity. Developing a slat side-edge that promotes cross-flow, minimises separation, and can be integrated into an actual aircraft is an interesting subject for future studies.

The second strategy revolves around the slat track. Slat track optimisations for specific slat cove flows which minimise separations have already been successfully tested by Van Bokhorst et al. [61]. The author suggests increasing the (fairing) thickness of the slat track near its connection point to the main wing and near the slat trailing edge to improve their low-frequency performance, as illustrated in figure 10.5. This constricts and hence accelerates the cross-flow, potentially also reducing the spanwise extent of the narrow-band resonance. Placing an additional flow accelerating/constricting slat track that has limited shedding might actually be beneficial to reduce the low-frequency peaks if it has limited influence on the existing noise intensities. Both of these alterations are interesting subjects for future research.

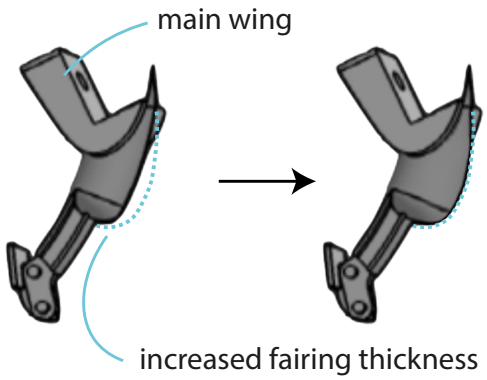

Figure 10.5: Proposed slat track alteration. Slat track visual taken from Van Bokhorst et al. [61]

While the current findings and hypotheses concerning fuselage-wing-slat junction noise generation and attenuation mechanisms provide a promising direction for future research, uncertainties need to be resolved first. These include validating the noise generation mechanisms, understanding the effects of slat loading on high-frequency noise, and investigating the narrow-band peak resonance mechanism in 3D geometries under cross-flow conditions, as described by earlier recommendations. Addressing these uncertainties will enhance the understanding of aeroacoustic phenomena in fuselage-wing-slat junctions and improve noise reduction strategies.

References

Articles & Reports

[2] IATA. *Global Outlook for Air Transport - A local sweet spot*. Tech. rep. All Rights Reserved. Montreal, Quebec: International Air Transport Association, Dec. 2023.

[3] A. Filippone. “Aircraft noise prediction”. en. In: *Progress in Aerospace Sciences* 68 (July 2014), pp. 27–63.

[8] W. Graham, C. Hall, and M. Vera Morales. “The potential of future aircraft technology for noise and pollutant emissions reduction”. en. In: *Transport Policy* 34 (July 2014), pp. 36–51.

[9] C. A. Hall. “Low noise engine design for the Silent Aircraft Initiative”. en. In: *The Aeronautical Journal* 113.1147 (Sept. 2009), pp. 599–607.

[10] W. Dobrzynski. “Almost 40 Years of Airframe Noise Research: What Did We Achieve?” en. In: *Journal of Aircraft* 47.2 (Mar. 2010), pp. 353–367.

[11] Y. Li, X. Wang, and D. Zhang. “Control strategies for aircraft airframe noise reduction”. In: *Chinese Journal of Aeronautics* 26.2 (Apr. 2013), pp. 249–260.

[12] J. Piet, G. Elias, and P. Lebigot. “Localization of acoustic source from a landing aircraft with a microphone array”. en. In: *5th AIAA/CEAS Aeroacoustics Conference and Exhibit*. Bellevue,WA,U.S.A.: American Institute of Aeronautics and Astronautics, May 1999.

[13] P. Sijtsma and R. Stoker. “Determination of Absolute Contributions of Aircraft Noise Components Using Fly-over Array Measurements”. en. In: *10th AIAA/CEAS Aeroacoustics Conference*. Manchester, GREAT BRITAIN: American Institute of Aeronautics and Astronautics, May 2004.

[14] H. Siller, W. Hage, and T. Schumacher. “Source localisation on aircraft in flight - new measurements with the DLR research aircraft Airbus 320 ATRA”. de. In: *7th Berlin Beamforming Conference (BeBeC)*. Berlin, Germany, 2018.

[16] J. E. Penner et al. *Aviation and the Global Atmosphere*. Tech. rep. Cambridge: IPCC, 1999.

[17] D. Lee et al. “The contribution of global aviation to anthropogenic climate forcing for 2000 to 2018”. en. In: *Atmospheric Environment* 244 (Jan. 2021), p. 117834.

[19] G. Schrauf. “Large-Scale Laminar Flow Tests Evaluated with Linear Stability Theory”. en. In: *Journal of Aircraft* 41.2 (Mar. 2004), pp. 224–230.

[20] G. Schrauf. “Status and perspectives of laminar flow”. en. In: *The Aeronautical Journal* 109.1102 (Dec. 2005), pp. 639–644.

[21] Y. Shi, X. Lan, and T. Yang. “Hybrid Laminar Flow Control Optimizations for Infinite Swept Wings”. en. In: *International Journal of Aerospace Engineering* 2023 (May 2023). Ed. by R. Pecora, pp. 1–33.

[23] C.-L. Navier. “Sur les lois des mouvements des fluide”. In: *Annales de Chimie et de Physique* 19 (1822), pp. 244–260.

[25] M. J. Lighthill. “On sound generated aerodynamically I. General theory”. en. In: *Proceedings of the Royal Society of London. Series A. Mathematical and Physical Sciences* 211.1107 (Mar. 1952), pp. 564–587.

[26] M. J. Lighthill. “On sound generated aerodynamically II. Turbulence as a source of sound”. en. In: *Proceedings of the Royal Society of London. Series A. Mathematical and Physical Sciences* 222.1148 (Feb. 1954), pp. 1–32.

[30] J. E. Ffowcs-Williams and L. H. Hall. “Aerodynamic sound generation by turbulent flow in the vicinity of a scattering half plane”. en. In: *Journal of Fluid Mechanics* 40.4 (Mar. 1970). Publisher: Cambridge University Press, pp. 657–670.

[31] D. A. Russell, J. P. Titlow, and Y.-J. Bemmen. “Acoustic monopoles, dipoles, and quadrupoles: An experiment revisited”. In: *American Journal of Physics* 67.8 (Aug. 1999), pp. 660–664.

[33] S. Marié, D. Ricot, and P. Sagaut. “Comparison between lattice Boltzmann method and Navier–Stokes high order schemes for computational aeroacoustics”. en. In: *Journal of Computational Physics* 228.4 (Mar. 2009), pp. 1056–1070.

[34] A. F. Ribeiro et al. “Effect of Slat Tracks and Inboard Slat Tip Geometry on Airframe Noise”. en. In: *28th AIAA/CEAS Aeroacoustics 2022 Conference*. Southampton, UK: American Institute of Aeronautics and Astronautics, June 2022.

[35] M. Murayama et al. “Aircraft Noise Reduction Study on Inboard Slat-Tip Region”. en. In: *AIAA AVIATION 2023 Forum*. San Diego, CA and Online: American Institute of Aeronautics and Astronautics, June 2023.

[37] R. Zamponi et al. “Effect of porosity on Curle’s dipolar sources on an aerofoil in turbulent flow”. In: *Journal of Sound and Vibration* 542 (Jan. 2023), p. 117353.

[39] D. Casalino et al. “Flow confinement effects on sUAS rotor noise”. In: *Aerospace Science and Technology* 143 (Dec. 2023), p. 108756.

[40] J. E. Ffowcs Williams and D. L. Hawkings. “Sound generation by turbulence and surfaces in arbitrary motion”. en. In: *Philosophical Transactions of the Royal Society of London. Series A, Mathematical and Physical Sciences* 264.1151 (May 1969), pp. 321–342.

[41] A. Towne, O. T. Schmidt, and T. Colonius. “Spectral proper orthogonal decomposition and its relationship to dynamic mode decomposition and resolvent analysis”. en. In: *Journal of Fluid Mechanics* 847 (July 2018), pp. 821–867.

[42] J. Jeong and F. Hussain. “On the identification of a vortex”. en. In: *Journal of Fluid Mechanics* 285 (Feb. 1995), pp. 69–94.

[43] Rayleigh. “XXXI. Investigations in optics, with special reference to the spectroscope”. en. In: *The London, Edinburgh, and Dublin Philosophical Magazine and Journal of Science* 8.49 (Oct. 1879), pp. 261–274.

[44] T. Takaishi et al. “Quantitative Modeling of Sound Sources Around Civil Aircraft on Final Approach”. en. In: *8th Berlin Beamforming Conference (BeBeC)*. Berlin, Germany, 2020.

[46] M. Choudhari and M. Khorrami. “Slat Cove Unsteadiness: Effect of 3D Flow Structures”. en. In: *44th AIAA Aerospace Sciences Meeting and Exhibit*. Reno, Nevada: American Institute of Aeronautics and Astronautics, Jan. 2006.

[47] W. Lu et al. “Investigation on tones due to self-excited oscillation within leading-edge slat cove at different angles of attack: Frequency and intensity”. en. In: *Aerospace Science and Technology* 91 (Aug. 2019), pp. 59–69.

[48] K. Takeda et al. “Unsteady aerodynamics of slat cove flow in a high-lift device configuration”. en. In: *39th Aerospace Sciences Meeting and Exhibit*. Reno,NV,U.S.A.: American Institute of Aeronautics and Astronautics, Jan. 2001.

[49] W. Dobrzynski et al. “Airframe noise studies on wings with deployed high-lift devices”. en. In: *4th AIAA/CEAS Aeroacoustics Conference*. Toulouse,France: American Institute of Aeronautics and Astronautics, June 1998.

[50] A. Kolb et al. “Aeroacoustic Wind Tunnel Measurements on a 2D High-Lift Configuration”. en. In: *13th AIAA/CEAS Aeroacoustics Conference (28th AIAA Aeroacoustics Conference)*. Rome, Italy: American Institute of Aeronautics and Astronautics, May 2007.

[51] D. König et al. “Two-step simulation of slat noise”. en. In: *Computers & Fluids* 39.3 (Mar. 2010), pp. 512–524.

[52] B. Storms et al. “Aeroacoustic measurements of slat noise on a three-dimensional high-lift system”. en. In: *5th AIAA/CEAS Aeroacoustics Conference and Exhibit*. Bellevue,WA,U.S.A.: American Institute of Aeronautics and Astronautics, May 1999.

[53] M. R. Khorrami, M. E. Berkman, and M. Choudhari. “Unsteady Flow Computations of a Slat with a Blunt Trailing Edge”. en. In: *AIAA Journal* 38.11 (Nov. 2000), pp. 2050–2058.

[54] K. Takeda, X. Zhang, and P. Nelson. “Unsteady aerodynamics and aeroacoustics of a high-lift device configuration”. en. In: *40th AIAA Aerospace Sciences Meeting & Exhibit*. Reno,NV,U.S.A.: American Institute of Aeronautics and Astronautics, Jan. 2002.

[55] T. Imamura et al. “Three-Dimensional Unsteady Flow Computations Around a Conventional Slat of High-Lift Devices”. en. In: *AIAA Journal* 46.5 (May 2008), pp. 1045–1053.

[57] M. Murayama et al. “Study on Noise Generation from Slat Tracks Using a High-Lift Wing Model”. en. In: *21st AIAA/CEAS Aeroacoustics Conference*. Dallas, TX: American Institute of Aeronautics and Astronautics, June 2015.

[58] M. Murayama et al. “Study on Change of Noise Generation from Slat Track Shape”. en. In: *22nd AIAA/CEAS Aeroacoustics Conference*. Lyon, France: American Institute of Aeronautics and Astronautics, May 2016.

[60] G. Chen et al. “Effects of slat track on the flow and acoustic field of high-lift devices”. en. In: *Aerospace Science and Technology* 126 (July 2022), p. 107626.

[61] E. Van Bokhorst, J. Kok, and M. Tuinstra. “Parametric study of the effect of slat track geometry on noise emissions”. en. In: *28th AIAA/CEAS Aeroacoustics 2022 Conference*. Southampton, UK: American Institute of Aeronautics and Astronautics, June 2022.

[62] B. Bai, Y. Zhang, and X. Li. “Identification of the two-sources at the aircraft slat/fuselage juncture based on phased array”. en. In: *Aerospace Science and Technology* 135 (Apr. 2023), p. 108186.

[63] N. Molin, M. Roger, and S. Barre. “Prediction of Aircraft High-Lift Device Noise Using Dedicated Analytical Models”. en. In: *9th AIAA/CEAS Aeroacoustics Conference and Exhibit*. Hilton Head, South Carolina: American Institute of Aeronautics and Astronautics, May 2003.

[64] M. M. Choudhari et al. *Aeroacoustic Experiments in the Langley Low-Turbulence Pressure Tunnel*. en. Technical NASA/TM-2002-211432. Virginia: NASA, Feb. 2002.

[65] S. Melber-Wilkending. “Aerodynamics of the Wing/Fuselage Junction at an Transport Aircraft in High-Lift Configuration”. en. In: *New Results in Numerical and Experimental Fluid Mechanics VII*. Ed. by A. Dillmann et al. Notes on Numerical Fluid Mechanics and Multidisciplinary Design. Berlin, Heidelberg: Springer, 2010, pp. 529–536.

[66] B. Bai, D. Lin, and X. Li. “Identification of Flap Side-Edge Two-Source Mechanism Based on Phased Arrays”. en. In: *AIAA Journal* (July 2021), pp. 1–12.

[67] R. Davy and H. Remy. “Airframe noise characteristics of a 1/11 scale Airbus model”. en. In: *4th AIAA/CEAS Aeroacoustics Conference*. Toulouse,France: American Institute of Aeronautics and Astronautics, June 1998.

[68] D. P. Lockard, M. M. Choudhari, and V. N. Vatsa. “Aeroacoustic Simulations of the High-Lift Common Research Model and Validation with Experiment”. en. In: *28th AIAA/CEAS Aeroacoustics 2022 Conference*. Southampton, UK: American Institute of Aeronautics and Astronautics, June 2022.

[71] T. L. Turner et al. “Development of Slat Gap and Slat Cove Filler Treatments for Noise Reduction Assessment on the High Lift Common Research Model in the NASA LaRC 14x22”. en. In: *28th AIAA/CEAS Aeroacoustics 2022 Conference*. Southampton, UK: American Institute of Aeronautics and Astronautics, June 2022.

[72] D. P. Lockard et al. “Noise Simulations of the High-Lift Common Research Model”. en. In: *23rd AIAA/CEAS Aeroacoustics Conference*. Denver, Colorado: American Institute of Aeronautics and Astronautics, June 2017.

[74] M. Terracol, E. Manoha, and B. Lemoine. “Investigation of the Unsteady Flow and Noise Generation in a Slat Cove”. en. In: *AIAA Journal* 54.2 (Feb. 2016), pp. 469–489.

[75] R. Merino-Martínez et al. “Aeroacoustic design and characterization of the 3D-printed, open-jet, anechoic wind tunnel of Delft University of Technology”. en. In: *Applied Acoustics* 170 (Dec. 2020), p. 107504.

[76] J. Gao, X. Li, and D. Lin. “Numerical Simulation of the 30P30N High-Lift Airfoil Noise with Spectral Difference Method”. en. In: *AIAA Journal* 58.6 (June 2020), pp. 2517–2532.

[77] M. Murayama et al. “Experimental Study on Slat Noise from 30P30N Three-Element High-Lift Airfoil at JAXA Hard-Wall Lowspeed Wind Tunnel”. In: *20th AIAA/CEAS Aeroacoustics Conference*. _eprint: https://arc.aiaa.org/doi/pdf/10.2514/6.2014-2080. American Institute of Aeronautics and Astronautics, June 2014.

[79] P. R. Spalart and J. H. Watmuff. “Experimental and numerical study of a turbulent boundary layer with pressure gradients”. en. In: *Journal of Fluid Mechanics* 249 (Apr. 1993), pp. 337–371.

[80] L. Botero et al. “Parametric Analysis of the Influence of Slat Geometry on Acoustic Noise”. In: *2018 AIAA/CEAS Aeroacoustics Conference*. AIAA AVIATION Forum. American Institute of Aeronautics and Astronautics, June 2018.

[82] C. Teruna et al. “Numerical investigation of leading edge noise reduction on a rod-airfoil configuration using porous materials and serrations”. en. In: *Journal of Sound and Vibration* 494 (Mar. 2021), p. 115880.

[86] T. Ahlefeldt. “Microphone Array Measurement in European Transonic Wind Tunnel at Flight Reynolds Numbers”. In: *AIAA Journal* 55.1 (Jan. 2017). Publisher: American Institute of Aeronautics and Astronautics, pp. 36–48.

[87] D. S. Souza et al. “Dynamics of the large-scale structures and associated noise emission in airfoil slats”. en. In: *Journal of Fluid Mechanics* 875 (Sept. 2019). Publisher: Cambridge University Press, pp. 1004–1034.

[88] F. H. T. Himeno et al. “SPOD analysis of noise-generating Rossiter modes in a slat with and without a bulb seal”. en. In: *Journal of Fluid Mechanics* 915 (May 2021). Publisher: Cambridge University Press, A67.

[89] R. F.R.S. “XXXI. Investigations in optics, with special reference to the spectroscope”. In: *The London, Edinburgh, and Dublin Philosophical Magazine and Journal of Science* 8.49 (Oct. 1879), pp. 261–274.

Books & Book Chapters

[1] ICAO. *Global air transport outlook to 2030 and trends to 2040*. eng. ICAO circular. OCLC: 867767826. Montréal: International Civil Aviation Organization, 2013.

[22] J. Delfs. *Grundlagen der Aeroakustik - Lecture notes*. Braunschweig: Technische Universitat Braunschweig, Oct. 2021.

[24] G. G. Stokes. *On the Theories of the Internal Friction of Fluids in Motion, and of the Equilibrium and Motion of Elastic Solids*. en. Apr. 1845.

[28] “Lighthill’s Theory”. In: *Theory of Vortex Sound*. Ed. by M. S. Howe. Cambridge Texts in Applied Mathematics. Cambridge: Cambridge University Press, 2002, pp. 25–40.

[29] A. Hirschberg and S. W. Rienstra. *An introduction to aeroacoustics*. en. Eindhoven, The Netherlands: Eindhoven University of Technology, July 2004.

[36] S. Glegg and W. Devenport. “Chapter 5 - The Ffowcs Williams and Hawkings equation”. en. In: *Aeroacoustics of Low Mach Number Flows*. Ed. by S. Glegg and W. Devenport. Academic Press, Jan. 2017, pp. 95–114.

[38] D. G. Simons and M. Snellen. *Introduction to general acoustics and aircraft noise*. Aircraft Noise and Emissions Part A. Lecture notes from AE4431 - Aircraft Noise and Emissions. Delft, The Netherlands: Delft University of Technology, Aug. 2022.

[56] F. Amaral et al. *STUDY OF THE EFFECT OF PROTUSIONS ON THE SLAT NOISE USING BEAMFORMING TECHNIQUES AND LATTICE-BOLTZMANN METHOD*. Nov. 2014.

[59] Y. Yokokawa et al. "Noise Generation Characteristics of a High-lift Swept and Tapered Wing Model". In: *19th AIAA/CEAS Aeroacoustics Conference*. Aeroacoustics Conferences. American Institute of Aeronautics and Astronautics, May 2013.

[73] Y. Zhang et al. "Effects of Porous Gap Fillers on 30P30N Leading-Edge Slat Noise. Part I: Surface Pressure and Acoustics". In: *28th AIAA/CEAS Aeroacoustics 2022 Conference*. Aeroacoustics Conferences. American Institute of Aeronautics and Astronautics, June 2022.

[78] F. M. White. *Viscous fluid flow*. eng. 3. ed., internat. ed. McGraw-Hill series in mechanical engineering. Boston: McGraw-Hill, 2006.

[81] P. J. Roache. *Verification and validation in computational science and engineering*. Albuquerque, N.M: Hermosapublishers, 1998.

[92] D. C. Giancoli. *Physics for scientists and engineers with modern physics. Vol. 1.* English. 4th ed. Section: 558 blz. ; .. cm. Upper Saddle River: Pearson/Prentice Hall, 2008.

Theses

[32] C. Teruna. "Aerodynamic Noise Reduction with Porous Materials: Aeroacoustics Investigations and Applications". PhD thesis. Delft, The Netherlands: Delft University of Technology, 2022.

[45] Y. Ikuta. "Noise Prediction for Aircraft during Approach using Sound Source Data Obtained from Microphone Array Measurement". jp. MA thesis. The University of Tokyo, 2023.

Other References

[4] N. Dickson. *ICAO Noise Standards*. Montréal, Canada, 2013.

[5] Fraport. *Fraport - Noise Abatement*. Frankfurt, 2023.

[6] Heathrow. *Noise action plan | Heathrow*. London, 2019.

[7] Schiphol. *Minder hinder Schiphol*. Amsterdam, 2023.

[15] IATA. *Aircraft Technology Roadmap to 2050*. Geneva, 2019.

[18] A. Esque, G. Fuchs, and R. Riedel. *Fuel efficiency: Why airlines need to switch to more ambitious measures | McKinsey & Company*. Mar. 2022.

[27] D. James. *Aerodynamic Sound*. en. Lecture Notes. by Stanford University. 2021.

[69] T. L. Turner et al. "Wing structure for an aircraft". en. *US11001368B2*. May 2021.

[70] M. R. Khorrami, D. P. Lockard, and J. B. Moore. "Elastically deformable side-edge link for trailing-edge flap aeroacoustic noise reduction". en. *US 8,695,925 B2*. Apr. 2014.

[83] Airbus. *A320 Aircraft Characteristics Airport and Maintenance Planning*. Blagnac, 2020.

[84] R. Williams. *What speed does an A320 land at? At what speed do planes usually land?* en. 2023.

[85] ICAO. *Noise Certification Workshop*. en. Bangkok, 2006.

[90] EASA. *TYPE-CERTIFICATE DATA SHEET FOR NOISE No. EASA.A.064.3 for AIRBUS A320*. 2022.

[91] EASA. *TYPE-CERTIFICATE DATA SHEET FOR NOISE No. EASA.A.151 for AIRBUS A350*. 2023.

Appendices

The appendices serve as a supplement to the report, providing additional information on various topics. Appendix A provides an example calculation of noise certification margins according to the ICAO Chapter 14 noise requirements for an Airbus A320neo and an Airbus A350. Appendix B consists of an article on the relation between fuselage-wing-slat junction designs, and their aeroacoustic footprint. The article conveys the main message of this thesis. Appendix C provides a calculation of the influence on the total airframe Sound Pressure Level (SPL) through noise reduction at the fuselage-wing-slat junction. Additional information regarding the open-jet angle of attack correction root mean square errors is provided in Appendix D. Appendix E includes a manual for setting up an acoustic sponge zone in PowerCASE and provides background information on its working methodology. Lastly, the numerical measurements conducted for the aeroacoustic analysis of the scaled models are detailed in Appendix F.

A

Noise certification case studies

Table A.1 displays the EPNL noise measurements at the three certification points for an Airbus A320neo with LEAP-1A26 under various conditions. It can be seen that the aircraft stays well below the ICAO Annex 16 Chapter 14 regulations limits for its class of aircraft.

Table A.1: Noise certification test data of the airbus A320neo with LEAP-1A26 engines, adapted from [90]. Note that the cumulative cases are taken from the averaged results.

EASA record no.	Variant	Maximum Mass (kg)		Lateral (EPNdB)		Flyover (EPNdB)		Approach (EPNdB)	
		Take-off	Landing	Level	Limit	Level	Limit	Level	Limit
A71507	055	79000	67400	85.60	97.00	81.60	91.90	92.70	100.70
A71508	054	79000	66300	85.60	97.00	81.60	91.90	92.50	100.70
A71515	053	77000	67400	85.70	96.90	80.90	91.70	92.70	100.70
A71516	052	77000	66300	85.70	96.90	80.90	91.70	92.50	100.70
A71521	069	75500	67400	85.80	96.80	80.40	91.60	92.70	100.60
A71522	068	75500	66300	85.80	96.80	80.40	91.60	92.50	100.60
A71523	071	75000	67400	85.80	96.80	80.30	91.60	92.70	100.60
A71527	075	74000	67400	85.80	96.80	80.00	91.50	92.70	100.50
A71529	051	73500	67400	85.80	96.70	79.80	91.40	92.70	100.50
A71530	050	73500	66300	85.80	96.70	79.80	91.40	92.50	100.50
Averaged		75900	66960	85.74	96.84	80.57	91.63	92.62	100.61
Cumulative	**Cumulative Limit**		289.08	**Cumulative Level**		258.93	**Cumulative Margin**		30.15

Table A.2 displays the EPNL noise measurements at the three certification points for an Airbus A350 with Trent XWB-75 under various conditions. It can be seen that the aircraft stays well below the ICAO Annex 16 Chapter 14 regulations limits for its class of aircraft.

Table A.2: Noise certification test data of the airbus A350 with Trent XWB-75 engines, adapted from [91]. Note that the cumulative cases are taken from the averaged results.

EASA record no.	Variant	Maximum Mass (kg)		Lateral (EPNdB)		Flyover (EPNdB)		Approach (EPNdB)	
		Take-off	Landing	Level	Limit	Level	Limit	Level	Limit
A75206	010	280000	207000	89.9	101.7	88.5	99.2	96.5	105.0
A75207	013	280000	205000	89.9	101.7	88.5	99.2	96.4	105.0
A75413	023	280000	205000	89.9	101.7	88.5	99.2	96.4	105.0
A75208	016	278000	207000	90.0	101.7	88.1	99.1	96.5	105.0
A75209	015	277000	205000	90.0	101.6	87.9	99.1	96.4	105.0
A75210	001	275000	207000	90.1	101.6	87.4	99.1	96.5	104.9
A75211	009	275000	207000	90.1	101.6	87.4	99.1	96.5	104.9
A75213	002	272000	207000	90.2	101.6	87.0	99.0	96.5	104.9
A75215	003	268000	207000	90.3	101.5	86.6	98.9	96.5	104.9
A75216	007	268000	207000	90.3	101.5	86.6	98.9	96.5	104.9
Averaged		275300	206400	90.07	101.62	87.65	99.08	96.47	104.95
Cumulative	**Cumulative Limit**		305.65	**Cumulative Level**		274.19	**Cumulative Margin**		31.46

B

Article on the aeroacoustics of a fuselage-wing-slat junction

The article explores the relation between fuselage-wing-slat junction designs and their aeroacoustic footprint. At the moment of writing this report, the article has not yet been submitted to a journal. However, the author plans to submit the article to a relevant journal for aircraft-integrated aeroacoustics in 2024.

Aeroacoustic analysis of a fuselage-wing-slat junction

H.I.G. Piera
Delft University of Technology

The junction between the fuselage, wing, and slat is a known high-intensity noise source region for an aircraft in approach configuration. However, it is unclear how to design a junction optimised for structural loading and low noise. This paper investigates the relation between fuselage-wing-slat junction designs and their aeroacoustic footprint. Two configurations, one with simplified junction surfaces and another one with realistic junction surfaces, are evaluated using a two-wall open-jet PowerFLOW simulation at a chord-based Reynolds number of $1.0 \cdot 10^6$. The results are compared to a control set-up featuring a full-span slat. Under the analysed slat loading, impingements from the minor roll-up vortices arising near the slat side-edge and slat stump do not alter the far-field noise spectra, irrespectively of the junction design. In fact, both junction configurations are approximately 0.5 dB OSPL quieter than the control, in disagreement with earlier research. This study shows that it is possible to alter the slat cove wake such that slat-cusp-to-slat-trailing-edge flow impingement is prevented on part of the slat, also limiting the spanwise extent of the narrow-band resonance noise. The alteration of the slat cove wake depends on the orientation and shape of the slat side-edge, slat track, and their relative positioning. These findings show that incorporating aeroacoustic analyses early in the design process of a fuselage-wing-slat junction can result in a reduced-noise design without impacting the aircraft's loading.

I. Introduction

AIRFRAME noise is becoming a prominent noise source during the approach phase, largely due to the rise in aircraft equipped with quieter high-bypass turbofan engines. In recent commercial aircraft, airframe noise, mainly originating from landing gears and high-lift devices, often surpasses jet exhaust noise [1, 2]. Noise source localisation results from fly-over measurements have identified the inboard slat [3] and the junction between the slat, wing, and fuselage [4, 5] as significant localised noise sources spread over the frequency spectrum. However, it remains unclear how to design a fuselage-wing-slat junction optimised for loading and low noise.

The aeroacoustic characteristics of this junction have rarely been investigated. An early study by Molin et al. [6] created a simplified junction set-up in an open-jet wind tunnel to compare against a to-be-developed analytical noise prediction model. They concluded that roll-up vortices forming at the slat side edge are likely the largest contributor to increased noise radiation compared to a full-span slat control setup. Yet, it is unclear to what extent the conclusions from the study are representative of full-scale fuselage-wing-slat junction noise, nor what slat loading was tested. More recently, Ribeiro et al. [7] analysed the influence of slat tracks, slat side-edge shapes, flow interactions between the slat side-edge and track, and wing sweep on the overall noise radiation using PowerFLOW simulations of wind-tunnel experiments at a Reynolds number of $2.6 \cdot 10^6$. Introducing a fuselage-slat gap increased the broadband noise by about 4 dB between 1 and 10 kHz with respect to a case where no slat track was present. However, introducing slat tracks to the control (without gap) increased the noise of more than 5 dB for all the frequencies above 2 kHz. The effect of a fuselage-slat gap compared to a control with a slat track is unknown. Increasing the sweep by roughly 5° decreased the broadband noise by about 1.5 dB. This is thought to be related to the slat side-edge-to-cove flow reducing impingements from slat-cusp-to-slat-trailing-edge turbulent structures, which is a promising aero-structural noise reduction effect. How this translates to a set-up with slat tracks remains unknown. Neither the fuselage nor the wing was mentioned as a potential noise source. Conversely, Bai et al. [8] suggest that the impingement of horseshoe vortices near the wing-fuselage junction, as well as the impingement of roll-up vortices near the slat side-edge, are the two main causes for excess fuselage-wing-slat junction noise, which was shown to increase with the angle of attack for all Reynolds numbers ($1.0 \cdot 10^6$ - $9.0 \cdot 10^6$). Their results were based on wind-tunnel deconvoluted beamforming integration methods. Murayama et al. [9] investigated the noise radiation of turbulent structures stemming from the inboard slat side edge. Reducing the impingement of roll-up vortical structures on the slat side-edge itself, as well as weakening the strength and impingement of structures on the inboard slat track, reduced the noise radiation in the junction. The simulation and wind tunnel set-ups were geometrically not an exact match and showed varying results. This suggests that there is a tight link between the aero-structural design and the achieved aeroacoustic benefits.

The literature indicates that the fuselage-wing-slat junction is a significant local noise source. However, all studies have been performed on different, not easily nor openly reproducible model geometries, often without specifying the loading conditions. Hence, it remains unclear how aero-structural features near the junction impact the radiated sound power. This study aims to investigate the relation between fuselage-wing-slat junc-

tion designs and their aeroacoustic footprint by characterising easily reproducible geometries.

Section II and section III describe the computational method and research set-up, respectively. Thereafter, section IV analyses the numerical set-up for grid independence. Section V, section VI, and section VII describe the noise radiation, noise mechanism through impingements, and indirect noise mechanisms, respectively. Lastly, the concluding remarks are drawn in section VIII.

II. Aeroacoustic computational method

A lattice-Boltzmann method (LBM) based solver has been used to compute the flow field. PowerFLOW, a commercial implementation of an LBM solver, has been extensively used and validated across a multitude of aerospace aeroacoustic applications, such as airfoil noise, e.g. Teruna [10], general airframe noise, e.g. Lockard et al. [11], and inboard slat-noise, e.g. Ribeiro et al. [7], and Murayama et al. [9].

The LBM is based on a mesoscopic kinetic equation: the lattice-Boltzmann equation. It forms the foundation of the numerical technique by computing the advection and collision of fluid particles using a statistical gas kinetic model. For this implementation, the discretisation involves 19 discrete velocities in three dimensions (D3Q19), incorporating a third-order truncation of the Chapman-Enskog expansion [12].

The methodology employs a collision model derived from the Bhatnagar-Gross-Krook (BGK) theory [13]. The equilibrium condition is set to the Maxwell-Boltzmann distribution, a distribution for gas particles at rest [12]. Flow variables are calculated by integrating the particle distribution functions over the 19 discrete state directions. Turbulence is modelled by extending the LBM to include a turbulent relaxation time, which replaces the relaxation time of the BGK model [14].

The distribution of particles is resolved on a Cartesian mesh, also known as a lattice. The lattice-Boltzmann scheme is applied on a unit of the lattice defined as a voxel. The dimensions of voxels vary by a factor of 2 in adjacent resolution regions of the simulation domain. Surface elements, referred to as surfels, are used to discretise surfaces of solid bodies at the positions where they intersect with a voxel. To account for the effect of the sub-grid unresolved scales of turbulence, a model referred to as a Very Large Eddy Simulation (VLES) is implemented [15]. A two-equation $\kappa - \epsilon$ Renormalisation Group, following Yakhot and Orszag [16], taking the non-linearity of Reynolds stresses into account, is used to compute a relaxation time accounting for the turbulence. A pressure-gradient-extended wall model is used to approximate the no-slip boundary condition on solid walls [17], based on the extension of the generalised law-of-the-wall model [18]. These equations are iteratively solved from the first cell close to the wall to specify the boundary conditions of the turbulence model. For the first cell's boundary interaction, a slip algorithm, obtained as a generalisation of a bounce-back and specular reflection process, is used [19].

Far-field noise is computed using the Ffowcs-Williams and Hawkings (FW-H) acoustic analogy [20]. Specifically, the formulation 1A of Farassat and Succi [21]. In the case of this study, pressure fluctuations are captured on the solid surfaces, which, when input to the FW-H solver, will include only dipole surface noise sources. The FW-H solver is built into SIMULIA's PowerACOUSTICS and Opty-dB suite, which are used in this study.

III. Research set-up description

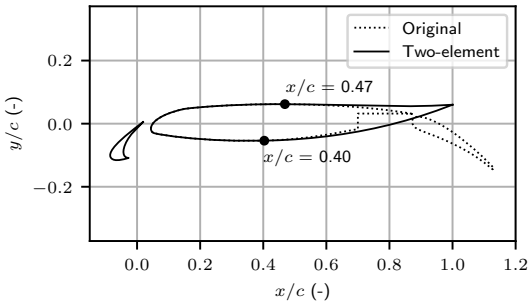

Figure 1: Modified two-element 30P30N compared to the original three-element cross-section.

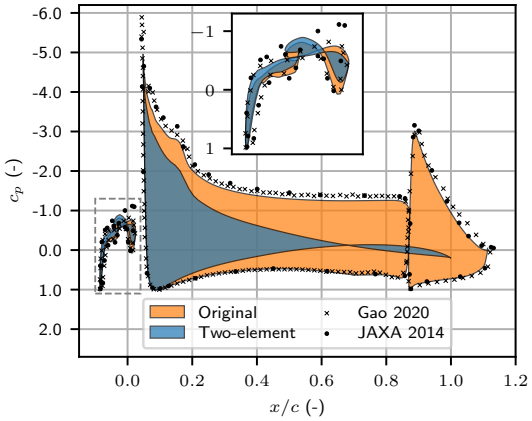

Figure 2: Pressure coefficient C_p distribution of the two-element geometry at $\alpha = 16°$ and three-element geometry at $\alpha = 4.0°$, compared to numerical data at $\alpha = 4.0°$ [22] and experimental data at $\alpha = 3.5°$ [23].

A. Slat-only 30P30N for open-jet facilities

A scaled fuselage-wing-slat model testable in both a numerical and experimental open-jet wind tunnel has been developed in the study. The set-up was engineered to be accommodated within the A-tunnel at TU Delft [24]. The 30P30N cross-section was chosen as a reference for reproducibility. The 30P30N has undergone extensive testing for slat noise, and its loading profiles are well-documented. To facilitate testing in an open-jet facility, the original three-element cross-section was modified to a two-element, slat-only configuration. The slat and main element leading edge loading were designed to be similar to an in-flight 30P30N flying at an approach angle of attack of $\alpha = 4.0°$. Terracol et al. [25] modified a

three-element Airbus FNG-type cross-section into a two-section configuration with minimal lift, maintaining the slat cove recirculation close to the original design. In this research, a comparable method was employed for slat loading rather than recirculation. The main element's leading edge remained unchanged, while the trailing edge was de-cambered to reduce lift. The leading edge on the suction side was consistent up to $x/c = 0.47$, and on the pressure side up to $x/c = 0.40$. The optimisation of the two-element design involved two variables: the angle of attack α and the trailing-edge position of the new main element $(y/c)_{TE}$. RANS simulations with a two-equation $\kappa - \epsilon$ turbulence model were iteratively conducted to fine-tune these parameters, aiming for a minimal lift on the main element and a slat lift behaviour similar to the original three-element design at the approach angle of attack. The optimised parameters for the new two-element configuration were $\alpha = 16°$ and $(y/c)_{TE} = 0.06$.

The newly proposed geometry is illustrated in figure 1. The loading patterns at a free-stream velocity of $U_\infty = 30$ m/s are depicted in figure 2. The loading differential between the upper and lower sides of the slat exhibited consistent behaviour across the slat chord with three distinct loading sections on both geometries. The areas for each of the three polygon sections give the loading per chord-length $\oint_a c_p dA$, with $a = f(c_p, x/c)$. These are, from upstream to downstream section, $(0.013, -0.006, 0.015)$, and $(0.016, -0.009, 0.008)$ for the three-element and two-element respectively, resulting in a total loading per chord length of 0.022, and 0.015. Moreover, the loading of the main element was significantly reduced. The magnitude of the suction side loading of the original cross-section is slightly underestimated when compared to the numerical data from Gao et al. [22] and JAXA's experimental data from Murayama et al. [23]. Nevertheless, the new geometry reduces the total lift while maintaining a similar slat and main element leading-edge loading.

B. Description of the geometrical set-up

The 30P30N model was modified to incorporate 3D elements to properly investigate the fuselage-wing-slat junction noise mechanism. A balance was struck between the simplicity of the set-up, compatibility with the TU Delft's A-tunnel, and manufacturability. The inspiration for the junction surface geometries, such as the slat horn, slat stump, and track position, was taken from Airbus' A320. Melber-Wilkending [26] explains that commercial aircraft include these features to improve the aerodynamics of the overall aircraft by creating a strong streamwise vortex near the wing root that delays root stall at high angles of attack by minimising the trailing-edge corner separation. Flyover-noise studies performed on Airbus aircraft [4, 5] even refer to the fuselage-wing-slat junction noise as 'slat horn noise', although the influence of a slat horn is still up for debate. The ratio of the slat length to the main element length was maintained at $c_s = 0.15c$ to preserve a slat recirculation similar to the 2D three-element 30P30N. The half-span b was set to 0.5 m to fit within the A-tunnel's 0.5 m $\times$ 0.5 m nozzle. An aspect ratio of 1.0 was used to create a slat chord of 78 mm with blunt trailing edges of 0.15 mm for manufacturability. The sweep $\phi = 25°$, the sideplate-slat gap of 65 mm, and the relative location of the inboard slat track at 96 mm from the sideplate were modelled after the Airbus

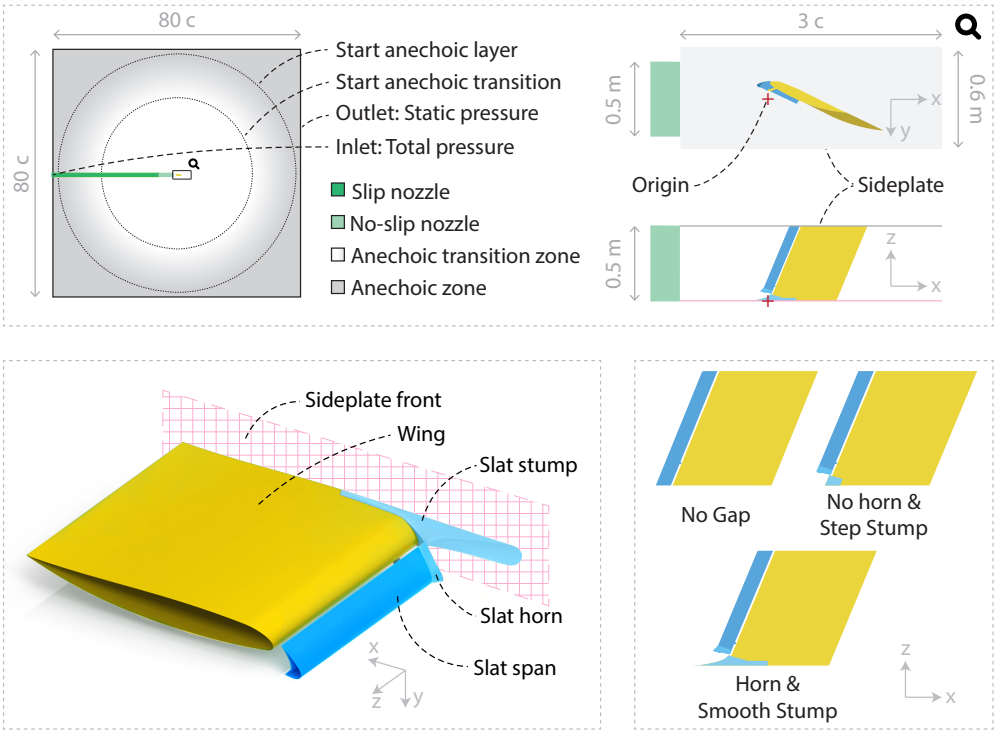

Figure 3: Schematic representation of the research set-up.

A320. The set-up main wing lacks tapering and twisting, resulting in a spanwise load distribution with isobars roughly parallel to the sweep angle. Finally, the ratio of the expected fuselage boundary-layer thickness to the fuselage-slat gap length was kept constant, assuming that the entire length of the fuselage created a turbulent boundary layer. The flat-plate turbulent boundary-layer approximation estimates the fuselage boundary layer of the A320 to be roughly 160 mm at the wing leading edge, whereas the A320's slat gap is roughly 200 mm. Hence, the research set-up should create a turbulent boundary-layer thickness of roughly $16/20 \cdot 65 \approx 50$ mm.

Three geometries are considered, depicted in figure 3. A simple No Gap (NG) geometry, which only incorporates the sweep and slat track position, a No Horn & Step Stump (NH) geometry, which introduces a sideplate-slat gap and a step stump, and the Horn & Smooth Stump (H) geometry, which includes a slat horn and a smooth slat stump loosely modelled after the Airbus A320. The location of the slat track remained consistent across all three geometries. The open-jet set-up used two sideplates, necessitating corrections to the geometrical angle of attack to create a similar effective angle of attack. The geometrical angle of attack was determined iteratively. Drawing from the work of Terracol et al. [25], who used a similar two-element setup and corrected from $18°$ to $25°$, the same ratio was applied as a starting point for the angle of attack correction, resulting in an initial angle of attack of $\alpha = 22.2°$. Five additional coarse simulations at $24.2°$, $25.2°$, $26.2°$, $27.2°$, and $28.2°$ were conducted to conclude that $26.2°$ most closely resembled the 2D RANS simulation based on the root mean square error (RMSE) of the pressure coefficient C_p compared to RANS, as shown in figure 4. The total RMSE simply represents the sum of the RMSE's for the four parts. A comparison of loading between the $16°$ PowerFLOW 2D RANS and the $26.2°$ open-jet 3D PowerFLOW will be presented in section IV.

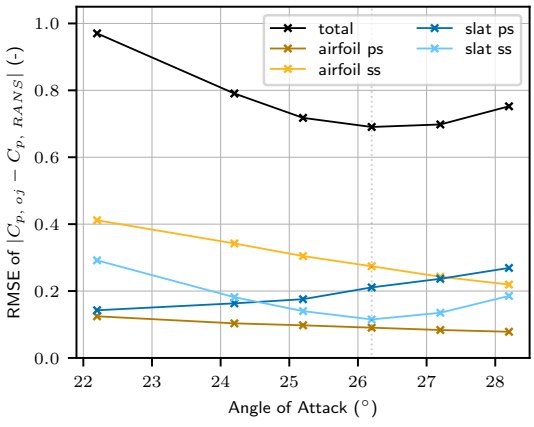

Figure 4: Angle of attack determination based on the root mean square error (RMSE) compared to the $16°$ RANS case.

C. Description of domain & boundary conditions

The three geometries were tested under identical flow conditions, described in table 1. The domain is a cubic space with dimensions of $80 \times 80 \times 80$ chord lengths, with all outer boundaries set to an outlet static pressure equal to the static ambient condition p_s, as shown in figure 3. The inlet boundary condition in the nozzle is set by the total pressure $p_t = p_s + q$, where the dynamic pressure q is derived from the fluid parameters and flow conditions outlined in table 1. An anechoic transition layer is used to dampen acoustic reflections within the domain by numerically modifying the ν/T value. This layer was designed to gradually transition from an echoic to an anechoic fluid, similar to what was done byTeruna et al. [27]. The start of this transition was positioned sufficiently distant from the nozzle jet to prevent the formation of a large static pressure zone caused by the jet encountering increased viscosity. The domain incorporates both slip and no-slip nozzles. The no-slip nozzle, combined with a trip in the nozzle, was designed to induce a boundary-layer thickness of approximately 50 mm within the sideplate-slat gap, as depicted in figure 3. Analysis of the boundary-layer thickness using the 99% value of the end velocity through the integration of vorticity along a wall-normal line ($U_e = \int \omega_y dz$), introduced by Spalart and Watmuff [28], revealed a boundary-layer thickness of 68 mm for the analysed medium refinement case, described next.

Table 1: Fluid parameters and flow conditions.

Density	ρ	(kg m^{-3})	1.225
Ambient static pressure	p_s	(Pa)	101325
Speed of sound	c_{sos}	(m s^{-1})	340.3
Dynamic viscosity	μ	(kg m^{-1} s^{-1})	$1.79 \cdot 10^{-5}$
Temperature	T	(K)	288.15
Free-stream velocity	U_∞	(m s^{-1})	30
Chord Reynolds number	Re_c	(-)	$1.03 \cdot 10^6$

A coarse, medium, and fine grid separated by a refinement factor of $r = 1.5$ were considered. All grids employ nine VR zones at the same locations, depicted in figure 5. The largest voxel size VR_0, smallest voxel VR_8, median $y+$, total number of voxels N_{voxels}, number of fine equivalent voxels $N_{fine\ eq.}$, number of timesteps $N_{timesteps}$, and the number of CPU hours CPUh are provided in table 2.

Table 2: Grid-refinement parameters.

		Coarse	**Medium**	**Fine**
VR_0	(m)	$c/4$	$c/6$	$c/9$
VR_8	(m)	$c/1024$	$c/1536$	$c/2304$
Median y^+	(-)	33.7	24.0	16.3
N_{voxels}	(-)	$138 \cdot 10^6$	$451 \cdot 10^6$	$1465 \cdot 10^6$
$N_{fine\ eq.}$	(-)	$34.1 \cdot 10^6$	$109 \cdot 10^6$	$349 \cdot 10^6$
$N_{timesteps}$	(-)	$483 \cdot 10^3$	$724 \cdot 10^3$	$1086 \cdot 10^3$
CPUh	(h)	$5.659 \cdot 10^3$	$23.81 \cdot 10^3$	$83.41 \cdot 10^3$

IV. Grid independence analysis

A. Lift & drag based grid convergence

The grid convergence analysis was performed on the Horn & Smooth Stump geometry. The grid convergence

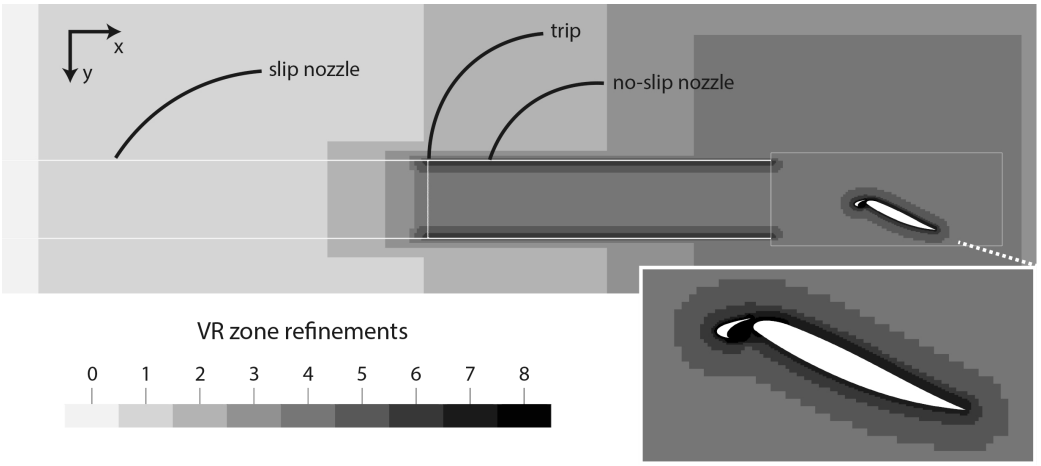

Figure 5: VR zone discretisation.

index GCI helps estimate the deviation of an integral parameter on a given grid to an asymptotic solution for an infinitely fine grid. The asymptotic solution can be estimated using a Richardson extrapolation [29]. Figure 6 demonstrates the convergence trend of the integral lift and drag coefficients C_l and C_d. The drag coefficient shows a negative order of convergence p, i.e. the deviation between the medium and fine grid is larger than the deviation between the medium and coarse grid, indicating that it has not reached a satisfactory asymptotic convergence. The GCI for the lift coefficient transitioned from coarse to medium grid at $GCI_{c,m} = 0.257\%$ and from medium to fine grid at $GCI_{m,f} = 0.096\%$, yielding a GCI ratio of approximately 1, specifically 1.0095. The calculated order of convergence p was 2.50. The small value of the medium GCI and the GCI-ratio close to unity indicates that the medium refinement lies within the asymptotic range of convergence for the lift coefficient [29].

The stability over time of the lift and drag coefficients is subject to discussion. The mean progression of the coefficients by averaging period, visualised in figure 7, indicates neither force has fully reached its asymptotic mean, questioning the validity of the Richardson extrapolation's magnitudes. However, the trends show that increasing the lift coefficient's C_l averaging period will result in a smaller deviation between the medium and fine grids than between the medium and coarse grid, indicating asymptotic convergence.

B. Time-averaged surface streamlines

Surface streamline visualisations allow for qualitative assessment and comparison of the flow behaviour across grid refinements. Figure 8 presents a comparison of streamlines and skin friction across grid refinements on the set-up's suction side and inside the slat cove (a plane looking towards the mean flow direction). Streamlines on the suction side of the element exhibit similar flow patterns across all cases, where the medium and fine case are in close agreement on the slat stump (region A in Figure 8), near the leading edge (B), and near the outboard sideplate (C). This indicates that vortices arising near the junctions are similar between the medium and fine cases and, to a lesser degree, to the coarse case. The skin friction and streamlines within the slat cove show a significant deviation between the coarse case and the medium & fine cases. The recirculation line extends considerably further towards the slat cusp in the coarse simulation. The fine simulation predicts a recirculation area (from the slat trailing edge to the recirculation line) slightly smaller than the medium case. Their overall patterns are similar. In conclusion, the medium and fine cases are in close agreement in terms of flow pattern, whereas the coarse case deviates from the other two.

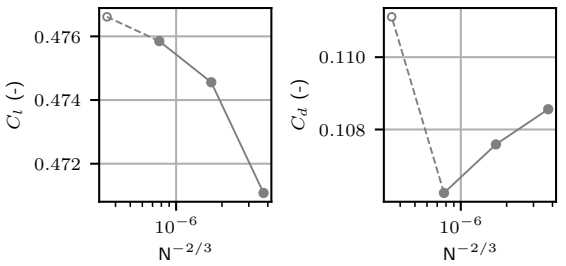

Figure 6: Richardson extrapolation of the lift and drag coefficient of the entire element.

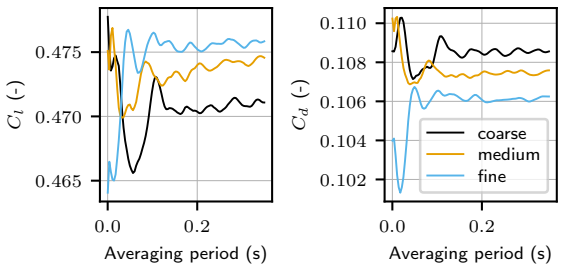

Figure 7: Mean progression of the lift (left) and the drag (right) by averaging period.

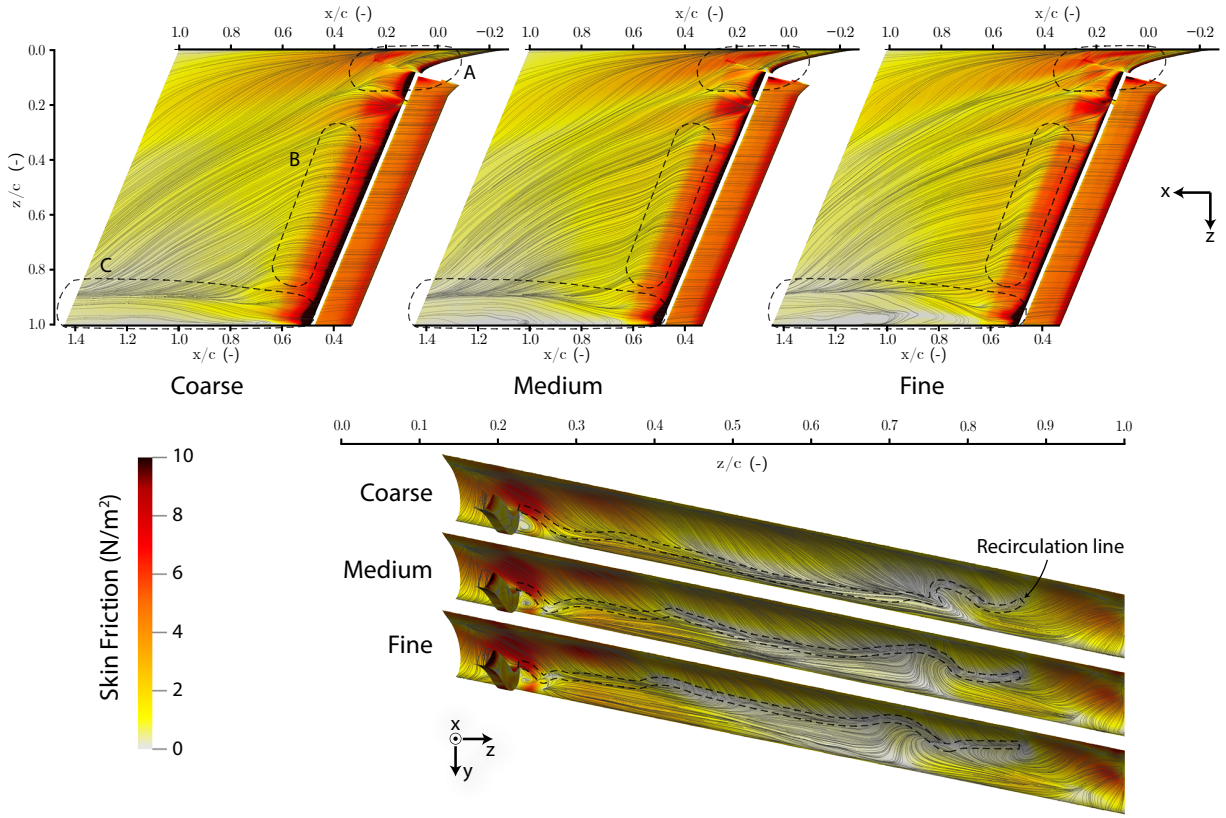

Figure 8: Streamline and skin friction visualisation of the three grid refinements using an averaging period of 0.33 s, resulting in roughly 130 slat flow-throughs at a slat-based Strouhal number of $St_{c_s} = 8.3 \cdot 10^{-3}$.

C. Time-averaged streamwise loading at $z = 0.5b$

The streamwise pressure coefficient distribution describes the streamwise force distribution per spanwise section. Figure 9 displays the loading of three PowerFLOW grid refinements, the 2D two-element RANS simulation for the slat and main element, and the 2D three-element RANS simulation from Gao et al. [22] for the slat. A finer grid corresponds slightly more closely with the RANS 2D case. Furthermore, the PowerFLOW cases align more closely to the numerical data from Gao et al. [22] than the two-element RANS performed for this study. Each refinement results in an increased extent of the suction peak. The point of loading reversal on the

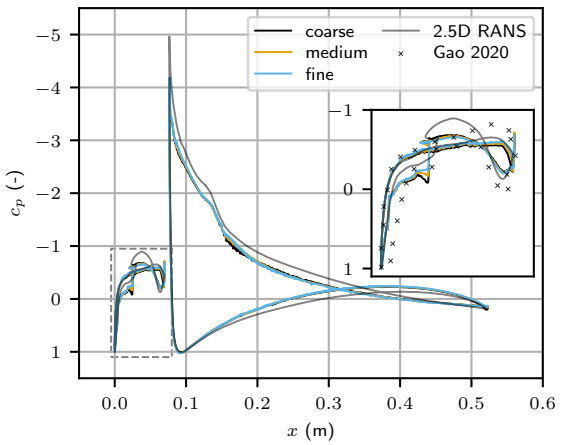

Figure 9: Pressure coefficient distribution of the mesh refinements and the 2D RANS simulation.

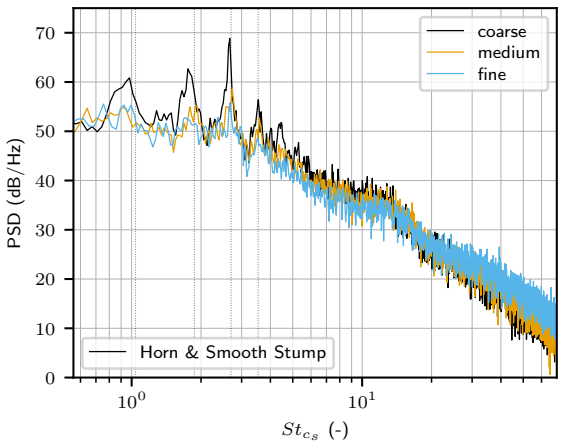

Figure 10: Power spectral density of the mesh refinements with a resolution of $\Delta f = 12$ Hz $\rightarrow \Delta St_{c_s} \approx 0.034$ at $x, y, z = (0.0, 1.6c, 0.5b)$.

main element is positioned more forward in the PowerFLOW simulations than in the RANS, likely attributable to the jet expansion in the PowerFLOW open-jet setup. In short, all grid refinements are adequate in terms of streamwise loading. The PowerFLOW simulation aligns closely with RANS results from the literature.

D. Far-field noise

Figure 10 compares the effect of grid refinement on far-field noise from a numerical probe in the mid-plane $z = 0.5b,\ 1.6c$ below the slat-retracted leading edge, $(x, y, z) = (0.0, 1.6c, 0.5b)$, by considering the acoustic pressure power spectral density (PSD). The observations will be discussed in terms of broadband noise and narrow-band Rossiter-like slat peak noise. The broadband noise across grid refinements is largely similar. A finer grid decreases the broadband noise below a slat-based Strouhal number of $St_{c_s} \approx 15$, above which a finer grid increases the broadband noise. The coarse grid predicts significantly higher intensity narrow-band peaks than the medium and fine case. In conclusion, the medium and fine cases show similar noise responses, which makes the medium refinement adequate for noise mechanism analyses. The sharp difference with the coarse variant is likely related to the dissimilar flow patterns in the slat cove, as the slat peaks are the dominant noise sources.

V. Far-field noise description per set-up

This section explores the far-field noise radiation of the three different geometries using a direct numerical probe, and a solid formulation of the FW-H equation. Henceforth all analyses are performed using the medium refinement. Figure 11 suggests that the geometries have the same spectral characteristics. At least four Rossiter-like modes are visible below $St_{c_S} \approx 4$, after which the sound power tapers of. Between the Strouhal number of 10 and 20 a hump is present in the noise response, which is related to vortex shedding of slat's trailing edge. The dissimilarities are presented next. As quantified by table 3, the geometries with a sideplate-slat gap (H and NH) consistently display (slightly) lower noise magnitudes at the main narrow-band peaks, resulting in an OSPL (St_{c_s} $0.3 - 70$) of 83.2 dB and 83.3 dB respectively, compared to 83.8 dB for the NG variant. This contradicts earlier findings from literature that found a multiple decibel increase when a fuselage-slat gap was introduced [7, 11]. A second observation reveals that the NG geometry has its narrow-band peaks at slightly higher frequencies than the geometries with a sideplate-slat gap.

Table 3: Sound pressure level (SPL) and ΔSPL, compared to the NG geometry, in dB around the main Rossiter-like modes.

	$500 - 800$ Hz St_{c_s} $1.40-2.24$		$850 - 1150$ Hz St_{c_s} $2.38-3.22$		$1200 - 1500$ Hz St_{c_s} $3.35-4.19$	
NG	76.70,	N/A	77.58,	N/A	74.43,	N/A
NH	76.67,	-0.03	75.61,	-1.97	74.02,	-0.41
H	75.99,	-0.71	77.36,	-0.22	72.98,	-1.44

Next, the validity of using the solid formulation of the FW-H acoustic analogy is evaluated for far-field analyses (FFA). Figure 12 compares the direct probe and FFA results for the three different geometries. In all three geometries the FFA resulted in near-identical power spectral densities. The radiation starts to deviate slightly after a Strouhal number of 3.0, as the surface measurements from which the far-field radiations are constructed had a sampling frequency of roughly 5.5 times that number. The close match between the probe and far-field propagation provides confidence to use the FW-H based results for a more in-depth analysis of the far-field noise mechanisms.

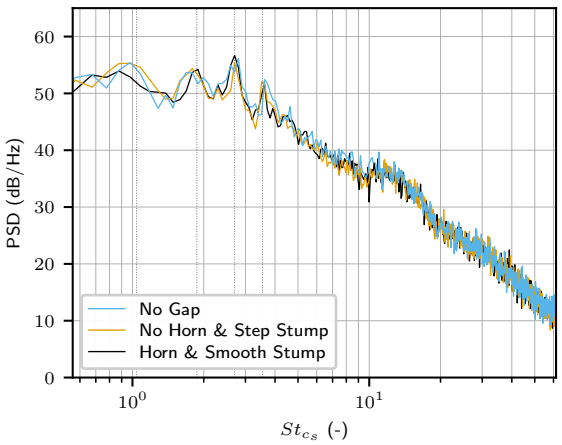

Figure 11: Power spectral density with a resolution of $\Delta f = 36$ Hz $\rightarrow \Delta St_{c_s} \approx 0.101$ at $x, y, z = (0.0, 1.6c, 0.5b)$.

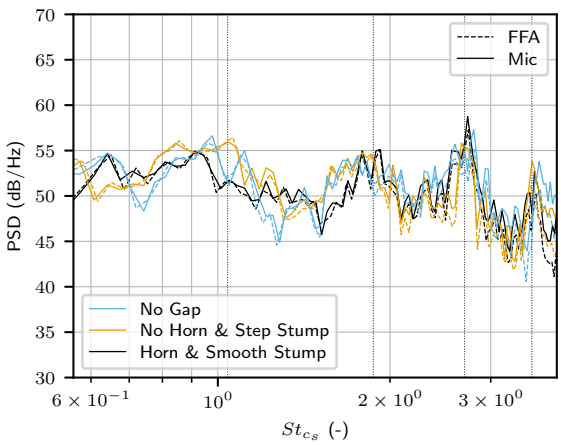

Figure 12: Probe and far-field analysis using a solid formulation of the FW-H equation with a resolution of $\Delta f = 12$ Hz $\rightarrow \Delta St_{c_s} \approx 0.034$ at $x, y, z = (0.0, 1.6c, 0.5b)$.

VI. Impingement noise in the fuselage-wing-slat junction

A. Vortical topology in the junction

The fuselage-wing-slat junction generates multiple coherent vortices [26], which are hypothesised to influence the pressure fluctuation intensity on the surfaces, and hence the far-field noise response. A comparison of the vortex topology between the No Horn & Step Stump (NH) and Horn & Smooth Stump (H) designs is provided in figure 13. The vortices are visualised using a λ_2-criterion at $-4{\cdot}10^7$ and coloured by the streamwise vorticity. Both the NH and H geometries produce a roll-up vortex on the slat chord, where the H geometry's roll-up vortex is of greater size and vorticity strength due to the elongated side-edge (figure 13, region A). For both geometries the vortex impinges on the slat trailing edge corner, after which it moves past the wing without impinging. The vortex arising at the trailing edge of the slat cusp, which traverses inside the slat cove, as predicted by Murayama et al. [9], is also more coherent for the H geometry (figure 13, region B). At the edge between the stump and wing, multiple vortices arise, which are of greater streamwise vorticity strength for the NH geometry. The vortices impinge on the side-edge of the slat stump, and on the main wing. A clear horseshoe vortex on the slat stump has not materialised for either geometry. In conclusions, roll-up vortices are created on the slat side-edge, which scale on its length. These vortices however, do not impinge meaningfully near the junction, but might impinge on the stump side-edge, the slat trailing edge and in the slat cove. However, the strength of these vortices is limited, likely related to the weak loading of the 30P30N's slat at the approach angle of attack of $4.0°$. A clear horseshoe vortex was not observed in this simulation.

B. Surface pressure fluctuation intensity

Regions with high intensity surface pressure fluctuations p' often serve as a precursor to high-intensity noise sources. If impingements from vortices in the junction are a root cause for the research set-up's noise, these would show up in surface p'_{rms} visualisations. Figure 14 presents the broadband pressure fluctuation intensity for all geometries. The intensities of the fluctuations originating from the expected vortices in the junction, encircled by region A in figure 14, are relatively weak. The fluctuation intensity from the side-edge roll-up vortex is barely discernible on the slat trailing edge. The side of the slat stump and the slat stump itself exhibit only moderate pressure fluctuation intensities compared to fluctuations stemming from turbulent structures from the slat track impinging on the main element's wing. Inside the slat cove, the influence of the sideplate-slat gap is clearly visible. The geometries that include a gap display a deep extent of high pressure fluctuation intensities outboard of the slat track, encircled by region B in figure 14, with the highest intensity region just aft of the track. This pattern is not visible in the No Gap geometry, hence it must be related to the interplay between the sideplate-slat gap, and the track.

C. Noise radiation of different slat horn & stump geometries

The contributions to the total far-field noise per component can be quantified using the FW-H propagation of the surface pressure fluctuations, which has been verified in section V. The research set-up has been subdivided into the components visualised in figure 3 (the back sideplate and slat track were individual components too, but not explicitly shown or labelled in the figure). Figure 15 reveals that for both 'Gap'-geometries pressure fluctuations stemming from the slat span dominate the spectrum above $St_{c_s} \approx 1.1$, below which the wing is the dominant noise contributor. This trend continues for higher frequencies, although not visualised. Slight differences are present between the NH and H geometries. The PSD for all frequencies from the smooth stump exceed those from the step stump (figure 15). However, this is likely caused by the increased surface area of the smooth

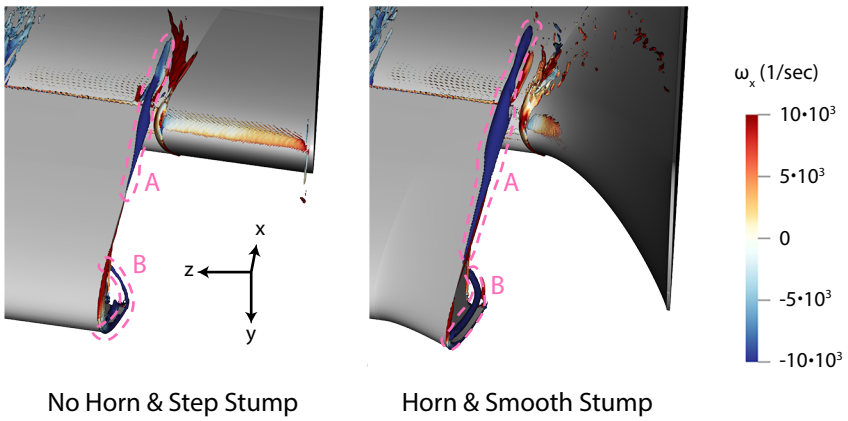

Figure 13: Vortex topology through $(\lambda_2 = -4 \cdot 10^7)$-iso-surfaces, coloured by the streamwise vorticity with an averaging period of roughly 4 streamwise slat passages or 0.0067 s. Blue indicates negative vorticity, and red indicates positive vorticity.

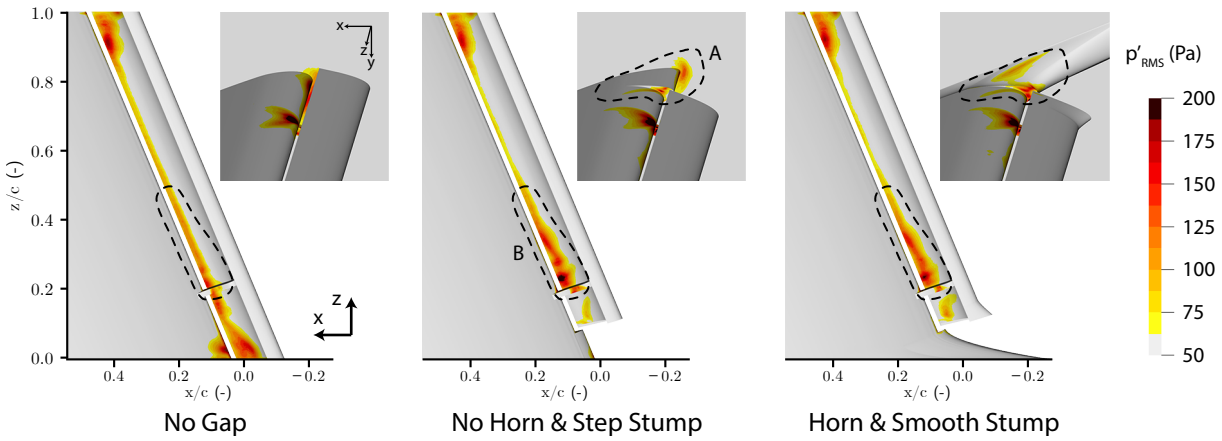

Figure 14: Pressure fluctuation intensities through p'_{rms} values for a flow duration of 0.33 s at a measurement frequency equal to the simulation's timestep frequency.

stump, as the noise spectrum starts to correlate to the front sideplate (e.g. at $St_{c_s} \approx 2.0$). The marginally increased size and strength of the side-edge roll-up vortex for an elongated slat horn do not lead to a significantly altered far-field noise radiation. In short, given the current flow and loading conditions, the change in horn and stump design do not alter the noise radiation.

This observation holds for other directions as well. Figure 16 depicts the sound pressure levels derived from the solid FW-H propagation between St_{c_s} 0.3 and 3.9 in all directions in the midplane $z = 0.5b$, with the x_i, y_i coordinates of the mircrophones given by

$$\theta_i = 2\pi \cdot i / N_{\text{mics}} \qquad i = 0, 1, \ldots N_{\text{mics}} - 1$$
$$x_i = R \cdot \cos(\theta_i) + x_0$$
$$y_i = R \cdot \sin(\theta_i) + y_0$$

where the radius R was set to $4c$, and the origin x_0, y_0 to 0 m and 0.05 m respectively. The main difference between the two geometries is that the smooth slat stump exhibits a higher correlation with the front sideplate as it effectively morphs the sideplate with the main wing. Additionally, the clear dipole pattern of the slat span dominates the noise, except where the dipoles cancel each-other ($30°$ and $210°$), at which point the wing noise level exceeds that of the slat. Lastly, in aft-direction the total noise is clearly shielded by the body, indicating that the main noise sources indeed lie near the leading edge of the research set-up. Hence, different horn and stump design do not affect the total noise response under the current flow and loading conditions.

VII. Slat cove noise influenced by large-scale 3D flow structures

Under the researched flow and loading conditions, noise due to direct impingements in the junction were not a significant source of noise. However, as referenced in

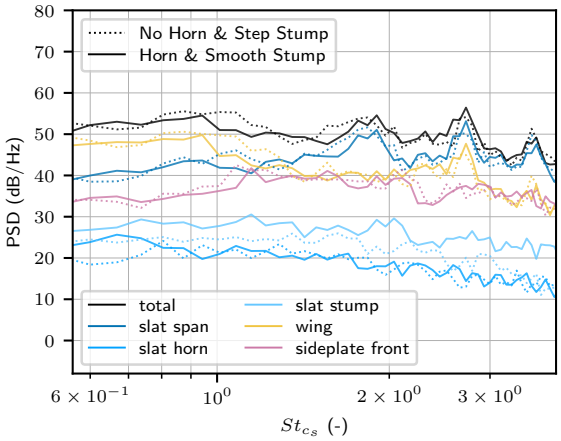

Figure 15: Component power spectral density from a solid formulation of the FW-H equation with a resolution of $\Delta f = 24$ Hz $\rightarrow \Delta St_{c_s} \approx 0.067$ at $x, y, z = (0.0, 1.6c, 0.5b)$.

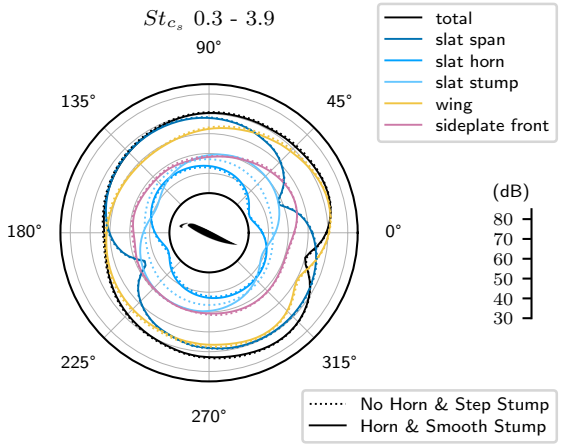

Figure 16: Directivity of the sound pressure level (SPL) from a solid formulation of the FW-H equation.

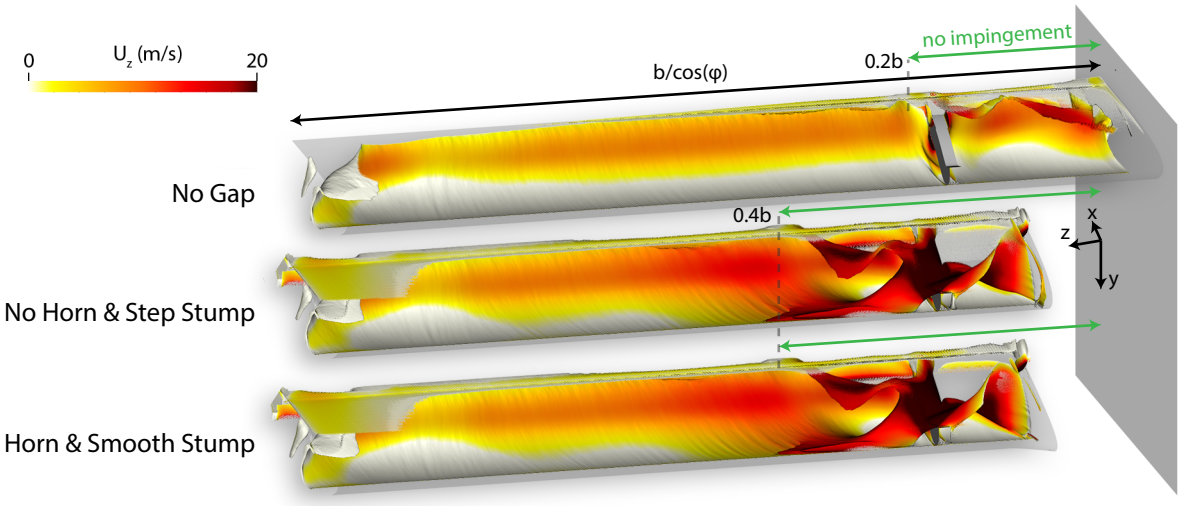

Figure 17: Comparison of the slat cove wake through ($C_{p,\ total} = 0$)-isosurface coloured by the outboard spanwise velocity in red using an averaging period of 0.33 s, resulting in roughly 130 slat flow-throughs at a slat-based Strouhal number of $St_{c_s} = 8.3 \cdot 10^{-3}$.

section V, the model configuration that lacks a sideplate-slat gap exhibits higher intensity narrow-band peaks. Moreover, the frequencies of these narrow-band peaks deviate when the sideplate-slat gap is introduced. It is well recognised that these peaks emit noise in the form of Rossiter-like cavity noise across the slat span. Himeno et al. [30] have shown that the frequencies of the Rossiter modes vary based on the slat recirculation. The subsequent sections will clarify the mechanisms contributing to the amplified noise and the alterations in peak frequencies.

A. Slat cove flow dynamics

The turbulent structures in the slat cove and their path play an important role in the noise response of the research set-up. The sideplate-slat gap has a significant effect on the slat cove wake. Figure 17 displays the iso-surface of $C_p = 0$, visualising the extent of the wake, coloured by the spanwise velocity inside the slat cove. The slat is shown partially transparent. The research set-up incorporates a sweep angle ϕ, a slat track, and a sideplate-slat gap, resulting in large-scale 3D flow phenomena inside the slat cove. The shape of the wake indicates that the introduction of the sideplate-slat gap significantly disrupts the coherency of the slat recirculation flow across a substantial portion of the slat span. Air is transported through the gap to inside the slat cove and accelerates over the slat track. This flow pattern enhances the turbulence just outboard of the slat track, as clearly demonstrated by figure 14 region B. Himeno et al. [30] explain that for 2.5D slat geometries, acoustic waves stemming from the slat trailing edge impingement trigger the formation of new vortices at the cusp, forming a flow-acoustic interaction that selects certain frequencies, resulting in narrow-band resonance. In this set-up, however, the slat mean shear does not impinge near the trailing edge until $z = 0.4b$ for the geometries with a sideplate-slat gap. Additionally, as seen from the spanwise velocity colouring, the slat cove recirculation is altered across the entire span. Hence, although the pressure fluctuation intensity is increased aft of the slat track by the introduction of a sideplate-slat gap, impingement of the mean shear line near the trailing edge does not occur until well into the slat span, possibly decreasing the narrow-band resonance.

B. Narrow-band resonance extent

The impact of the alteration of the slat cove's recirculation bubble on the Rossiter modes can be visualised using a FW-H based noise source visualisation technique introduced by Casalino et al. [31]. This technique computes the contribution of each surface element to the far-field noise at a specific location using FW-H based noise propagation. The method distinguishes between elements that contribute constructively (in-phase) and destructively (out-of-phase) per frequency band. Consequently, it can also describe the coherence of different source locations per frequency, as resonating elements are coherent. Therefore, an FW-H based noise visualisation focused around a narrow-band peak such as the St_{c_s} $2.1 - 2.9$ band, will provide insights into the slat span-based extent of resonance of the tonal noise. Figure 18 visualises the Coherent Output Power (COP) on the left, i.e., all noise source mechanisms, regardless of whether they contribute in or out of phase to the far-field noise at the specified microphone location, the Coherent Power (CP), i.e. in phase contributions, in the middle, and the Destructive Power (DP), i.e. out-of-phase contributions, on the right. The slat chord trailing edge is clearly the largest contributor to the total noise at this frequency band, as seen from the COP and CP. The resonating elements are visible in the CP visualisation. As suggested by the slat cove wake, the resonating area of the research setup is considerably smaller when a sideplate-slat gap is present, in this case the Horn & Smooth Stump geometry. The extent of the resonance

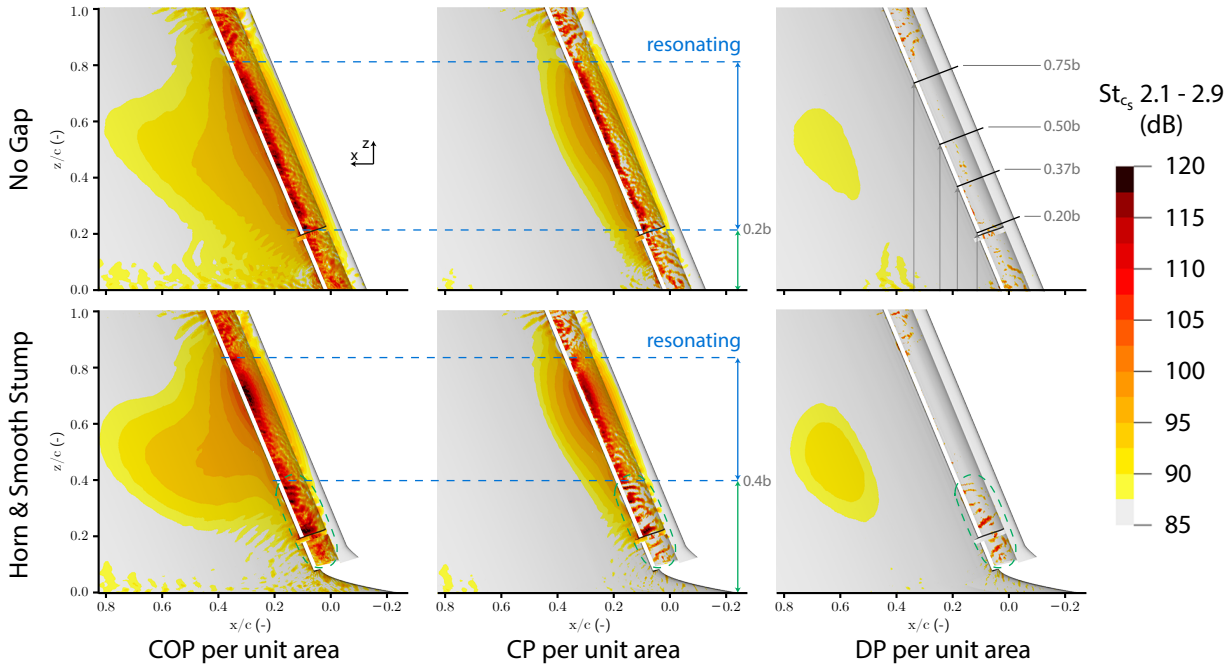

Figure 18: Coherent Output Power (COP), Constructive Power (CP), and Destructive Power (DP) comparison of a geometry with and without sideplate-slat gap between $St_{c_s}\,2.1 - 2.9$.

is perhaps most clearly visible on the main element itself, which shows the acoustic reflections from the slat trailing edge. The resonance is broken by the additional high-intensity sources which show up alternatingly in- (CP) and out-of-phase (DP) (encircled in figure 18 in the Horn & Smooth Stump geometry). Casalino et al. [31] explain that such sources are ineffective at radiating noise to the far-field. The broken resonance is believed to be the primary mechanism causing the decrease in energy of the narrow-band peaks when a sideplate-slat gap is present, as indicated in table 3.

C. Narrow-band centre frequencies

The introduction of a sideplate-slat gap appears to marginally reduce the frequency of each Rossiter-like mode (figure 11). The frequencies of the narrow-band peaks are only contingent on the shedding within the slat cove, if Strouhal scaling is used. Figure 19 visualises the impact of the sideplate-slat gap on the slat cove recirculation through a Line Integral Convolution (LIC). The flow topology was captured on a plane perpendicular to the slat span at $z = 0.75b$ where all geometries were resonating, as per figure 18. The flow topology outside the cove (O, in figure 19) exhibit similar patterns, whereas the flow topology within the cove (C, in figure 19) have undergone a stark alteration. The mean shear line and trailing edge impingement point are near identical between all cases. However, the NH and H geometries have an additional smaller recirculation area and an altered centre of the recirculation bubble. This was already suspected from the recirculation line depicted in figure 8. Frequency prediction models from both Terracol et al. [25] and Souza et al. [32] (the latter is given by eq. (1)) relate the centre of the narrow-band peaks to the acoustic path length

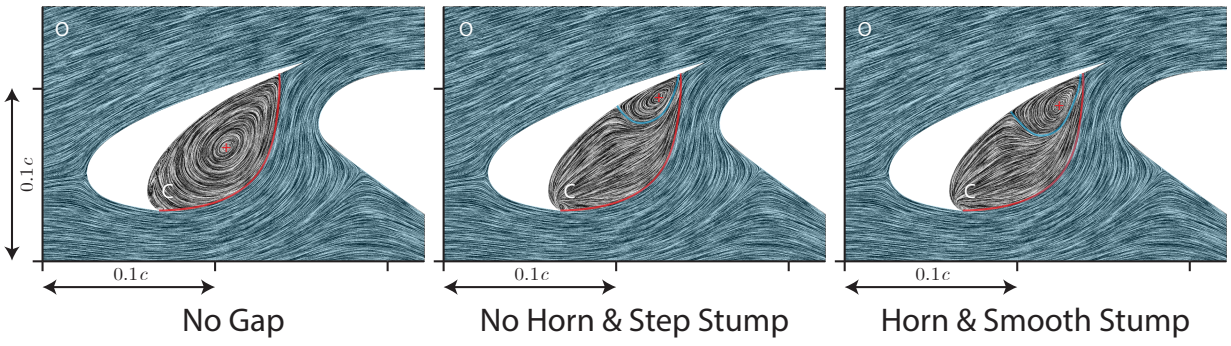

Figure 19: Flow topology through Line Integral Convolution (LIC) at $z = 0.75b$ (figure 18) averaged for 0.33 s. The centre of the recirculation is indicated with '+' symbol. The main shear line is shown in red, and optionally a secondary shear layer is shown in blue.

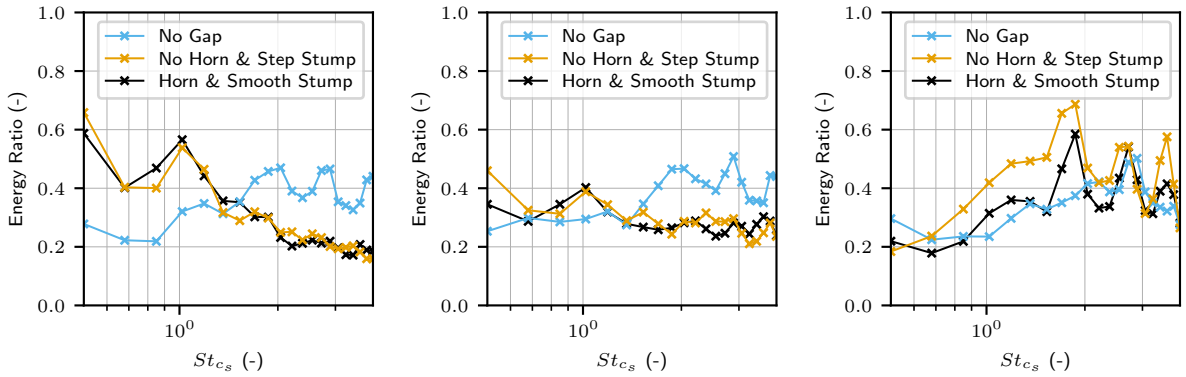

(a) $z = 0.37b$ **(b)** $z = 0.50b$ **(c)** $z = 0.75b$

Figure 20: Energy content of the first SPOD mode compared to the total energy at three planes defined in figure 18.

L_a ($\sim$ straight line between impingement location and the slat cusp), the vortex path length L_v ($\sim$ mean shear line), and the mean vortex convective velocity V. Moreover, the work from Himeno et al. [30] indicates that an additional circulation bubble slows the mean vortex convective velocity, resulting in lower centre frequencies for the narrow-band peaks. Therefore, a retarded vortex convective velocity V is suspected to be the principal reason for the lower frequency of the narrow-band peaks when a sideplate-slat gap is introduced.

$$St_n = \left(n + \frac{1}{4}\right) \frac{c_s}{U_\infty} \frac{V c_{sos}}{c_{sos} L_v + V L_a} \tag{1}$$

The frequency of consistently shedding turbulent structures within the cove can be quantified using a Spectral Proper Orthogonal Decomposition (SPOD) analysis. The flow separation at the slat cusp gives rise to turbulent structures of varying sizes and consequently, different frequencies. Owing to the resonance mechanism between the acoustic radiation at the slat trailing edge, certain turbulent structures with a specific frequency are selected more frequently. In an SPOD analysis, if the first mode in a certain frequency band possesses a high ratio of the energy of the first mode to the total energy, it implies that the turbulent structures are shed very consistently at that frequency band. Figure 20 demonstrates that at the narrow-band peak frequencies, the energy ratio of the first SPOD mode is significant at $z = 0.75b$. Moreover, the shedding frequencies in the No Gap configuration are slightly higher than those in the geometries with a sideplate-slat gap, aligning with the noise response. Hence, a likely slower convective velocity reduces the frequency of the acoustic radiation which selects aerodynamic structures of a lower frequency, closing the resonance loop. Another interesting observation is that the energy ratio of the peaks in the "No Gap" geometry do not reach as high as the two configurations with the gap at $z = 0.75b$. Figure 18 does not imply that the noise intensity at a given spanwise slice is lower when the sideplate-slat gap is closed, nor does the far-field noise response from the microphone probe (figure 11). Therefore, this might merely be a coincidental result of the precise location of the spanwise plane used for the SPOD analysis. At $z = 0.37b$ and $z = 0.50b$ the geometries with a sideplate-slat gap do not show a high energy content in the turbulent structures surrounding the narrow-band peaks, reinforcing the evidence for lack of acoustic-flow resonance at those locations. At $z = 0.37b$ the geometries with a sideplate-slat gap show a large energy peak at lower frequency, which is likely related to the wake structure shown in figure 17.

In conclusion, given the research set-up's loading and flow conditions, the introduction of a sideplate-slat gap reduces the magnitude of the narrow-band peaks, because the slat side-edge wake starts interfering with the flow-acoustic resonance mechanism. Additionally, the gap introduces a second recirculation area which likely retards the convective velocity of the shed turbulent structures, therefore lowers the acoustic radiation frequency and hence the narrow-band peak frequencies.

VIII. Conclusions

This study investigated the relation between fuselage-wing-slat junction designs, and their aeroacoustic footprint. Different junction surface geometries such as the slat side-edge, slat horn, and slat stump show similar far-field noise radiation given a minimally loaded slat. The introduction of a fuselage-slat gap decreased low frequency noise ($St_{c_s} < 4$) compared to a full-span model by c.a. 0.5 dB. This study showed that the spanwise extent of the slat narrow-band peak resonance mechanism can be decreased by preventing impingement of the slat cusp shear on the slat trailing edge. The introduction of a fuselage-slat gap increases the spanwise velocity in the slat cove which partially prevents slat-cusp-to-slat-trailing-edge impingement. This phenomenon is amplified by the inboard slat track which constricts the flow in the slat cove, hence accelerating the cross-flow and decreasing the spanwise resonance extent further.

These findings show that holistic aero-structure and aeroacoustic design can help reduce the junction noise radiation, without impacting the aircraft's loading. The current study has characterised a noise reduction

method for the slat narrow-band peaks by altering large-scale 3D flow structures. Future research could leverage this methodology by re-engineering the junction surfaces, thereby amplifying its capacity for noise reduction.

References

[1] W. Dobrzynski. “Almost 40 Years of Airframe Noise Research: What Did We Achieve?” en. In: *Journal of Aircraft* 47.2 (Mar. 2010), pp. 353–367.

[2] C. A. Hall. “Low noise engine design for the Silent Aircraft Initiative”. en. In: *The Aeronautical Journal* 113.1147 (Sept. 2009), pp. 599–607.

[3] J. Piet, G. Elias, and P. Lebigot. “Localization of acoustic source from a landing aircraft with a microphone array”. en. In: *5th AIAA/CEAS Aeroacoustics Conference and Exhibit*. Bellevue,WA,U.S.A.: American Institute of Aeronautics and Astronautics, May 1999.

[4] P. Sijtsma and R. Stoker. “Determination of Absolute Contributions of Aircraft Noise Components Using Fly-over Array Measurements”. en. In: *10th AIAA/CEAS Aeroacoustics Conference*. Manchester, GREAT BRITAIN: American Institute of Aeronautics and Astronautics, May 2004.

[5] H. Siller, W. Hage, and T. Schumacher. “Source localisation on aircraft in flight - new measurements with the DLR research aircraft Airbus 320 ATRA”. de. In: *7th Berlin Beamforming Conference (BeBeC)*. Berlin, Germany, 2018.

[6] N. Molin, M. Roger, and S. Barre. “Prediction of Aircraft High-Lift Device Noise Using Dedicated Analytical Models”. en. In: *9th AIAA/CEAS Aeroacoustics Conference and Exhibit*. Hilton Head, South Carolina: American Institute of Aeronautics and Astronautics, May 2003.

[7] A. F. Ribeiro et al. “Effect of Slat Tracks and Inboard Slat Tip Geometry on Airframe Noise”. en. In: *28th AIAA/CEAS Aeroacoustics 2022 Conference*. Southampton, UK: American Institute of Aeronautics and Astronautics, June 2022.

[8] B. Bai, Y. Zhang, and X. Li. “Identification of the two-sources at the aircraft slat/fuselage juncture based on phased array”. en. In: *Aerospace Science and Technology* 135 (Apr. 2023), p. 108186.

[9] M. Murayama et al. “Aircraft Noise Reduction Study on Inboard Slat-Tip Region”. en. In: *AIAA AVIATION 2023 Forum*. San Diego, CA and Online: American Institute of Aeronautics and Astronautics, June 2023.

[10] C. Teruna. “Aerodynamic Noise Reduction with Porous Materials: Aeroacoustics Investigations and Applications”. PhD thesis. Delft, The Netherlands: Delft University of Technology, 2022.

[11] D. P. Lockard, M. M. Choudhari, and V. N. Vatsa. “Aeroacoustic Simulations of the High-Lift Common Research Model and Validation with Experiment”. en. In: *28th AIAA/CEAS Aeroacoustics 2022 Conference*. Southampton, UK: American Institute of Aeronautics and Astronautics, June 2022.

[12] H. Chen, S. Chen, and W. H. Matthaeus. “Recovery of the Navier-Stokes equations using a lattice-gas Boltzmann method”. In: *Physical Review A* 45.8 (Apr. 1992). Publisher: American Physical Society, R5339–R5342.

[13] P. L. Bhatnagar, E. P. Gross, and M. Krook. “A Model for Collision Processes in Gases. I. Small Amplitude Processes in Charged and Neutral One-Component Systems”. In: *Physical Review* 94.3 (May 1954). Publisher: American Physical Society, pp. 511–525.

[14] H. Chen et al. “Extended Boltzmann Kinetic Equation for Turbulent Flows”. In: *Science* 301.5633 (Aug. 2003). Publisher: American Association for the Advancement of Science, pp. 633–636.

[15] H. Chen et al. “Expanded analogy between Boltzmann kinetic theory of fluids and turbulence”. en. In: *Journal of Fluid Mechanics* 519 (Nov. 2004), pp. 301–314.

[16] V. Yakhot and S. A. Orszag. “Renormalization group analysis of turbulence. I. Basic theory”. en. In: *Journal of Scientific Computing* 1.1 (Mar. 1986), pp. 3–51.

[17] C. M. Teixeira. “Incorporating Turbulence Models into the Lattice-Boltzmann Method”. In: *International Journal of Modern Physics C* 09.08 (Dec. 1998). Publisher: World Scientific Publishing Co., pp. 1159–1175.

[18] B. E. Launder and D. B. Spalding. “The numerical computation of turbulent flows”. In: *Computer Methods in Applied Mechanics and Engineering* 3.2 (Mar. 1974), pp. 269–289.

[19] H. Chen, C. Teixeira, and K. Molvig. “Realization of Fluid Boundary Conditions via Discrete Boltzmann Dynamics”. In: *International Journal of Modern Physics C* 09.08 (Dec. 1998). Publisher: World Scientific Publishing Co., pp. 1281–1292.

[20] J. E. Ffowcs Williams and D. L. Hawkings. “Sound generation by turbulence and surfaces in arbitrary motion”. en. In: *Philosophical Transactions of the Royal Society of London. Series A, Mathematical and Physical Sciences* 264.1151 (May 1969), pp. 321–342.

[21] F. Farassat and G. P. Succi. “A review of propeller discrete frequency noise prediction technology with emphasis on two current methods for time domain calculations”. In: *Journal of Sound and Vibration* 71.3 (Aug. 1980), pp. 399–419.

[22] J. Gao, X. Li, and D. Lin. “Numerical Simulation of the 30P30N High-Lift Airfoil Noise with Spectral Difference Method”. en. In: *AIAA Journal* 58.6 (June 2020), pp. 2517–2532.

[23] M. Murayama et al. “Experimental Study on Slat Noise from 30P30N Three-Element High-Lift Airfoil at JAXA Hard-Wall Lowspeed Wind Tunnel”. In: *20th AIAA/CEAS Aeroacoustics Conference*. _eprint: https://arc.aiaa.org/-doi/pdf/10.2514/6.2014-2080. American Institute of Aeronautics and Astronautics, June 2014.

[24] R. Merino-Martínez et al. “Aeroacoustic design and characterization of the 3D-printed, open-jet, anechoic wind tunnel of Delft University of Technology”. en. In: *Applied Acoustics* 170 (Dec. 2020), p. 107504.

[25] M. Terracol, E. Manoha, and B. Lemoine. “Investigation of the Unsteady Flow and Noise Generation in a Slat Cove”. en. In: *AIAA Journal* 54.2 (Feb. 2016), pp. 469–489.

[26] S. Melber-Wilkending. “Aerodynamics of the Wing/Fuselage Junction at an Transport Aircraft in High-Lift Configuration”. en. In: *New Results in Numerical and Experimental Fluid Mechanics VII*. Ed. by A. Dillmann et al. Notes on Numerical Fluid Mechanics and Multidisciplinary Design. Berlin, Heidelberg: Springer, 2010, pp. 529–536.

[27] C. Teruna et al. “Numerical investigation of leading edge noise reduction on a rod-airfoil configuration using porous materials and serrations”. en. In: *Journal of Sound and Vibration* 494 (Mar. 2021), p. 115880.

[28] P. R. Spalart and J. H. Watmuff. “Experimental and numerical study of a turbulent boundary layer with pressure gradients”. en. In: *Journal of Fluid Mechanics* 249 (Apr. 1993), pp. 337–371.

[29] P. J. Roache. *Verification and validation in computational science and engineering*. Albuquerque, N.M: Hermosapublishers, 1998.

[30] F. H. T. Himeno et al. “SPOD analysis of noise-generating Rossiter modes in a slat with and without a bulb seal”. en. In: *Journal of Fluid Mechanics* 915 (May 2021). Publisher: Cambridge University Press, A67.

[31] D. Casalino et al. “Flow confinement effects on sUAS rotor noise”. In: *Aerospace Science and Technology* 143 (Dec. 2023), p. 108756.

[32] D. S. Souza et al. “Dynamics of the large-scale structures and associated noise emission in airfoil slats”. en. In: *Journal of Fluid Mechanics* 875 (Sept. 2019). Publisher: Cambridge University Press, pp. 1004–1034.

C

Impact of junction noise reduction on overall noise

This section describes an example calculation for the impact on overall noise by reducing the noise from the fuselage-wing-slat junction. The data is taken from the $60°$ direction of figure 4.1 from Siller et al. [14].

Siller et al. [14] provides the data in third-octave band for the overall integrated beamforming noise, and the integrated 'slathorn', i.e. fuselage-wing-slat junction noise. Calculating the impact of reducing the junction noise by x dB can be done as follows. Let the original two data arrays be S_{junction}, and S_{overall} both in third-octave dB. Then $S_{\text{junction, reduced}}$ is simply given by $S_{\text{junction}} - x$. All data arrays can be converted to pascals using

$$S^{\text{Pa}} = 10^{S^{\text{Pa}}/10}$$

Then the pressure variants $S^{\text{Pa}}_{\text{junction}}$ and $S^{\text{Pa}}_{\text{junction, reduced}}$ can be subtracted to calculate the pressure deficit of the junction per frequency band. The pressure deficit in the junction equals the total reduced pressure, hence the overall reduced pressure $S^{\text{Pa}}_{\text{overall, reduced}}$ can be calculated by subtracting the junction pressure deficit from $S^{\text{Pa}}_{\text{overall}}$. Lastly, the OSPL of $S_{\text{overall, reduced}}$ can be calculated by

$$10\log_{10}\left(\sum S^{\text{Pa}}_{\text{overall, reduced}}\right)$$

Similarly, the OSPL of the original S_{overall} can be calculated and the OSPLs can be compared.

Setting x equal to 3 dB results in a reduction of 0.34 dB overall OSPL. The asymptotical impact of fuselage-wing-slat noise reduction can be calculated by performing the same calculations, but equating $S^{\text{Pa}}_{\text{overall, reduced}}$ to $S^{\text{Pa}}_{\text{overall}} - S^{\text{Pa}}_{\text{junction}}$. This results in a maximum overall noise reduction of 0.71 dB OSPL. The impact on SPL is provided in figure C.1.

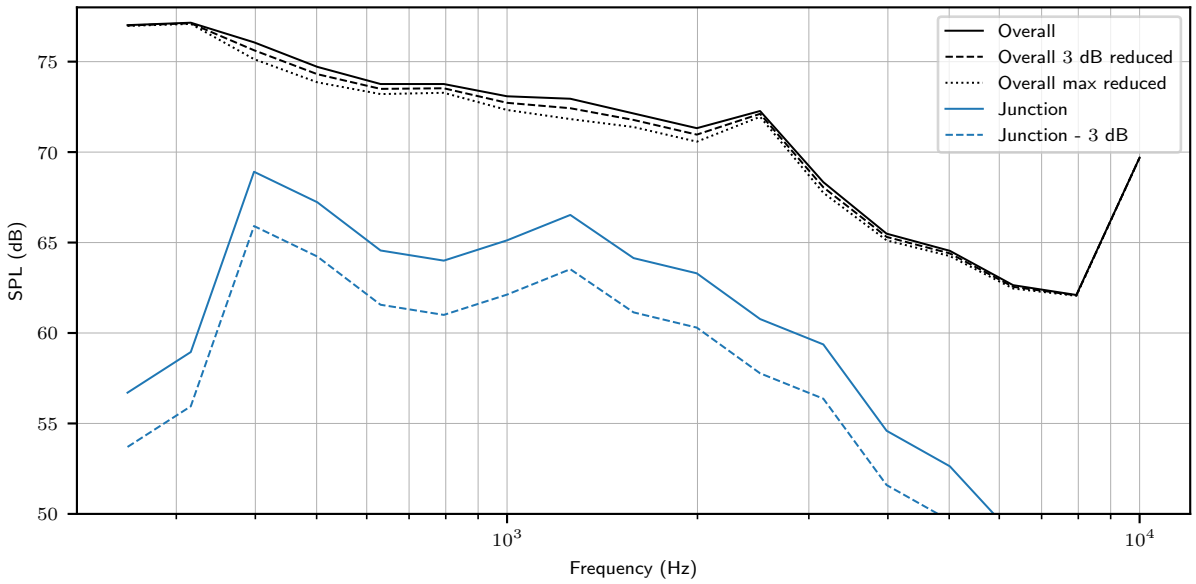

Figure C.1: SPL third-octave band fuselage-wing-slat junction noise reduction example at $60°$, data from Siller et al. [14]

D

Error per section for the open-jet angle of attack correction

The tuned angle of attack was determined based on a minimal value of the sum of Root Mean Square Error (RMSE) of the airfoil suction side, airfoil pressure side, slat suction side and slat pressure side PowerFLOW open-jet simulations compared to the 16° two-element 30P30N RANS simulation. The PowerFLOW simulations were run on a coarse simulation (table 2) with the VR8-zone removed (figure 6.2).

Each section was given the same weight. The slat pressure side was subdivided into three sections, the chord, cove and cusp (figure D.1) which were weighted according to their relative length for the summed RMSE. This subdivision was performed as the RMSE can only be performed on an interpolated grid and for proper interpolation a monotonically increasing (or decreasing) interpolator (x/c-position) was necessary. The absolute pressure coefficient errors per section per relative x/c-position (where in this case c refers to the section chord length, not the wing chord) are given in figure D.2. Increasing the angle of attack always results in a lower error for the main element, throughout the x-position. For the slat, however, the pressure side error increases with the angle of attack whereas the suction side is lowest for 26.2°, below and above which the error increases. Based on the patterns in the streamwise error it is likely that an increased angle of attack will reduce the main element error at all streamwise positions. The slat error, however, will only increase for lower and higher angles of attack than 26.2°.

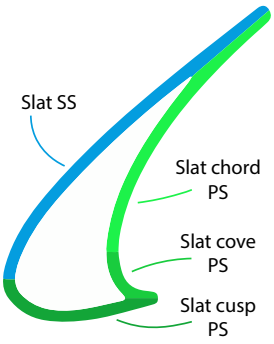

Figure D.1: Definition of slat subdivision used for the RMSE comparison

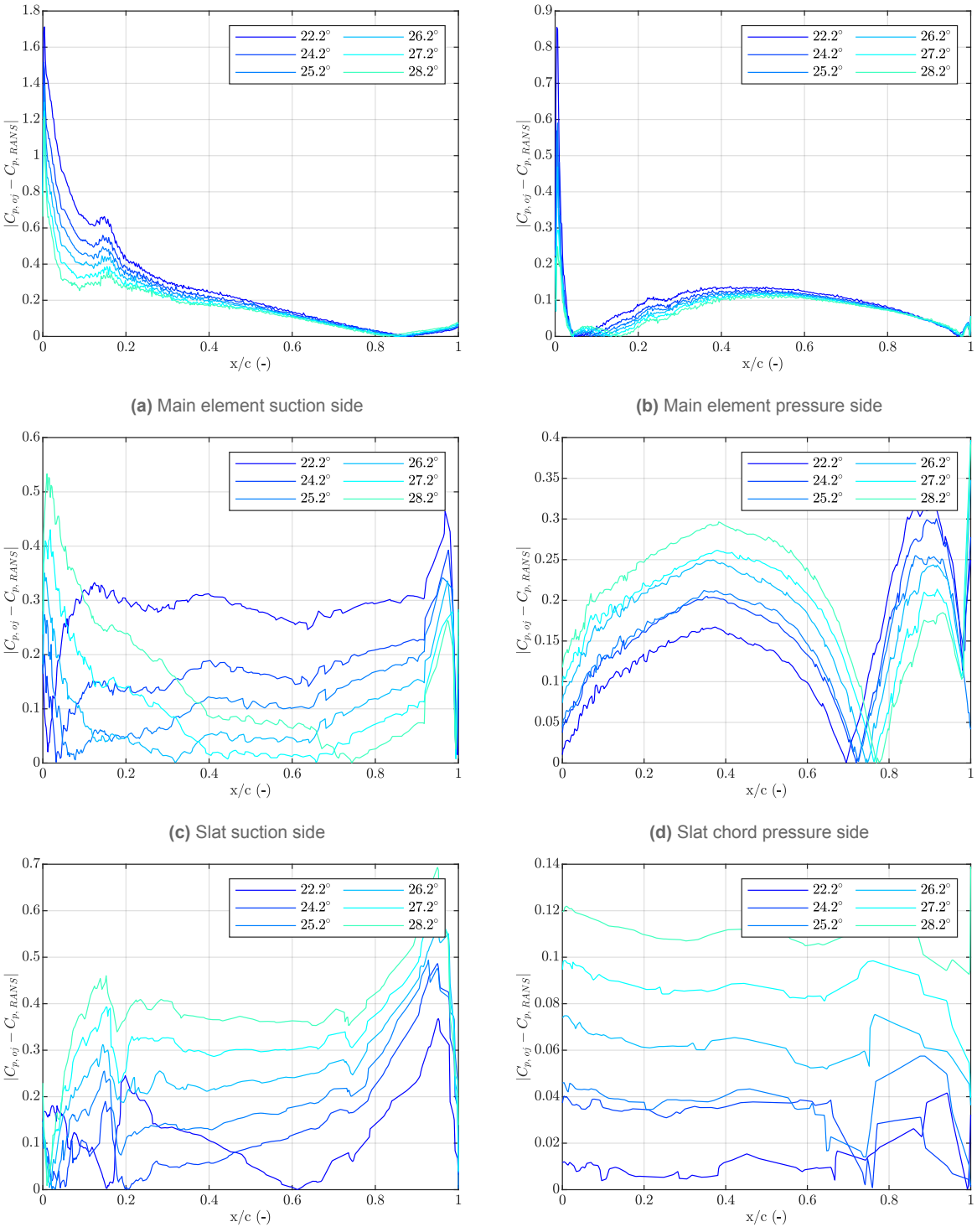

(a) Main element suction side

(b) Main element pressure side

(c) Slat suction side

(d) Slat chord pressure side

(e) Slat cusp pressure side

(f) Slat cove pressure side

Figure D.2: Absolute error $|C_{p,\,oj} - C_{p,\,RANS}|$ of the pressure coefficient compared to RANS per section

E

Utilising a PowerCASE acoustic sponge zone

Numerical studies aim to represent phenomena accurately with minimal computational cost. This involves careful consideration of the simulation domain size, mesh, boundary conditions, and initial conditions. In aeroacoustic numerical studies, the requirements for aerodynamic simulation and acoustic analysis can sometimes conflict.

Acoustic analyses usually need a large domain size to reduce the effect of unavoidable reflections (refer to Giancoli [92, p. 409] and figure E.1). However, large domains are computationally expensive and low-frequency noise, which has large wavelengths, takes a long time to dampen.

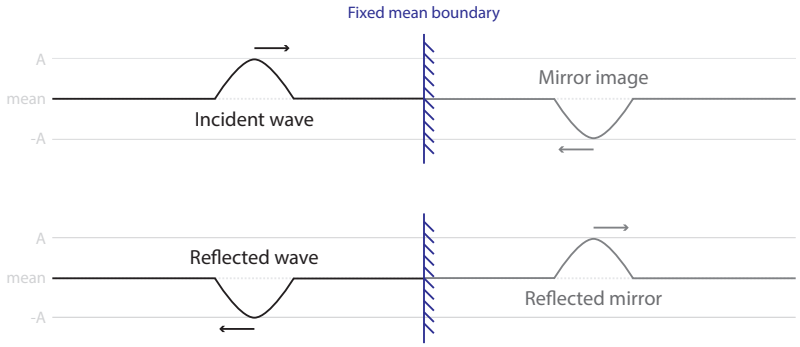

Figure E.1: Wave reflections at a fixed boundary. A wavefront approaches a boundary which imposes a fixed value on the medium. An equal but opposite wave must be exerted on the boundary to enforce the fixed value (the mirror image of the wave). This in turn causes a reflected wave to be radiated back into the domain.

Numerical pressure wave reflections can interfere with proper acoustic analysis. A common solution is to introduce a numerical acoustic sponge zone. In this zone, outside the domain of interest, the fluid medium's viscosity to temperature ratio (ν/T) gradually increases, enhancing the resistance to fluctuations. This change in resistance causes part of the wavefront to reflect and part to transmit and dampen. Therefore, it's crucial to ensure a smooth transition from the original resistance to a high-resistance outer zone.

PowerFLOW provides the capability to numerically adjust the ν/T ratio of a fluid. To access this feature, PowerCASE must be launched with additional options, specifically the *-expose_nu_over_t* option.

To do this, navigate to the 'PowerCASE.exe' application directory (not the shortcut directory) and create a new .bat file. In Windows, you can create a .bat file by opening Notepad as an administrator (right-click on Notepad > Run as administrator). Insert the following line of text and save the file as "all files" with a .bat extension (e.g., runPowerCASE.bat).

```
"Path\To\PowerCASE\Directory\PowerCASE.exe" -expose_nu_over_t "%~1"
```

Next, go to the PowerCASE shortcut directory > right-click > properties. Change the application path from PowerCASE.exe to runPowerCASE.bat (or the name given to the .bat file).

```
"Path\To\PowerCASE\Directory\runPowerCASE.bat"  // changed to .bat file
```

Finally, after creating the first .case file using PowerCASE, you can set .case files to always open with the *-expose_nu_over_t* option. Right-click on a .case file > open with > runPowerCASE.bat. This ensures that PowerCASE always opens with the *-expose_nu_over_t* option enabled.

Whenever PowerCASE is opened, fluids (located under Parameters > Fluid/Solid) will display with an extra column ‘Nu/T’ (figure E.2). Editing the fluid allows the ‘Nu/T’ field to be specified to a constant, or any variable defined in either the ‘Case Variables’ or ‘Calculations’ page in PowerCASE (figure E.3).

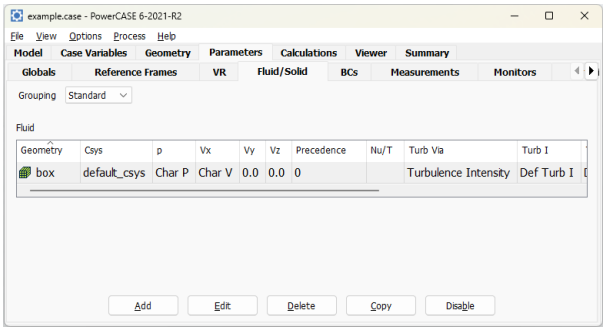

Figure E.2: Fluid/Solid page overview

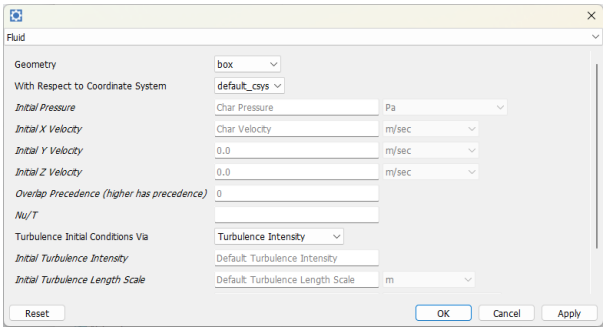

Figure E.3: Fluid edit window

The ‘Nu/T’ field on the fluid page requires no unit, as it expects a value or variable given in non-dimensionalised ‘lattice units’. Additionally, setting a value in the ‘Nu/T’ is additive to the original, i.e. a numerical addition to the ratio.

$$\left(\frac{\nu}{T}\right)_{\text{fluid, new}} = \left(\frac{\nu}{T}\right)_{\text{fluid, original}} + \left(\frac{\nu}{T}\right)_{\text{numerical}}$$

Having noted how PowerCASE handles the ‘Nu/T’ option, a correct initialisation of the fluids in the domain can be set up. The fluid in the region of interest (surrounding the element from which the noise radiation must be determined) should not have its ν/T ratio altered as it will alter the actual Reynolds number experienced by the test section. Hence, at least two fluid regions must be defined. An inner region of the sponge zone, which has the ‘Nu/T’ option disabled (no value assigned to it) and an outer region of the fluid from which the ν/T steadily rises towards higher values that damp the pressure fluctuations without causing reflections.

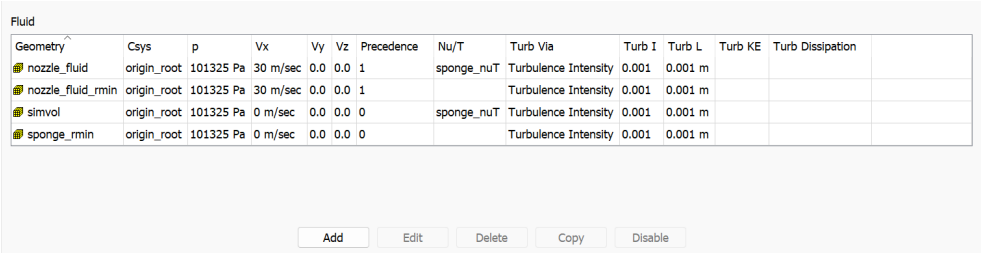

Figure E.4: example of multiple fluids with ‘Nu/T’ options

The example in figure E.4 has four fluids defined. The ‘simvol’ fluid covers the entire domain and has the ‘Nu/T’ option enabled for the variable ‘sponge_nuT’. The ‘sponge_rmin’ fluid is a sphere surrounding the test object which has the original, unaltered ν/T values. Since the ‘sponge_rmin’ object is fully enclosed by the ‘simvol’ object, it gets automatic precedence. This example also has two additional fluids defined, the ‘nozzle_fluid’ and the ‘nozzle_fluid_rmin’. These fluid objects are present to initialise the X-velocity within the nozzle to 30 m/s, whereas the rest of the domain is initialised to 0 m/s. The ‘nozzle_fluid_rmin’ is fully enclosed by the ‘nozzle_fluid’, hence it takes automatic precedence. The ‘sponge_rmin’, ‘nozzle_fluid_rmin’, and ‘nozzle_fluid’ fluids however, partly overlap. Hence, the nozzle fluids are set to precedence ‘1’ to ensure that the velocity in every part of the nozzle is indeed set to 30 m/s.

To minimise reflections, the ν/T ratio should gradually change, without sudden jumps anywhere in the domain. Additionally, the derivatives of ν/T should be smooth as well, to ensure minimal reflections. An S-shaped function prescribed to a ‘sponge_nuT’ variable is a likely candidate. Designing a variable in PowerCASE that varies the ν/T ratio based on its location, without causing any sudden jumps anywhere in the domain, is not as flexible as with actual programming languages. Hence, the most straightforward

method is to use a single spatial variable, a radial distance to a point, to calculate a ν/T variable. In that case, an option for an S-shaped logical function starting from $(\nu/T)_{\text{min}}$ to $(\nu/T)_{\text{max}}$ would be

$$\frac{\nu}{T}(r) = (\nu/T)_{\text{min}} + \frac{(\nu/T)_{\text{max}} - (\nu/T)_{\text{min}}}{1 + \exp(-s(r - r_{\text{inflexion}}))}$$

where r is the radial distance, $r_{\text{inflexion}}$ the location of the inflexion point of the S-shaped function and s the steepness of the curve. The downside of a logical function is that you cannot determine the location at which the variable reaches either $(\nu/T)_{\text{min}}$ or $(\nu/T)_{\text{max}}$, which are situated at $-\infty$ and $+\infty$ respectively. However, with a proper combination of the steepness parameter and the location of the inflexion point, the ν/T-ratio will almost be equal to $(\nu/T)_{\text{min}}$ at the beginning of the sponge. A very small jump will remain at the boundaries between the different fluids.

Yet, an improved infinitely smooth interpolant can be designed as well. A 'bump function' is a function that is both smooth (infinitely differentiable), and compactly supported, i.e. only non-zero in a range of values. A subset of bump functions, 'smooth transition functions', are only non-constant in a range of values. A smooth transition function, which is mathematically designed to transition from $y = 0$ to $y = 1$ between $0 < x < 1$, can be modified to transition from any starting value to any end value, between any specific range. The following set of equations serves this purpose for the $\nu/T(r)$ transition of an anechoic sponge zone.

$$\psi(r) = \begin{cases} e^{-\frac{r_{\text{max}} - r_{\text{min}}}{r}}, & r > 0 \\ 0, & r = 0 \end{cases}$$

$$\phi(r) = \begin{cases} 0, & r \leq r_{\text{min}} \\ \frac{\psi(r - r_{\text{min}})}{\psi(r - r_{\text{min}}) + \psi(r_{\text{max}} - r)}, & r_{\text{min}} < r < r_{\text{max}} \\ 1, & r \geq r_{\text{max}} \end{cases}$$

$$\frac{\nu}{T}(r) = (\nu/T)_{\text{min}} + \left((\nu/T)_{\text{max}} - (\nu/T)_{\text{min}}\right) \cdot \phi(r)$$

The code below shows an example implementation of the S-shaped interpolant in the Calculations page in PowerCASE. The 'SPONGE_RMAX' and 'SPONGE_RMIN' are scalars to be set on a case-by-case basis. Often they are the radius of a sphere added to the PowerCASE with radii defined between the halfway points of VR0-VR1 and VR1-VR2, and the origin at the same origin point as the 'CS' variable. The 'CS' variable must be added to PowerCASE as a coordinate system. PowerFLOW will then calculate the ν/T-ratio based on the location in the domain, including which fluid is defined at that location (with the variable ν/T either used or not) and the 'sponge_nuT' variable if the fluid has the variable enabled.

```
//============================================
// sponge_determination

//============================================

sponge_nuT_min    = 0;
sponge_nuT_max    = 0.5;

sponge_rmin   = SPONGE_RMIN <<m>>;
sponge_rmax   = SPONGE_RMAX <<m>>;
sponge_r    = sqrt(CS.x^2+CS.y^2+CS.z^2);

// Use the s curve function to create a smooth transition of nuT values

sponge_steepness  = 12/(sponge_rmax-sponge_rmin);
sponge_horizontal_shift = (sponge_rmin + sponge_rmax) / 2;

sponge_nuT    = (1 / (1 + exp(-sponge_steepness * (sponge_r - sponge_horizontal_shift)))) * (
    sponge_nuT_max - sponge_nuT_min) + sponge_nuT_min;
```

Checking whether the sponge zone and the ν/T-variable are defined properly is unfortunately impossible in PowerCASE. PowerVIZ can visualise the variable 'sponge_nuT' after a full simulation, but also after discretisation. After discretisation, a .lgi file is created in the folder where the PowerCASE .cdi file has run on the server. In the Linux terminal which is connected to the server (e.g. the HPC12) navigate to the correct folder which contains the .cdi and .lgi file after discretisation and perform the following command.

```
lgi_to_fnc CDI_FILE.cdi LGI_FILE.lgi
```

This will create a .fnc file that can be read into PowerVIZ in conjunction with the .cdi file. Inside PowerVIZ go to Project > Equations > New > Open Editor > paste the ”Sponge_determination” code that has been defined in PowerCASE in the editor > Check > Calculate. Then, use Fluid > Axis aligned slice > Scalar Property Set > sponge_nuTand make sure to check the Slice Image checkbox under Image / Grid > Slice Image. Additionally, it is good practice to simply plot the logic curve and the sponge_rmin and sponge_rmax points to check its behaviour before discretising. A Python script corresponding to the PowerCASE sponge_determination above is defined below. Comment out line 6 if Latex is not installed on your machine. This particular example yields the curve shown in figure E.5.

```
1  import numpy as np
2  import matplotlib.pyplot as plt
3
4  # Use latex formatting (need a local latex interpreter for this to work)
5  plt.rcParams['text.usetex'] = True
6  plt.rcParams['font.size'] = 7
7
8  # Define figure parameters adjusted to a latex report
9  textwidth = 0.77 * 210 / 25.4  # in inches
10 lw = 0.75
11 ms = 18
12
13 # Given values
14 V0_r = 5
15 V1_r = 4
16 V2_r = 3
17
18 sponge_nuT_min = 0.
19 sponge_nuT_max = 0.5
20
21 sponge_rmin = V2_r + 1. / 2. * (V1_r - V2_r)
22 sponge_rmax = V1_r + 1. / 2. * (V0_r - V1_r)
23
24 # Generate sponge_r values from 0 to 5
25 sponge_r = np.linspace(sponge_rmin - 0.5 * sponge_rmin, sponge_rmax + 0.5 * sponge_rmin, 1000)
26
27 # Use the s curve function to create a smooth transition of nuT values
28 sponge_steepness = 12 / (sponge_rmax - sponge_rmin)
29 sponge_horizontal_shift = (sponge_rmin + sponge_rmax) / 2
30
31 sponge_nuT = (1 / (1 + np.exp(-sponge_steepness * (sponge_r - sponge_horizontal_shift)))) * (
32             sponge_nuT_max - sponge_nuT_min) + sponge_nuT_min
33
34 # Plotting
35 fig, ax = plt.subplots(figsize=(0.5*textwidth, 0.4*textwidth))
36
37 ax.plot(sponge_r, sponge_nuT,  color='black', linewidth=lw)
38 ax.scatter(sponge_rmin, sponge_nuT_min, color='black', marker="x", linewidth=lw, s=ms)
39 ax.scatter(sponge_rmax, sponge_nuT_max, color='black', marker="x", linewidth=lw, s=ms)
40 ax.set_xlabel(r'Distance to domain centre (m)')
41 ax.set_ylabel(r'Additional $\nu/T$ (-)')
42 ax.grid(which='both', linewidth=0.5*lw)
43
44 fig.tight_layout()
45
46 fig.savefig('sponge_curve_old.pdf', bbox_inches='tight')
47
48 plt.show()
```

A Python implementation for the ‘smooth transition function’ is provided below. Comment out line 42 if Latex is not installed on your machine. This particular example yields the curve shown in figure E.6.

```
1  """
2  Continuously smooth step function between two straight lines
3  based on https://www.youtube.com/watch?v=vD5g8aVscUI&list=WL&index=29
4
5  author: H.I.G. Piera
6  date: 2024
```

```
"""

import numpy as np
import matplotlib.pyplot as plt


# Define the functions
def psi(x, dx):
    """
    psi(x) = exp(-dx/x) is a continuously smooth function from 0 to 1
    :param x: x location
    :param dx: xmax - xmin
    :return: psi(x)
    """
    return np.exp(-dx/x) if x > 0 else 0


def phi(x, x_min=0., x_max=1.):
    """
    phi(x) = psi(x-x_min) / (psi(x-x_min) + psi(x_max - x)) is smooth step from 0 to 1 between
    x_min and x_max
    :param x: x location
    :param x_min: start of interpolation
    :param x_max: end of interpolation
    :return: phi(x)
    """
    dx = x_max - x_min
    if x <= x_min:
        return 0
    elif x_min < x < x_max:
        return psi(x-x_min, dx)/(psi(x-x_min, dx) + psi(x_max-x, dx))
    else:
        return 1


# plot parameters
plt.rcParams['text.usetex'] = True
plt.rcParams['font.size'] = 7

textwidth = 0.77 * 210 / 25.4  # in inches
lw = 0.75
ms = 18

# Given values
V0_r = 5
V1_r = 4
V2_r = 3

sponge_nuT_min = 0.
sponge_nuT_max = 0.5

sponge_rmin = V2_r + 1. / 2. * (V1_r - V2_r)
sponge_rmax = V1_r + 1. / 2. * (V0_r - V1_r)

# Generate x values
sponge_r = np.linspace(sponge_rmin - 0.5 * sponge_rmin, sponge_rmax + 0.5 * sponge_rmin, 1000)

# Generate y values for each function
y_phi = [sponge_nuT_min + (sponge_nuT_max-sponge_nuT_min)*phi(i, sponge_rmin, sponge_rmax) for
    i in sponge_r]  # rescale the phi function based on y_min, y_max

# Create the plot
fig, ax = plt.subplots(figsize=(0.5*textwidth, 0.4*textwidth))

ax.plot(sponge_r, y_phi, linewidth=lw, color="black")
ax.scatter(sponge_rmin, sponge_nuT_min, color='black', marker="x", linewidth=lw, s=ms)
ax.scatter(sponge_rmax, sponge_nuT_max, color='black', marker="x", linewidth=lw, s=ms)
ax.set_xlabel(r'Distance to domain centre (m)')
ax.set_ylabel(r'Additional $\nu/T$ (-)')
ax.grid(which='both', linewidth=0.5*lw)

```

```
fig.tight_layout()

fig.savefig('sponge_curve_new.pdf', bbox_inches='tight')

plt.show()
```

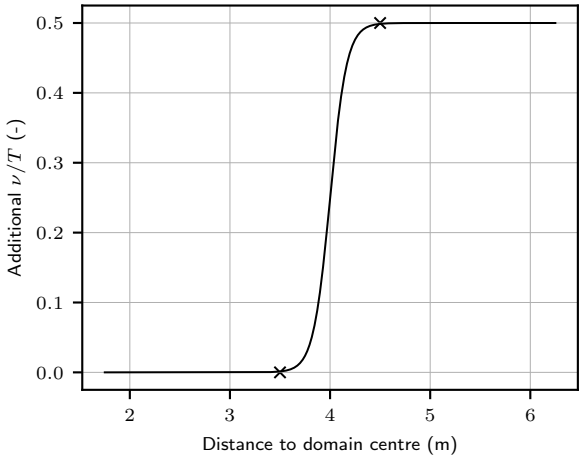

Figure E.5: Defined numerical alteration of ν/T for an S-shaped function

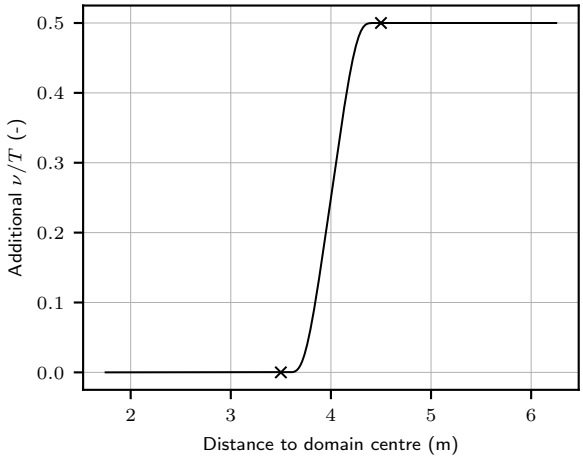

Figure E.6: Defined numerical alteration of ν/T for a 'smooth transition function'

F

Description of measurements

Setting up a numerical simulation requires a thorough understanding of the expected flow field, as well as a good understanding of all goals of the study and their related necessary measurement. The measurements for this study can be split into five categories: verifying the **simulation** itself, verifying the **design** requirements of the research set-up, answering the research **questions**, comparing the novel research set-up to **literature**, and performing a grid **convergence** study between different mesh refinements. Table F.1 provides an overview of the performed measurements, their related goal and category, and the specifications with which the measurements were performed.

Table F.1: Description of measurements

Measurement & location	Goal	Category	Res.	Time (s)	t_{avg} (s)	f_{avg} (Hz)
Flow around the full research set-up	• Flow behaviour check • Acoustic wave behaviour check	simulation	VR5	3.33E-02	8.33E-04	1200
Flow around the full research set-up (instantaneous)	Flow behaviour check	simulation	VR5	3.33E-02	dt_vr8	
Flow at nine evenly spaced single voxel depth spanwise sections	• Detailed flow behaviour check • Detailed acoustic wave behaviour check	simulation	VR8	3.33E-02	8.33E-04	1200
Flow at nine evenly spaced single voxel depth spanwise sections (instantaneous)	Detailed flow behaviour check	simulation	VR8	3.33E-02	dt_vr8	
Flow around the sideplate-slat junction	Junction vortex visualisations	questions, literature	VR8	6.60E-03	1.67E-04	6000
Flow around the sideplate-slat junction (instantaneous)	Junction turbulent flow structures visualisations	questions, literature	VR8	6.60E-03	dt_vr8	
Flow around the sideplate-slat junction (steady)	• Junction wake visualisations • Sideplate boundary layer thickness determination	questions, design, convergence	VR8	3.33E-01	3.33E-01	3
Flow inside the slat cove	Slat cove vortex visualisations	questions, literature	VR8	6.60E-03	1.67E-04	6000
Flow inside the slat cove (instantaneous)	Slat cove turbulent flow structures visualisations	questions, literature	VR8	6.60E-03	dt_vr8	
Flow inside the slat cove (steady)	• Slat cove wake visualisations • Slat cove streamlines	questions, literature	VR8	3.33E-01	3.33E-01	3
Flow inside the entire simulation domain	Flow behaviour check	simulation	VR3	3.33E-01	3.33E-02	30
Flow on a plane parallel to the span inside the nozzles and sideplates of a single voxel depth	Flow behaviour check	simulation	VR8	3.33E-02	8.33E-04	1200
Flow at a plane parallel to the span inside the nozzles and sideplates of a single voxel depth (instantaneous)	Flow behaviour check	simulation	VR8	3.33E-02	dt_vr8	
Flow at seven LE planes orthogonal to the sweep from the slat horn towards the midsection (low frequency)	• SPOD • Slat cove streamlines	questions, design	VR8	3.33E-01	1.67E-04	6000
Flow at seven LE planes orthogonal to the sweep from the slat horn towards the midsection (high frequency)	• SPOD • Turbulent flow structures visualisation	questions, design	VR8	1.99E-02	8.33E-06	120000
Flow at two planes parallel to the flow stream in the sideplate-slat junction (low frequency)	SPOD	questions	VR8	3.33E-01	1.67E-04	6000
Flow at two planes parallel to the flow stream in the sideplate-slat junction (high frequency)	• SPOD • Turbulent flow structures visualisation	questions	VR8	1.99E-02	8.33E-06	120000
Surface measurement of the full research set-up including sideplates (low frequency)	• Pressure fluctuation spectra (wall + far field with FWH) • Noise source visualisation (beamforming + FWH based) • Noise directivity	questions, literature, convergence	0.0028 m	3.33E-01	1.67E-04	6000
Surface measurement of the full research set-up including sideplates (high frequency)	• Pressure fluctuation spectra (wall + far field with FWH) • Noise source visualisation (beamforming + FWH based) • Noise directivity	questions, literature, convergence	0.0028 m	1.99E-02	8.33E-06	120000
Surface measurement of the full research set-up including sideplates (steady)	• y^+ specification • Static pressure (loading) • Pressure fluctuation intensity • Streamlines	questions, literature, design, simulation, convergence	VR8	3.33E-01	3.33E-01	3
Flow microphone probes at numerous positions outside of the nozzle jet in the far-field	Pressure fluctuation spectra	questions, literature, convergence	VR4	3.33E-01	dt_vr4	
Flow microphone probes at the nozzle exit	Nozzle velocity check	simulation	VR4	4.00E-01	dt_vr4	
Flow microphone probes along numerous presumed slat mean shear lines	Aerodynamic fluctuation spectra	questions	VR7	3.33E-01	dt_vr5	
Integral force measurument of the research set-up	Lift and drag development over time	simulation, convergence	N/A	4.00E-01	1.67E-04	6000